FH ▶▶

Wiener Neustadt

Tulln an der Donau

ANALYSIS OF FIBER ATTRITION AND FIBER-MATRIX SEPARATION DURING INJECTION MOLDING OF LONG FIBER-REINFORCED THERMOPLASTIC PARTS

Sara Andrea Simon, B.Sc.

Austrian Biotech University of Applied Sciences

Campus Tulln

Master Thesis

Master Degree Program Biotechnical Processes

Tulln, November, 2016

Assessor: **Dipl.- Ing. Birgit Herbinger**

Completed at: **University of Wisconsin-Madison, Polymer Engineering Center**

Supervisor: **Prof. Dr. Tim A. Osswald**
Sebastian Goris, M.Sc. and Ph.D. candidate

ACKNOWLEDGEMENTS

Kurzzusammenfassung

Die Erhaltung der ursprünglichen Faserlänge bei der Verarbeitung von glasfaserverstärkten Thermoplasten ist von großem Interesse, da die Endfaserlänge die mechanischen Eigenschaften des Fertigteils bestimmt. Faserbruch im Zuge der Verarbeitung ist unvermeidlich und eine große Herausforderung, da er schwierig zu kontrollieren ist und die zugrunde liegende Physik nach wie vor noch nicht vollständig erforscht ist und verstanden wird. Um ein besseres Verständnis zu bekommen wurde die Faserschädigung von langglasfaserverstärktem Polypropylen in einer Couette Strömung untersucht. Die Ergebnisse zeigen, dass das verwendete Couette Rheometer ein geeignetes Gerät ist um die Auswirkungen von unterschiedlichen Prozessbedingungen auf den Faserbruch zu eruieren, zu isolieren und diese des Weiteren auch zu quantifizieren. Es konnte nachgewiesen werden, dass sowohl die Temperatur, als auch die Faserkonzentration, die Schergeschwindigkeit und die Verweilzeit einen großen Einfluss auf die Faserschädigung haben, die sich in einem Faserbruch von bis zu 90 % widerspiegelt.

Die Faserbruchstudie wurde erweitert indem die Faserlängenverteilung entlang der Strömungsrichtung von Spritzgussteilen analysiert wurde. Ein weiterer Teil dieser Arbeit beschäftigte sich mit der Untersuchung der Faser-Polymer-Trennung in Spritzgussteilen, da auch dieses Phänomen beträchtlich zu einem heterogenen Eigenschaftsprofil in den Fertigteilen beiträgt. Zur Evaluierung dieser Faser-Matrix Separation wurden Computertomographie Scans angefertigt, die in Folge mit digitale Bildverarbeitung ausgewertet wurden. Die erhaltenen Ergebnisse zeigen eine deutliche Faser Agglomeration in der Kernschicht des Formteils, in welcher eine Erhöhung der Faserkonzentration von bis zu 40 % festgestellt werden konnte. Die experimentellen Daten aus den Couette Rheometer Experimenten wurden in weiterer Folge zur Validierung und Bewertung von verfügbaren Tools zur Vorhersage der Faserschädigung (Faserbruch Simulation) verwendet. Ein spezielles Augenmerk wurde auf das Phelps Kontinuum Modell gelegt, welches implementiert und in weiterer Folge für die Couette Rheometer Versuche angewandt wurde. Des Weiteren wurden die empirischen Modellparameter aus dem Phelps Modell als Eingangsvariablen für eine Moldex3D Simulation verwendet, um den Faserbruch in einem spritzgegossenem Fertigteil zu bestimmen. Das Phelps Modell wurde erfolgreich umgesetzt, jedoch war es mit den erhaltenen Ergebnissen nicht möglich die Materialabhängigkeit der empirischen Modellparameter zu bestätigen. Die Ergebnisse aus den Modex3D Simulationen zeigen, dass die Phelps Modell Parameter nicht verwendet werden können um den Faserbruch in Spritzgusssimulationen vorherzusagen, da die Parameter nicht übertragbar sind - auch nicht zwischen dem gleichen Material. Da Single Particle Modelle in Prozesssimulationen an Beliebtheit gewinnen, wurde ein kürzlich veröffentlichtes Single Particle Modell auf seine Vorhersagekraft für Faserbruch getestet. Es war möglich, das Modell in einem ersten Schritt qualitativ zu validieren. Jedoch sind zusätzliche Simulationen notwendig, um die Gültigkeit des Modells für ein breiteres Spektrum von Daten zu bestätigen.

Schlagworte

Glas Faser, Polypropylen, Mikrostrukturanalyse, Prozess Simulation, Couette Strömung, Spritzgießen, Faserbruch

Abstract

Preserving the initial fiber length of glass fiber-reinforced thermoplastics during processing is from major interest since the residual fiber length determines the mechanical properties of the finished part. Fiber length attrition during processing is still an inevitable and substantial challenge, because it is difficult to control and the underlying physics are not completely understood. In order to gain a better understanding in the phenomena of fiber breakage, the fiber degradation of long glass fiber-reinforced polypropylene in a Couette flow was studied. The results of this work show that the Couette rheometer is an important device to isolate and quantify the impact of processing conditions on the fiber breakage for long glass fiber-reinforced thermoplastics. Temperature, residence time, fiber concentration and processing speed all have a major impact on fiber attrition with breakage rates of up to 90 %.

The study was expanded to injection molded parts and the fiber length distribution along the flow path was analyzed. An additional study of injection molded parts focused on the phenomena of fiber-matrix separation since it also causes highly heterogeneous properties within the finished part. This analysis was conducted using micro computed-tomography scans and digital image processing. The results clearly show a substantial fiber agglomeration in the core layer of the molded part of up to 40 % increase from the nominal value.

Lastly, the experimental data obtained in this work was used to evaluate available predictive tools for fiber breakage simulation. A comprehensive study focused on the Phelps continuum model, which was implemented and applied for the Couette rheometer experiments. Additionally, the empirical model parameters from the Phelps model were used as an input for a Moldex3D simulation to determine the fiber breakage in an injection molded plaque. The Phelps model was successfully implemented. However, the results were not able to prove the material dependency of the empirical model parameters. The results from the Moldex3D simulations display that the Phelps model parameter cannot be used to accurately predict the fiber breakage in injection molding simulations since the model parameters seem to be not transferable even for the same material. As single particle models become more popular in process simulation, a recently published single particle model was tested for its ability to predict fiber breakage. It was possible to validate the single particle model in a first step, but to confirm the model´s validity for a broader set of data additional simulations are necessary.

Keywords

List of Abbreviations

A	Cross sectional area
B	Radius of curvature
BC	Boundary condition
B_i	Dimensionless variable for buckling (Phelps model)
CAE	Computer aided engineering
C_B	Breakage parameter (Phelps- and Baird model)
$C_B^{IM}*$	C_B parameter reported in terms of a dimensionless time for IM
d	Diameter
E_f	Elastic modulus
F	Force
FC	Fiber concentration
FD	Fiber density
FL	Fiber length
FLD	Fiber length distribution
FO	Fiber orientation
FRT	Fiber-reinforced thermoplastics
H	Gate thickness
IM	Injection molding
l	Length
l_{crit}	Critical fiber length
LFT	Long fiber-reinforced thermoplastics
L_N	Number average fiber length
L_W	Weight average fiber length
m	Shape parameter (Durin model)
n	Power law index
N_{PDF}	Normal probability density distribution (Phelps model)
PA	Polyamide
PEC	Polymer Engineering Center
P_iN_i	Breakage probability of parent fibers (Phelps model)
PP	Polypropylene
PPGFX	X% glass fiber-reinforced Polypropylene
PS	Polystyrol

Q	Volumetric flow rate
r	Radius
R_{BREAK}	Critical radius for breaking (Baird model)
$R_{ik}N_k$	Children fiber generation (Phelps model)
RPM	Revolutions per minute
RTD	Residence time distribution
S	Shape parameter (Phelps model)
SABIC	Saudi Arabia Basic Industries Corporation
SD	Standard deviation
T	Temperature
t*	Dimensionless time
u	Velocity flow field
W	Gate width
W(Li)	Cumulative fiber length distribution
µCT	Micro Computed Tomography
β_e	Average aspect ratio for cylindrical objects (Durin model)
∂	Partial derivative
т	Torque
Ω	Rotational speed
η	Viscosity
η_0	Zero shear rate viscosity
τ	Shear stress
$\tau*$	Critical shear stress
$\dot{\gamma}$	Shear rate
ζ	Hydrodynamic drag coefficient (Phelps model)
ω	Angular velocity
σ	Tensile stress

Table of Contents

1 Introduction

1.1 Description and Objective of the Task

Over the last decade, a continuously rising demand has been noted for fiber-reinforced thermoplastics (Malnati, 2007, Thomason, 2005, Goris and Osswald, 2016). A market study forecasts that the US demand for fiber-reinforced plastic composites will increase by 4.7 % in 2017 (Freedonia, 2013). Since motor vehicles represent the leading outlet of fiber-reinforced composites and is anticipated to be the main driver for the industry´s growth through 2017 an increased vehicle output is predicted (Freedonia, 2013). Especially long fiber-reinforced thermoplastics (LFT) have gained importance in the automotive industry due to their high performance in terms of mechanical properties (favorable specific stiffness and impact strength), low cost, processing advantages and low density (Nguyen, 2010, Zhang and Thompson, 2005, Thomason, 2005, Wang et al., 2011). LFTs are used for manufacturing bumper beams, front end modules, instrument panel carrier, door modules and under body shields of automobiles (Shi et al., 2013). LFTs have an edge over traditional materials such as steel and aluminum due to their high specific strength, good damping capacity, impact resistance and, corrosion resistance. But most important is their exceptional lightweight, which enables car manufacturer to decrease the overall weight of vehicles and therefore reduce fuel consumption (Nguyen, 2010, Nguyen et al., 2008a, Thomason, 2002). Additionally, LFTs show improved recyclability compared to conventional materials (Inoue et al., 2015, Zhang and Thompson, 2005, Stewart, 2003, Jeyanthi and Rani, 2012).

Although LFTs are an ideal material class for low cost lightweight applications, there is still uncertainty and a lack of control of the final properties of LFT parts. The final state of the fibers determines the local and global properties of the finished part. Over all stages of processing LFT (e.g. injection molding), the configuration of the fibers changes significantly, reflected in form of fiber attrition, excessive fiber orientation (FO), fiber jamming and fiber-matrix separation that ultimately results to highly heterogeneous properties within the finished part (Goris et al., 2016).

In order to accurately address this process-induced fiber microstructure, a fundamental understanding of the physics behind fiber motion is required, which also includes the interrelationship between FO, fiber-matrix separation and fiber breakage (Goris et al., 2016) (Figure 1).

Furthermore, it is essential to be able to accurately predict the mechanical performance from the process-induced microstructure (Figure 1). This is due to the fact that current approaches in LFT material modeling and structural analyses assume that fiber length (FL) and fiber density (FD) are uniform throughout the part. However, measurements demonstrate that the local FL and FD vary substantially in the finished part (Lafranche et al., 2005). In order to exploit the full potential of LFT materials these local variations have to be taken into account for adequate material modeling and structural analysis (Goris et al., 2016).
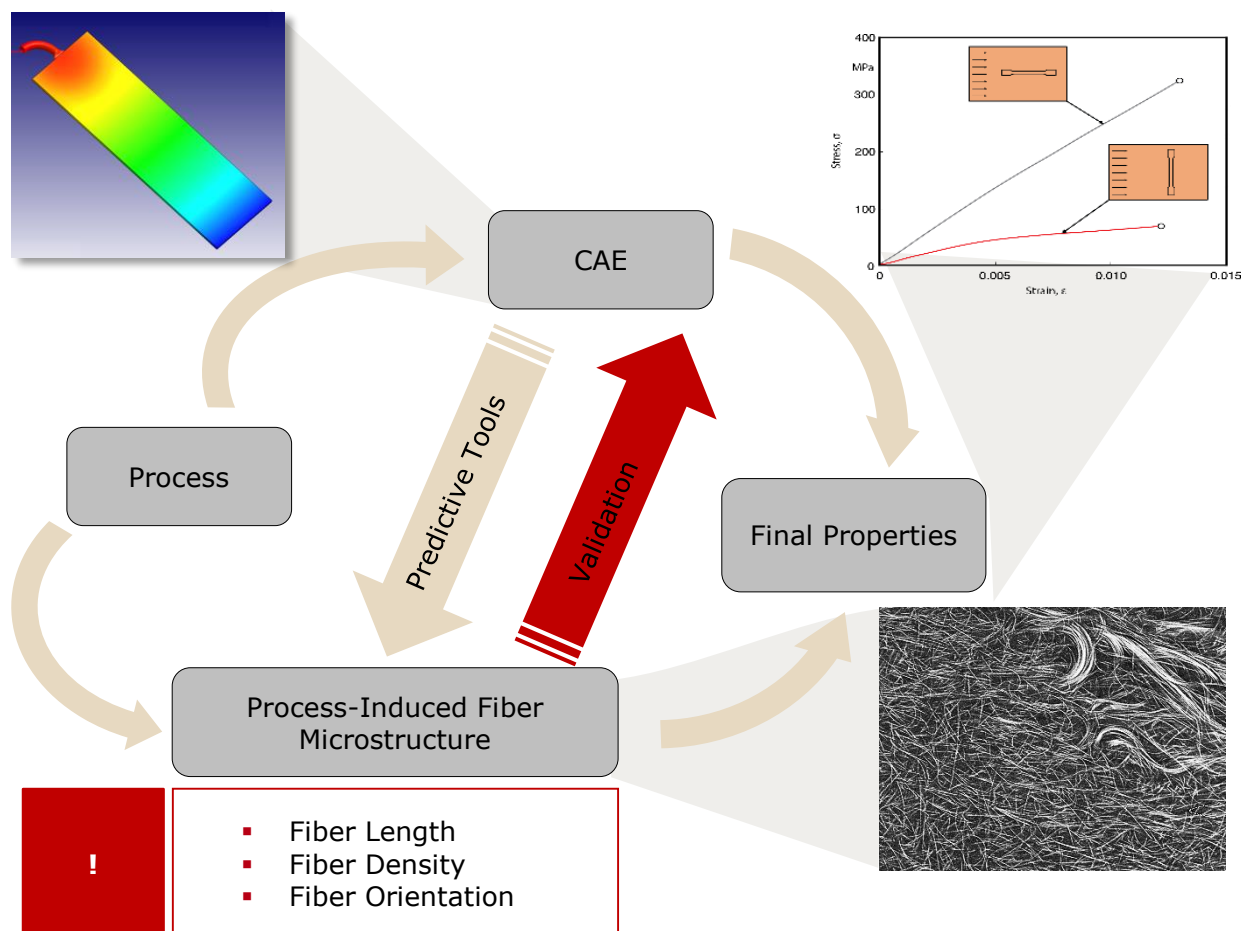
Figure 1: Schematic of the process-structure relationship (Goris, 2016).

In particular, fiber attrition in polymer processing is still not fully understood and difficult to control (Phelps et al., 2013). Along the entire process line, the fibers are subjected to severe stresses that cause the fibers to bend, buckle and break.

The main focus of this work is on studying fiber breakage of LFT materials in simple shear flow using a highly controlled experimental setup in a form of a Couette rheometer. This setup is conceptualized to isolate and evaluate the effects present in LFT processing under controlled conditions.

In the second part of this work, injection molded plaques are investigated in terms of fiber breakage and fiber-matrix separation. The local FL is measured and analyzed along the flow path. The FD is investigated through the thickness of the sample using micro computed tomography (µCT) scans. Ultimately, the correlation between the two microstructural properties is investigated.

The third part of this work addresses the prediction of fiber breakage for LFT materials using process simulation. In order to use LFTs efficiently and safely for automotive applications, there is a need to develop process simulation and constitutive models as well as computational tools to predict the process-induced microstructure of the composite, and the resulting properties of the molded part. Therefore, the data set generated with the controlled Couette rheometer trials will be utilized to validate a continuum model for fiber breakage prediction (Phelps Model) that is currently implemented in commercially available software packages. Validating and being able to confirm that the model can accurately predict the fiber breakage is important, because no comprehensive validation for any fiber breakage model exist at this point. The Phelps model is based on three fitting parameters, which may be assumed to be material dependent to use it as a predictive tool. Hence, the model should be able to predict fiber breakage for the same material with one set of parameters. Although this is an important aspect of the continuum model in order to use it as a predictive tool, the material dependency of the model parameters has never been verified. Therefore, the present work aims to gain a more fundamental understanding on the model parameters to fully verify their material dependency (Goris et al., 2016, Nguyen et al., 2015a, Phelps et al., 2013). Furthermore, the model parameters are used as an input for a Moldex3D simulation to determine the fiber breakage of an injection molded plaque and compared to the measured FL.

Another emphasis of fiber breakage modeling will be on a single particle model. Therefore, the measured data from the Couette rheometer experiments will be used to validate a recently published single particle model for fiber breakage predictions (Perez, 2016).

All those approaches covered in this thesis help to achieve a higher level of understanding the process-induced fiber microstructure and therefore increase the confidence level and the quality of LFT parts to make light weight polymer composites available to a wider range of applications.

1.2 Fiber Breakage Phenomena

1.2.1 Introduction

LFT materials consist of a thermoplastic matrix material, such as polyethylene, polypropylene, polyvinylchloride or polystyrene, and the reinforcing fibers. The function of the matrix material is to provide a medium for binding and holding the reinforcing phase, to protect the fibers from environmental damage and to transfer stresses to the fibers (Ha, 2015, Balasubramanian, 2011, Rhode et al., 2011, Schatt, 1983, Wambua et al., 2003, Larbig et al., 1998, Mallick, 2007, Wang et al., 2011). Glass fibers are currently the most preferred reinforcement material in thermoplastics due to their availability, their low cost, their capability of being economically processed by different manufacturing processes, their high specific strengths and their corrosion stability (Wang et al., 2011). The purpose of introducing a fiber into a polymer is to enhance the mechanical properties of the composite since the load is transferred from the weaker material (=matrix) to the reinforcing phase (=fiber). The term load describes external forces which act as shear stresses on the fiber-matrix interface. In order to introduce the full reinforcing effect of the fibers in the compound it is important that the fibers are longer than a critical FL which is described as follows (Stelzer, 2003, Osswald, 2011):

$$l_{crit} = \frac{\sigma_F d_F}{2\tau_{Gr}}$$

Equation 1: Critical fiber length (l_{crit}), with σ_F as the fiber tensile stress, d_F as the fiber diameter and τ_{Gr} as the shear stress acting on the fiber/matrix-interface, respectively (Kelly and Tyson, 1965, Kelly, 1966).

If fibers are shorter than their critical FL, the stress in the compound do not reach the fiber tensile strength and the fibers do not fail. Instead the matrix fails, because the length of the fiber is not sufficient to transfer the entire load to the

fiber. In case the fibers are equal or longer than their critical FL, the loads can be fully transferred to the fiber. The fibers deform elastically until the stresses in the system exceed the strength of the fibers resulting in fiber failure. This immediately leads to matrix failure and, thus, failure of the entire composite. Fibers with a length that equals the critical FL result in a perfect utilization of the FL meaning that the fiber breaks just barely before fiber pull-out. It is important to note that fiber breakage during processing always results in degradation in FL, which leads to a fiber length distribution (FLD). Therefore the aim in processing LFTs is to maximize the FL well above the critical FL (Osswald, 2011, Rhode et al., 2011, Cox, 1952, Stelzer, 2003, Simon, 2016).

1.2.2 Injection Molding and Process-Induced Fiber Breakage

Injection molding of LFTs is a widely used process to manufacture plastic products with advanced mechanical properties at low costs. Furthermore, the process is ideally suited to manufacture mass produced parts of complex shapes requiring precise dimensions (Zhang and Thompson, 2005, Osswald, 2011, Strong, 2000). The basic principle of the injection molding process is as follows: LFT pellets are fed through a hopper into the first part of the plasticating unit, the conveying zone. In this zone the raw material is transported from the hopper to the screw channel. Once the material reaches the screw channel it experiences compaction and transportation down the channel. It is important to note that the compaction process is only possible if the friction at the barrel surface exceeds the friction at the screw surface. The second zone of the plasticating unit is the transition zone where the material melts due to shear. Subsequently, the melt enters the metering zone which is responsible for accumulating and homogenizing of the material. As soon as sufficient material is accumulated, the injection molding cycle starts by closing the mold. The polymer is injected in the mold cavity. Once the cavities are filled, a holding pressure is maintained to compensate for material shrinkage. In the next step the screw reciprocates, feeding the next shot to the front of the screw. As soon as the part is sufficiently cooled down and reached dimensional stability, the mold opens and the part is ejected (Osswald, 2011, Simon, 2016). The scheme of an injection molding process including the process cycle is shown in Figure 2.

Over all stages in the injection molding process, the fibers are subjected to extensive stresses that inevitably cause fiber breakage. While the initial length of the fibers might be uniform, fiber attrition results in a distribution of FLs in the finished part. The degree of fiber breakage is determined by the process, the processing parameters, the mold design and the material. Several research groups showed that the initial FL cannot be preserved under any circumstances (Turkovich and Erwin, 1983a, Yilmazer and Cansever, 2002, Wang et al., 2011). Moreover, FL measurements in injection molded parts suggest a total reduction in initial FL of about 82 up to 98 %. A summary of published research studies on fiber degradation in injection molding are given in Table 1 and Table 2.
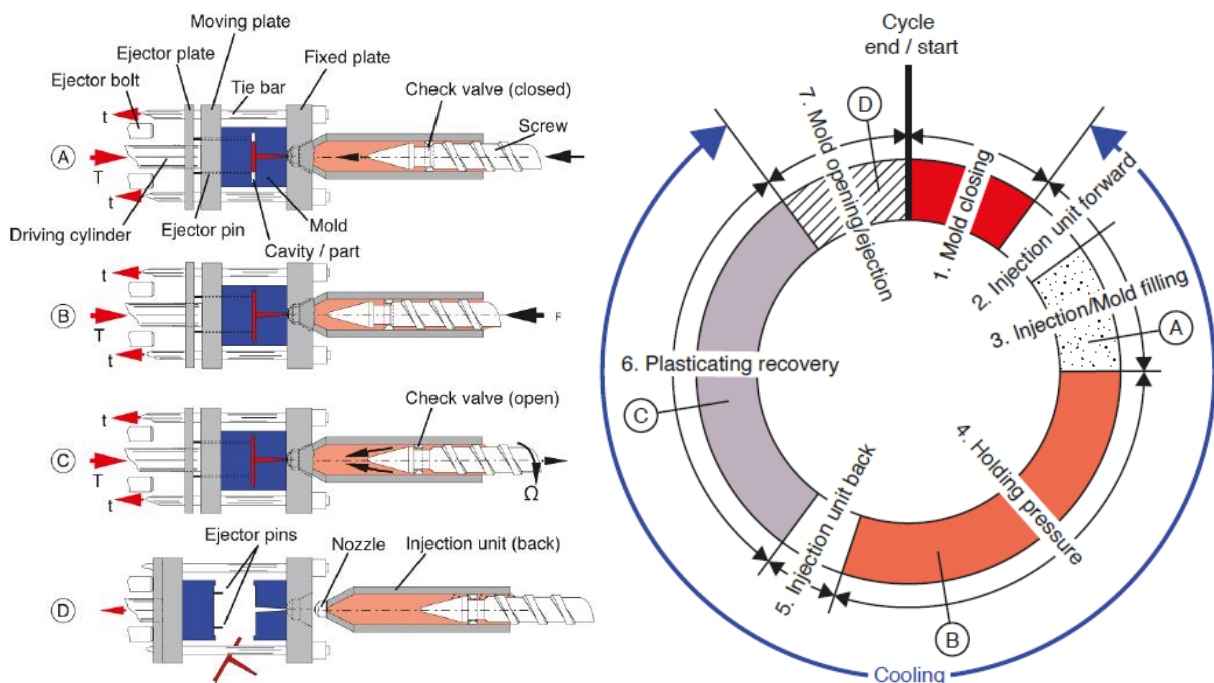
Figure 2: Sequence of events during an injection molding cycle. Right: Injection molding cycle (Osswald, 2011).

There is a general consent, that fiber breakage can be attributed to four main mechanisms, namely solid-melt-fiber interactions, fiber-wall interactions, fiber-fiber interactions and hydrodynamic stresses induced by the matrix rheology (Gupta et al., 1989, Turkovich and Erwin, 1983b).

The solid-melt-fiber interaction occurs at the beginning of the polymer process when the pellets are partially fused and the solid-fiber interaction leads to large bending stresses within the fibers.

Table 1: Evolution and change in average FL of FRT during injection molding process. (*) representing the number average FL.

Material description	Initial FL [μm]	FL in the feed zone [μm]	FL in the compression zone [μm]	FL in the metering zone [μm]	FL in the melt [μm]	Total reduction of FL [μm]	[%]	Reference
Long glass fiber reinforced PP*	3200	No data available	~2513	~550	~425	~2775	~87	(Turkovich and Erwin, 1983a)
Short glass fiber reinforced PP	350	~250	~225	~200	~160	~190	~55	(Patcharaphun and Opaskornkul, 2008)
Long glass fiber reinforced PP	7000	~3955	~1115	~709	(~800)	~6291	~90	(Patcharaphun and Opaskornkul, 2008)
Long glass fiber reinforced PA*	~7700	~7700	~3100	~1800	~1500	~6200	~81	(Moshe et al., 2012)

Table 2: Comparison between initial average FL and FL after processing to quantify the degree of fiber attrition. (*) representing the number average FL.

Material description	Processing conditions	Initial FL [μm]	FL after processing [μm]	Total reduction of FL [%]	Reference
Long glass fiber reinforced PP*	Injection molding. Screw speed: 30/50/70 RPM	**3175**	30 RPM: **584** 50 RPM: **432** 70 RPM: **482**	30 RPM: **82** 50 RPM: **86** 70 RPM: **85**	(Turkovich and Erwin, 1983a)
Long glass fiber reinforced PP*	No data available	**3175** (Sampling location 1), **4532** (2), **6350** (3), **3175** (4), **4572** (5), **6350** (6)	1: **508**, 2: **838**, 3: **736**, 4: **635**, 5: **685**, 6: **685**	1: **84**, 2: **82**, 3: **88**, 4: **86**, 5: **89**	(Turkovich and Erwin, 1983a)
Long glass fiber reinforced Nylon-6 (30 wt%)*	Injection molding. Screw speed: 250/300/350. Feed rate: 70/80/90 kg/h	**4500**	250/70**: 141**, 250/80: **134**, 300/70: **104**, 300/80: **119**, 300/90: **114**, 350/70: **146**, 350/80: **120**, 350/90: **115**	250/70: **97**, 250/80: **97**, 300/70: **98**, 300/80: **97**, 300/90: **97**, 350/70: **97**, 350/80: **97**, 350/90: **97**	(Yilmazer and Cansever, 2002)
Long glass fiber reinforced PP (20 wt%)	Static packing injection molding + Dynamic packing injection molding (oscillatory shear, 10 s^{-1})	**10 000**	Number/weight average FL Static: **1150/1340** Dynamic**: 830/950**	Number/weight average FL Static: **89/87** Dynamic: **92/91**	(Wang et al., 2011)
Long glass fiber reinforced PP (20 wt%)*	Injection molding. Presence of a chemical blowing agent (foam processing). Processing temperature: 230 °C	**640**	Average FL 0 wt% CBA – **350** 5 wt% CBA – **535**	0 wt% CBA – **45** 5 wt% CBA – **16**	(Zhang and Thompson, 2005)

The term fiber-wall interaction describes fiber collisions with adjacent objects. Adjacent objects are solid walls of the equipment like the barrel surface, the screw surface and the cavity walls. These interactions lead to abrasion and friction between the fibers and the walls and therefore trigger stress concentrations within the fibers. According to Ren et al., 2014 the interaction between the fibers and the screw is weaker than that between the fibers and the barrel surface due to the presence of the resin melt and due to the reason that the roughness of the barrel surface is greater than those of the screw surface (Ren and Dai, 2014). Inoue et al., (2013) observed that the screw size and screw diameter does not affect or has little effect on the fiber breakage in the channel, but the screw geometry affected the residual FL in the finished part. If using screws with increased flight depths the shear stress is reduced and therefore increases the residual FL (Shon and White, 1999, Ramani et al., 1995, Inoue et al., 2015).

Fiber-fiber interactions describe fiber collisions and interactions with adjacent fibers. In all industry relevant applications, the concentration of the fibers range from 20 % to 60 % by weight. It is important to note that the higher the fiber concentration (FC), the better the mechanical properties of the finished parts but the more fiber collisions occur during processing (Servais et al., 1999, Zhang and Thompson, 2005). It can be assumed that an increase in FC correlates with more fiber collisions, which ultimately result in an elevated FL degradation (Zhang and Thompson, 2005).

Another mechanism attributed to fiber breakage are fiber-melt interactions, which describe the influence of the matrix rheology on the fibers. Fibers are embedded in the thermoplastic matrix, which introduce hydrodynamic stresses acting on the fibers during processing. Furthermore, viscosity and pseudoplasticity of the matrix play a role in the degree of fiber breakage. It is assumed that the viscosity of the composite material has a direct impact on fiber attrition (Zhang and Thompson, 2005). One way to reduce fiber breakage is to decrease the suspension viscosity by increasing the melt temperature. Nevertheless it is important to note that the increase in melt temperature is limited due to the fact that high temperatures result in polymer degradation and longer cooling cycles (Shimizu et al., 1997, Zhang and Thompson, 2005, Turkovich and Erwin, 1983a).

1.2.3 Couette Rheometer Design

1.2.3.1 Introduction

A Couette flow is defined as a two-dimensional laminar steady flow of a fluid between two concentric infinitely long cylinders with one cylinder rotating relative to the other. The emerging circular annular flow is a drag flow. This type of rheometer is commonly used for materials which contain suspended solids, such as fibers embedded in a polymer matrix (Clark, 2016). The investigated material is filled in the gap between the inner and outer cylinder. With a known torque and revolutions per minute, the viscosity can be determined. It is important to note that if the ratio of the two cylinder diameters is close to one (annular gap is small), the shear rate nearly becomes uniform in the gap and thus approximates that in steady simple shear flow (Dealy and Wang, 2013, Lai et al., 2010).

The Couette rheometer used in this study was developed at the Polymer Engineering Center (PEC), University of Wisconsin-Madison, particularly to study the fiber degradation of LFT materials under controlled conditions. As it can be seen in Figure 3 the fiber filled material is placed in the annular gap and is subjected to a continuous planar shear flow. The rheometer was specially designed to control the temperatures, processing speeds and residence times. This particular setup not only enables highly controlled conditions but also allows to isolate the effects of processing conditions on fiber breakage. The dimensions of the setup are characteristic of common plasticating units of injection molding machines.
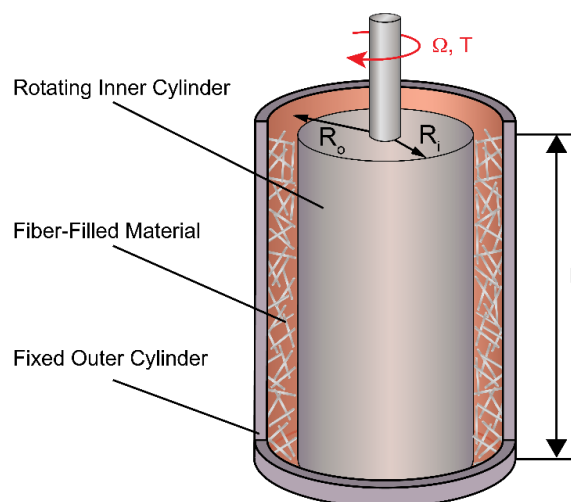
Figure 3: Couette rheometer used in this study to process LFTs (adapted from Osswald and Rudolph, 2015).

The advantges in using this particular Couette rheometer setup are i) the shear rate is nearly constant for large radii, ii) that thermoplastics with short and long fibers can be used iii) there is an analytical solution for the flow and iv) the highly control. Disadvantges include that the rheometer i) cannot be used for high viscosity polymer melts, that ii) loading and cleaning is a difficult endeavor, that iii) a large sample volume is required and that iv) high shear rates result in an unstable fow due to centrifugal forces. Furthermore, non-uniform flow can occur due to end effects, secondary flows (Taylor vortices) and shear heating. End-effects are responsible for the deviation of the measured apparent viscosity from its actual value (effect on the torque) and are at the moment the major source of error in concentric cylinder rheometers. These effects can be minimized by providing a large gap between the inner cylinder and the outer cylinder. But it is important to note that a big gap size can lead to variations of the shear rate and particles (fibers) might migrate radially outward (Osswald and Menges, 2012, Hamedi, 2015, Manias, 2016, Clark, 2016, Morris and Boulay, 1999).

1.2.3.2 Parameters and Underlying Equations

During a Couette rheometer trial the torque (T) and the rotational speed (Ω) can be easily measured. T can also be calculated according to Equation 2:

$$T = \pm e_z \frac{4\pi\eta r_i^2 r_o^2 (\omega_i - \omega_o)}{r_o^2 - r_i^2}$$

Equation 2: Torque T, where e_z is the vector unit in the positive direction of the z axis, η the viscosity of fiber-polymer suspension, r_i the radius of the inner cylinder, r_o the radius of the outer cylinder, ω_i the angular velocity of the inner cylinder and ω_o the angular velocity of the outer cylinder, respectively (Osswald and Menges, 2012).

T is related to the shear stress (τ) and acts on the inner cylinder wall. τ can be computed as follows:

$$\tau_i = \frac{F}{A} = \frac{T}{2\pi r_i^2 l}$$

Equation 3: Shear stress τ_i, where F is the force applied, A the cross sectional area, T the torque, r_i the radius of the inner cylinder and l the length of the inner cylinder, respectively (Osswald and Menges, 2012).

For a power-law fluid the shear rate ($\dot{\gamma}$) at the inner wall can be calculated according to Equation 4:

$$\dot{\gamma}_i = \frac{2\Omega}{n(1 - (r_i/r_o)^{2/n})}$$

Equation 4: Shear rate $\dot{\gamma}_i$ at the inner wall of the Couette Rheometer, where Ω is the rotational speed, n the power law index, r_i the radius of the inner cylinder and r_o the radius of the outer cylinder, respectively (Osswald and Menges, 2012).

From τ and $\dot{\gamma}$ the viscosity of the fiber-polymer-suspension (η) can be calculated according to Equation 5:

$$\eta = \frac{\tau_i}{\dot{\gamma}} = \frac{\tau r_{as}}{4\pi^2 r_i^3 l \omega_i}$$

Equation 5: Viscosity η, where τ_i is the shear stress, $\dot{\gamma}$ the shear rate, τ the torque on the inner cylinder, r_{as} the radius of the annular space between the inner- and the outer cylinder, r_i the radius of the inner cylinder, l the length of the inner cylinder and w_i the angular velocity of the inner cylinder, respectively (Osswald and Menges, 2012).

1.2.3.3 Mathematical Description of the Couette Flow Field

The circular annular Couette flow is schematically depicted in Figure 4. Assuming a laminar flow with perfect concentric cylinders and using cylindrical coordinates (r, θ, z) it can be assumed that there is no flow in r and z direction. The only velocity component left is u_θ which varies in r. The velocity field can therefore be described as follows:

$$u = (0, u_\theta(r, 0_\theta, 0_z), 0)$$

Equation 6: Velocity flow field in simple shear flow of a Couette rheometer.

The continuity equation for an incompressible flow therefore reduces to:

$$\frac{\partial u_\theta}{\partial \theta} = 0$$

Equation 7: Reduced continuity equation for an incompressible flow.

Since gravity forces can be neglected and there is no pressure, the present flow field is generated by the drag flow caused by the rotation of the inner boundary. θ of the equation of motion gives an insight into the velocity field:

$$0 = \left[\frac{1}{r^2} \frac{\partial}{\partial_r} (r^2 \tau_{r\theta}) \right]$$

Equation 8: Reduced momentum balance.
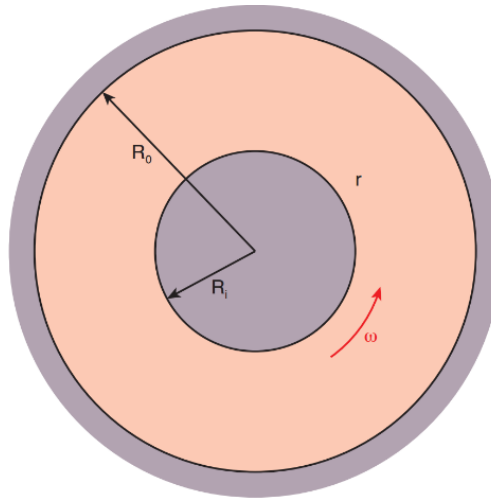
Figure 4: Planar Couette flow, where R_o is the radius of the outer cylinder, R_i the radius of the inner cylinder and ω the rotational speed (Osswald and Rudolph, 2015).

The Power Law model from Ostwald and de Waele is then used as the constitutive model to solve the flow field inside the Couette device. The shear stress tensor ($\tau_{r\theta}$) can be written as:

$$\tau_{r\theta} = m \left(\frac{\partial u_\theta}{\partial r} \right)^n$$

Equation 9: Shear stress tensor obtained by inserting the rθ component of the rate of deformation tensor into the Power Law model.

In order to fully account for the velocity field boundary conditions (BC) for the inner- and the outer cylinder are needed:

$$BC1 = \frac{u_\theta}{r = R_o} = 0$$

Equation 10: BC1 is based on the assumption that the flow velocity of the melt is zero at the outer wall since polymer freezes at the wall and therefore flow velocity becomes zero.

$$BC2 = \frac{u_\theta}{r = R_i} = \omega R_i$$

Equation 11: BC2 assumes that the flow velocity near the inner cylinder is identic to the angular velocity of the inner cylinder.

After solving all the equations the velocity flow field u_θ can be written as (for more details refer to Osswald et al., 2015):

$$u_\theta(r) = \omega r \frac{\left[1 - \left(\frac{r}{R_o}\right)^{-\frac{2}{n}}\right]}{\left[1 - \left(\frac{R_i}{R_o}\right)^{-\frac{2}{n}}\right]}$$

Equation 12: Velocity flow field u_θ in a Couette rheometer.

1.2.4 Characterization Techniques

1.2.4.1   Fiber Length Measurement

Comprehensive experimental and simulation studies are necessary to obtain the required understanding of the fiber breakage mechanisms present in LFT processing. One crucial aspect is to utilize a precise, consistent and reproducible measurement technique to obtain reliable experimental data. The data is necessary to quantify the impact of processing conditions on fiber breakage, which are the basis to understand the fiber breakage phenomena and to develop proper predictive models (Latimer et al., 2008, Kunc et al., 2007b).

Although this topic has been addressed by varying research groups, it is important to note that there is still no standardized method to measure the FLD of a sample and the characterization of the FLD of fiber-filled materials still remains a challenging task. Even small samples can consist of millions of fibers, which make the length determination extremely cumbersome. A wide variety of measurement concepts exist, but no industry standard has been defined yet (Kunc et al., 2007b). The large majority of measurement techniques are destructive test methods that involve a composite coupon extraction step, the removal of matrix material either by chemical decomposition or pyrolysis, fiber sample isolation and dispersion as well as digital imaging and individual filament length measurement (Kunc et al., 2007b, Rohde et al., 2011). Examples of FLD determination techniques used by different research groups are summarized in Table 3.

For decades the measurements were performed completely manually by selecting single fibers with tweezers and placing them under a microscope. The length of the fibers was then determined from a digital by manually selecting the endpoints

Table 3: Examples of FLD determination techniques for various LFTs (with RTD as Residence time distribution, respectively).

Material description	Dimension of extracted sample	Matrix burn-off (Muffle furnace)	Fiber dispersion technique	Measurement technique of FL	Number of fibers measured	Presentation of FL-measurement results	Reference
Short glass fiber reinforced PP	Injection molded granules	600 °C for 1 h	Glass dish with distilled water	Manually (Microscopic analysis + SigmaScan Image analysis software)	No data available	Cumulative FLD	(Zhang and Thompson, 2005)
Long glass fiber reinforced PP	No data available	No data available	Organosilane	Semi-automatic (Microscopic analysis + Image-Pro Plus Software)	>2000	Weight average FL of fibers along the screw pitches	(Ren and Dai, 2014)
Long glass fiber reinforced PP	Extrudate was processed into plates of requested size	500 °C for 4 h	Silicone-water	Semi-image analyser system	>800	Data was used to associate with parameters of RTD model	(Zhuang et al., 2008)
Glass fiber reinforced Nylon6	Extruded granules and injection molded test specimen	650 °C for 30 min	Glycerine	Microscopic analysis + automatic length measurement	>2000	FLD by weight/ number	(Yilmazer and Cansever, 2002)
Short glass fiber reinforced PA	Collected samples after compounding	800 °C for 1 h	Glycerin-water	Manually (Microscopic analysis)	>400	Change in FLD by fiber fraction	(Inceoglu et al., 2011)
Long glass fiber reinforced PP	Molded test pieces	Electric oven at 600 °C for x min/h	water	Microscopic analysis	>1000	Probability density distribution of FLs	(Inoue et al., 2015)
Long glass fiber reinforced PP	Specimen of a size of 70x40x3 mm^3	No data available	No data available	Semi-automatic/ automatic (Image analysis software FASEP®)	No data available	Probability density distribution versus aspect ratio	(Garesci and Fliegener, 2013)
Long glass fiber reinforced PP	Center-gated disk specimen and ISO plaque	450 °C	Glass Petri dish	Manual (Scanner + Image J Software)	>2000	FLD by weight	(Kunc et al., 2007b)

of the fibers in an image processing software. These measurements can easily result in skewed FLD due to the small sample size as well as influence of human error (Kunc et al., 2007b, Rhode et al., 2011, Latimer et al., 2008). Today there are several sophisticated image processing algorithms available to analyse the scanned image, like the Chord Length Transformation (FASEP, Germany), the Image-Pro Plus Algorithm (Media Cybernetics, USA), the CT-Fire (UW-Madison, USA), FiVer (SKZ, Germany), the STAMAXTAT Method (SABIC, Netherlands) and the Marching Ball Algorithm (PEC, USA). Commonly used FL measurement techniques are presented in the following paragraphs.

FASEP is a complete measurement system that includes a semi-automatic image processing software which is divided into the following steps: i) Pyrolysis to separate the fibers from the matrix, ii) dispersion of the fibers in an adequate liquid (distilled water and glycerine), iii) series of dilution preparation, iv) generation of a digital image and v) digital image analysis. The digital image analysis contains a conversion of the input image to a grey scale image and an improvement of the contrast as well as an object recognition. In the pattern recognition step a classification of objects into dust particles, single fibers and fiber clusters take place. The classification is based on the shape of the object as well as on the fact that fiber clusters are always bigger than individual fibers and that they have more than two endpoints. In course of this procedure objects that do not show the anticipated fiber shape and which are neither classified as individual fiber nor as fiber cluster are identified as "dust" and excluded from following calculations. Single fibers that are fully isolated in the image can be detected and measured automatically, whereas crossed fibers need a manual cluster separation in order to be able to measure their length (=semi-automatic analysis of crossed fibers). The fiber cluster images are binarized and the white pixels are displayed in the Hough space. From the occurring maxima in the Hough space the single fibers can be calculated and can be distinguished by a colored overlay. The detected fibers can now be measured (Höhn, 2016, Mörl, 2016). 3000-9000 individual recovered fibers per sample are measured (Ayotte and Bund, 2008, Tan et al., 2015). An additional module (ALF algorithm) which can be purchased in combination with FASEP promises to be able to measure even bent and crossed fiber clusters (Höhn, 2016, Mörl, 2016).

The Saudi Arabia Basic Industries Corporation (SABIC) uses a proprietary measurement technique, called STAMAXTAT, to analyse the FLD of LFTs. In a first

step, a defined sample (dimensions 12 mm x 12 mm x thickness of the specimen) is extracted from the molded part and the matrix is removed by pyrolysis. Subsequently, all fibers of the sample are measured without a down sampling step. The fibers are manually dispersed on a scanner using brushes and tweezers and a digital image is generated. A fully automated image processing algorithm detects all fibers without manual input by the operator. The measurement technique allows a full analysis of all fibers in a sample without skewing the results due to down-sampling or partial measurement of a fiber sample. However, the manual dispersion is a time intensive step that due to the sample size of 350,000 to 750,000 fibers per sample can take up to 8 hours per sample. Also, the relatively small sample size before pyrolysis may cause error in the analysis, because extracting the samples cuts fibers and can result in a lower average FL.

At the PEC, University of Wisconsin-Madison, a new measurement technique was developed that uses a time-efficient fiber dispersion technique and an image processing algorithm that can automatically detect fibers in a digital image (Goris and Osswald, 2016). The image processing algorithm, called the Marching Ball Algorithm, is based on the work by Perez et al., 2013 and can detect single fibers as well as curved and intersecting fibers, which is particularly important for LFTs (Perez et al., 2013). The algorithm is currently implemented in MATLAB R2016a and takes as an input a scanned image containing fibers. After all endpoints are found and marked a "marching ball" is created at one end and marches along the fiber to measure its length. A more detailed explanation on the single steps of the Marching Ball Algorithm can be found in Table 4.

Detected fibers are marked by a colored overlay. The results from a Marching Ball analysis are shown in Figure 5. It can be seen that the algorithm is able to deal with complicated features such as bent fibers, intersecting fibers or fibers which cross at the same point. This is really important for the analysing of LFTs. Nevertheless, it can be seen in Figure 5 that the algorithm also dismisses some fibers or only measures fibers partially. This occurs due non-uniform illumination of the fiber sample during scanning. Thus, the thresholding becomes challenging and fibers are segmented into pieces and therefore cannot be detected as a single fiber. Furthermore, two perfectly aligned fibers might be identified as a single long fiber. However, according to Perez et al., 2013 this error only represents an estimated 5 % deviation in the calculated average FL (Perez et al., 2013).

Table 4: Principle of the Marching Ball Algorithm (Perez et al., 2013).

Endpoints of the fibers are found by first skeletonizing the objects in the image and removing any branches that do not represent actual endpoints of the fibers.	
An artificial marching ball that has a predefined radius is created at one endpoint. A set of potential marching directions is generated.	
The marching directions are evaluated and the ball marches to the direction where he encounters more white pixels.	
The ball marches forward to its new position.	
At the new position possible marching directions are evaluated again. If more than two possible directions have the same white pixel quantity the marching ball compares the possible marching directions which the previous one.	
The ball will move along the direction, which is most similar to that of the previous jump.	
The algorithm continues the previous step until an endpoint is reached. The fiber has been successfully detected and its length can be computed from the marched path in pixels and the resolution of the image.	
At potentially ambiguous marching directions (=intersecting fibers) the ball evaluates all possible marching directions and jumps to the position which is most similar to that of the previous one. This step ensures that the ball continues marching the same fiber it started with since fibers commonly do not show any substantial curvature.	
The ball marches till he reaches the neighborhood of an endpoint. So the algorithm is able to detect and successfully identify intersecting fibers.	
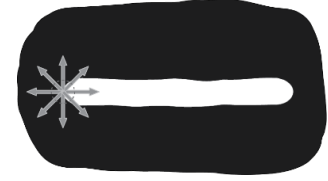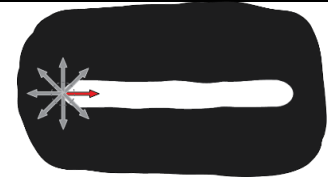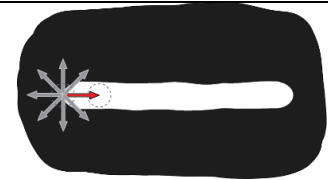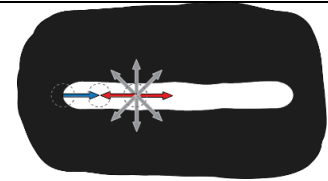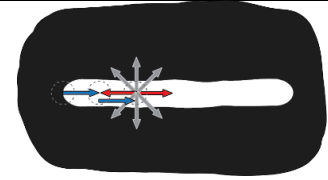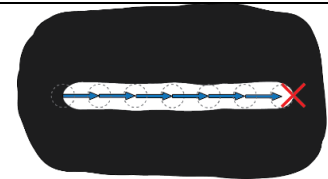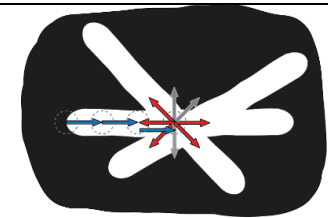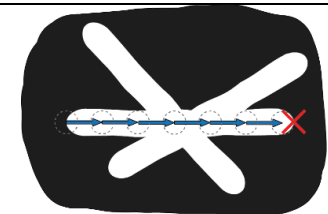
Moreover, the error decreases even further with the amount of fibers that are measured. At 15,000 to 25,000 fibers, the potential error is decreased to less than 2 %.
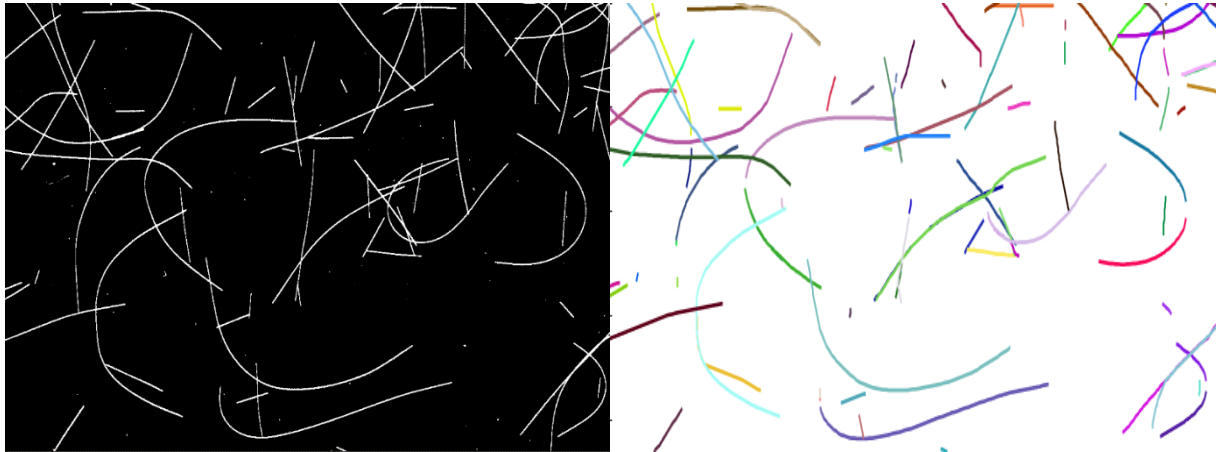
Figure 5: Illustration of the Marching Ball Algorithm, i) Binary image form the scan and ii) detected fibers.

1.2.4.2 Micro Computed-Tomography

Micro computed-tomography (µCT) is an X-ray transmission image technique, which can be used to analyze the microstructure of specimens. For LFT materials, the FO distribution and the FD distribution across the part thickness of samples can be quantified. µCT is a non-destructive testing method that provides three-dimensional reconstruction of the internal structure of an object to evaluate its micro-structural properties (Goris et al., 2016).

For a µCT measurement an X-ray source illuminates the specimen which is fixed on a rotating platform. The X-rays pass through the sample and are attenuated by the material. Depending on the configuration of the constituents of the sample, the energy of the X-rays is absorbed differently. A detector records the transmitted X-rays and produce a radiograph. It is important to note that the specimen is rotated (360 degrees) and stopped at predetermined angles. At each step a new projection image is taken. Subsequently, a full 3D representation of the sample can be generated by all radiographs (Figure 6) (Nguyen et al., 2015a, Goris et al., 2016, Goris and Osswald, 2016, MicroPhotonicsInc, 2015).

Due to differential absorption, which means that different materials have different absorption characteristics (glass absorbs radiation stronger than the polymer), a distinct contrast between the glass fibers and the thermoplastic matrix material

can be achieved in the projected image. This enables a determination of the local FD by using image processing algorithms (Nguyen et al., 2015a).
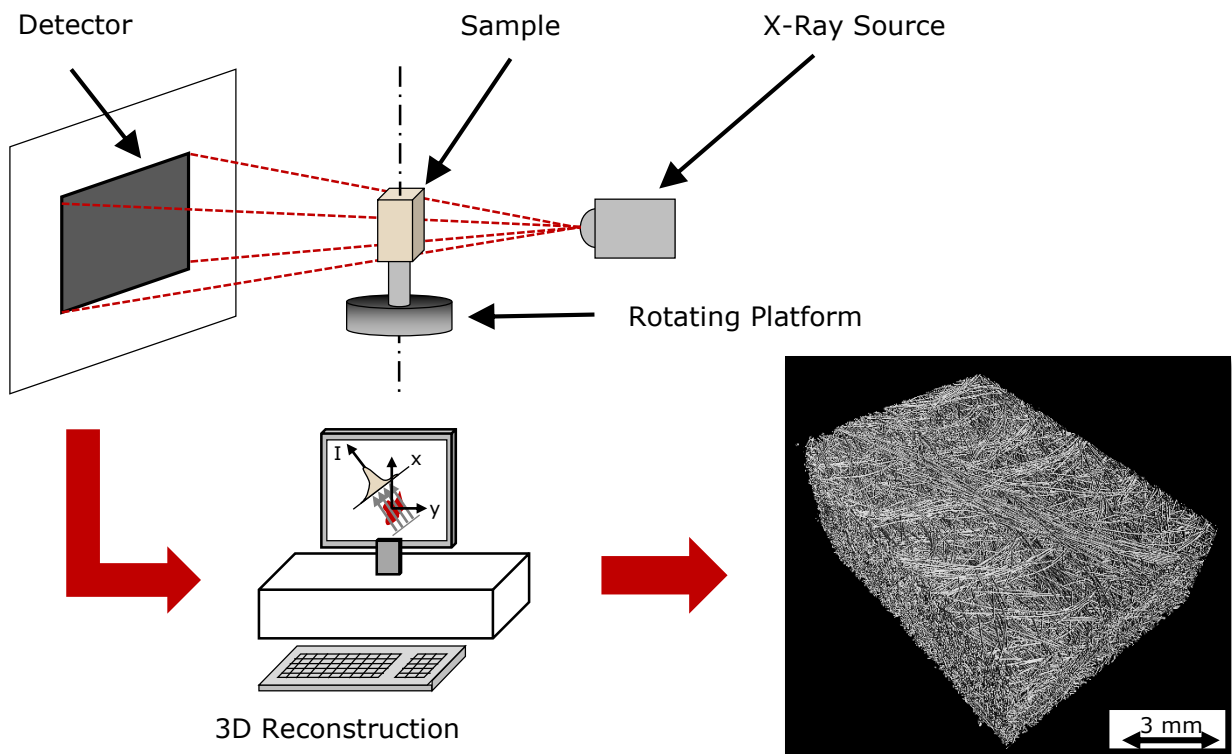
Figure 6: Schematic of the µCT system used in this study (Goris, 2016).

1.3 Fiber-Matrix Separation

Flow effects during mold filling lead to two fiber-matrix-separation effects in the finished part that result in a spatial variation of the FC. First, injection molded parts exhibit a FD distribution through the part thickness and, secondly, a local variation along the flow path can be found (Back, 2016).

Injection molded LFTs clearly reveal a shell-core-shell structure (Figure 7). The core region is in the center of the part and the shell regions are close to the mold walls. Various researchers found that fibers in the shell regions are oriented in flow direction whereas fibers in the core layer are aligned in cross flow due to the fountain flow in the mold (Velez-Garcia, 2012). Lafranche et al., 2005 noticed that the core thickness increases with increasing FL, since longer fibers impede the mobility of the fibers and therefore their ability to orient (Lafranche et al., 2005). Nguyen et al., 2015 further observed higher core widths at the end of an injection molded part (Nguyen et al., 2015b). Additionally, higher melt viscosities lead to a

wider core layer (Brast, 2001, Back, 2016). Furthermore, the FD is higher in the core of the part and lower in the shell layers (Zeng et al., 2015, Akay and Barkley, 1991, Toll and Andersson, 1993, Lafranche et al., 2005). This fiber distribution pattern over the part thickness might be explained with a phenomenon in fluid mechanics, namely the shear induced particle migration. This means that fibers migrate from high shear regions (near the mold wall) to lower shear regions (center of the part). This shear migration leads to a agglomeration of fibers in the core layer of the part (Goris et al., 2016, Morris and Boulay, 1999).

Zeng et al., 2015 demonstrated an increased FD in the core layer of an injection molded part of up to 50 % compared to the shell region (Zeng et al., 2015). Goris et al., 2016 findings agree with those presented by Zeng et al., 2015. The measurements also clearly demonstrated an increased FD in the core region of 30- up to 42 % compared to shell regions and therefore showed a substantial accumulation of fibers in the core region (Goris et al., 2016).
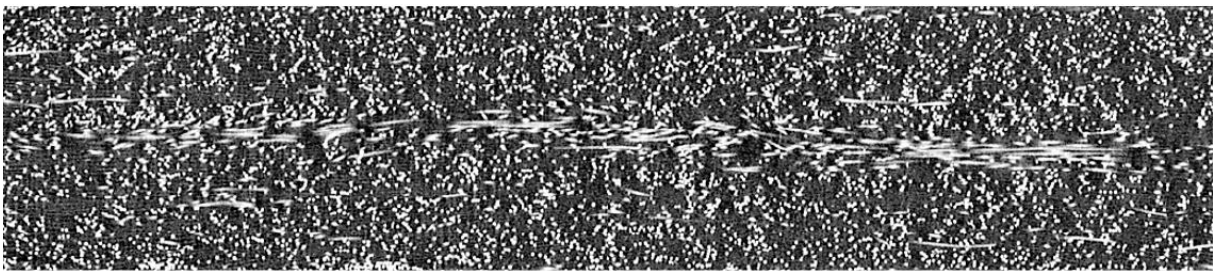
Figure 7: Cross section image of an injection molded part showing distinct core- and shell layers.

In addition to variations across the part thickness, a change in FD is also found along the lengthwise direction of injection molded parts. According to literature higher FC can be found at the end of the part. This results were confirmed by Lafranche et al., 2005 who found a relative increase of FD of about 21 % and Toll et al., 1993 reported an increase of 23 % (Lafranche et al., 2005, Toll and Andersson, 1993, Back, 2016, Goris et al., 2016).

Since there is not comprehensive explanation of fiber-matrix-separation published yet, potential mechanisms (Fiber Pull-Out and Fiber Breakage), which may explain the fiber agglomeration will be discussed briefly (Figure 8). The Fiber Pull-Out mechanism describes the effect that partially embedded fibers are pulled out of the solidified layers at the mold wall. The pulled out fibers are swept along with the molten core (Toll and Andersson, 1993). The Fiber Breakage mechanism

describes that the flow of the molten core shears off the partially embedded fiber. The broken fibers are then swept along with the core which leads to fiber agglomerations in the core and at the end of the part (Lafranche et al., 2005, Akay and Barkley, 1991). Furthermore, fiber-fiber interactions can also contribute to fiber matrix separation. However, no conclusive hypothesis or theory exists at this point.
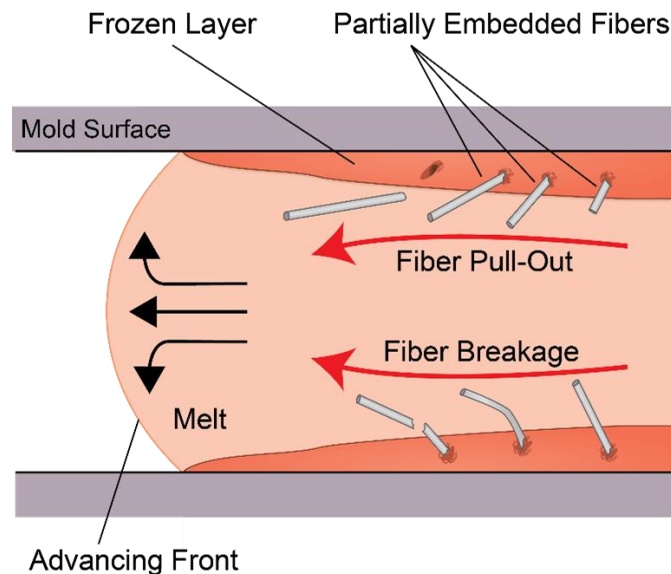
Figure 8: Melt flow during mold filling showing the two fiber matrix separation mechanisms, namely Fiber Pull-Out and Fiber Breakage, which may be responsible for FD variations in injection molded part (Goris, 2016).

1.4 Modeling and Simulation

1.4.1 Introduction

Computer-aided engineering (CAE) describes the application of computer software to simulate the manufacture of a part as well as the performance of a molded part in order to improve their design and/or to assist in the resolution of engineering problems (Siemens, 2016). The CAE approach provides the advantage of enabling designers and engineers to consider virtually any geometric and processing option (like to determine the effect of different gating scenarios, runner designs, cooling lines when designing an injection mold) without incurring the expense associated with prototype mold or die making or the material waste of time-consuming trials-and-error procedures. The objective is to validate new designs, processing conditions and material combinations in order to predict and fix issues before

beginning production. The first step of a CAE approach is to discretize the part domain into a finite element mesh that can be used to numerically solve the governing equations (Osswald, 2011). A variety of models exist to predict the fiber configuration after processing FRTs. These models can estimate FO, FL and FC separately. While FO models are widely established (Folgar and Tucker, 1984) the predication of fiber breakage has been addressed only recently (Phelps et al., 2013).

Severe fiber breakage occurs along all stages of FRT processing and the final FL in the finished part is reduced to a fraction of its initial length. Since the mechanical properties of FRT parts depend on the final length of the fibers, it is of vast interest to be able to predict and model the fiber breakage phenomena in processing FRT. The models used for fiber breakage prediction can be classified into continuum models and single particle models. The most prominent continuum models have a probabilistic approach for the breakage behavior which depends on the fiber characteristics (initial length, diameter, material properties, etc.) and the flow conditions (shear rate, viscosity, etc.). These phenomenological models for fiber breakage prediction have been recently implemented in commercial software packages. However, the performance and reliability has not been proven yet and no comprehensive validation has been published yet. Moreover, the dynamics of concentrated fiber suspensions are still not fully understood, which is partly caused by limitation in characterization techniques (Baur et al., 2014, Perez et al., 2016b). Besides continuum models, single particle simulation models resolve each fiber individually and take the interactions between the phases into account. The advantage of using these kind of models is their high accuracy in modeling the actual motion of fibers that is reached at the price of high computational costs and times (Strautins, 2008). The next chapters give a more detailed description on the models as well as the most popular and commonly used models are presented and explained briefly.

1.4.2 Continuum Model Approach

1.4.2.1 Phelps Model

The Phelps model is a phenomenological model to predict FL attrition during processing of discontinuous fiber reinforced composites. The Phelps model is

currently the only fiber breakage model that is implemented into commercially available simulation tools for injection molding (like Moldex3D and Moldflow).

The fundamental assumption of the Phelps model is that fiber breakage only occurs due to hydrodynamic forces acting on the fibers which cause them to buckle and ultimately to break. Additional forces which may arise from fiber-fiber contacts, like sliding or short-range hydrodynamic lubrication forces that act tangential to the fiber axis and normal forces that act perpendicular to the fiber axis, are not considered (Phelps et al., 2013).

The model is based on a conservation equation for the total FL (Equation 13) which is combined with a breakage rate (Equation 14) that is based on the buckling of fibers due to hydrodynamic forces (Equation 15) (Phelps et al., 2013).

$$\frac{dN_i}{dt} = -P_i N_i + \sum_k R_{ik} N_k$$

Equation 13: Basic conservation equation for FL, where N_i is the number of fibers of length l_i in a small volume of material, $-P_i N_i$ describes the number of parent fibers that break into children fibers of a specific length (breakage probability of parent fibers, term is negative since the number of parent fibers decreases) and $R_{ik} N_k$ represents the number of formed child fibers of a specific length (child generation) (Phelps et al., 2013).

In order to be able to develop the equation for R_{ik} it is assumed that the center-point of the fiber is the most likely location for buckling, but other locations along the fiber have also a non-zero probability of breakage. The probability density distribution is assumed to follow a Gaussian profile (Phelps, 2009):

$$R_{ik} = N_{PDF}\left(l_i, \frac{l_k}{2}, Sl_k\right)$$

Equation 14: Normal probability density function N_{PDF} for the variable fiber length l_i, with the mean $l_k/2$ and the standard deviation Sl_k, where l_k is the "parent" fiber length. The variable S represents a dimensionless fitting parameter which can be used to control the shape of the Gaussian breakage profile (Phelps et al., 2013).

$$P_{i=}\begin{cases} 0 & for \quad B_i < 1 \\ c_B \dot{\gamma}[1 - exp(1 - B_i)] & for \quad B_i \geq 1 \end{cases}$$

Equation 15: Breakage probability P_i, where C_B is the breakage coefficient, $\dot{\gamma}$ the shear rate and B_i the dimensionless variable for fiber buckling, respectively (Phelps et al., 2013).

The fiber buckling variable Bi is defined as:
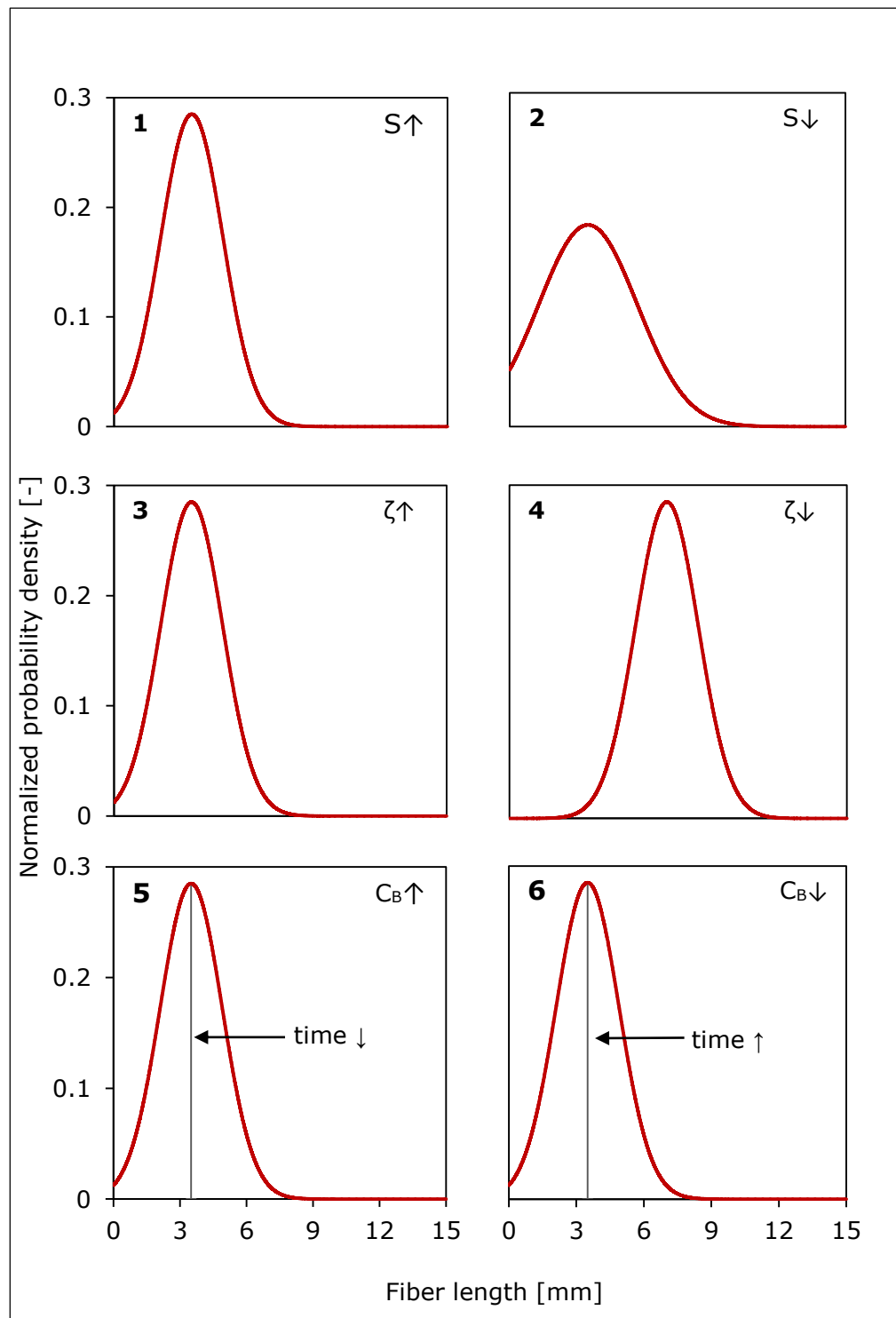
Figure 9: Influence of the three model parameters: the breakage coefficient C_B, the hydrodynamic drag coefficient ζ and the distribution shape factor S. Graph 1 and 2 demonstrate the influence of S, the higher S the sharper the peak. Graph 3 and 4 show the influence of ζ, the higher the value the more the peak moves towards left. Graph 5 and 6 display the influence of C_B, the higher the value the faster the steady state of the FLD is reached.

$$B_i = \frac{4\zeta\eta_m\dot{\gamma}l_i^4}{\pi^3 E_f d_f^4}$$

Equation 16: Dimensionless variable for fiber buckling B_i, where ζ is the tensorial anisotropic drag coefficient, η_m the matrix viscosity, $\dot{\gamma}$ the scalar magnitude of D ($\hat{D} = D/\dot{\gamma}$), l_i the fiber length, E_f the elastic modulus of the fiber and d_f is the fiber diameter, respectively (Phelps et al., 2013).

For $B_i<1$, the conditions that fibers are exposed to do not satisfy the buckling criterion and therefore the fiber does not buckle or break. If $B_i>1$ the processing conditions cause a fiber to buckle and might cause the fiber to break (Phelps et al., 2013).

Phelp´s model is based on three fitting parameters, namely the breakage coefficient (C_B), the hydrodynamic drag coefficient (ζ) and the distribution shape factor (S). ζ influences the location of the peak in the near-steady-state FLD. The higher the value the more the peak moves towards left. C_B controls the time required to reach that steady state. The higher the value the faster the endpoint (steady state) is reached. S influences the shape of the FLD. The higher the value the sharper (thinner) the peak, the lower the value the smaller and rounded the peak (Phelps et al., 2013). The influence of the three model parameters is shown in Figure 9.

Although Phelps model is the only commercially used fiber breakage model, it is based on the assumption that buckling is the only failure mechanism during processing FRTs. However, it has not been proven that this failure mechanism does apply for highly filled systems. Furthermore, bending can also be a potential failure mechanism and is not taken into account in this model. Another simplification in the Phelps model is the fact that it does not take fiber-fiber interactions into account and, thus, might not be applicable for concentrated suspensions. The model also does not require the FC as a material property input for the model. Lastly, Phelps model does not consider fiber defects (bubbles, cracks or necking of fibers) which are stress concentrators and might increase the probability of breakage.

1.4.2.2 Durin model

Another continuum model that was published around the same time, is the Durin´s Model, which is used to predict fiber breakage in the FLD along a twin-screw extruder (Durin et al., 2013). Durin's model is very similar to the Phelps Model.

Both models calculate the time evolution of the full FLD and both models assume that the only mechanism for fiber breakage is buckling due to hydrodynamic forces. Differences include that Durin et al., 2013 assign a non-zero probability of breakage to fibers with Bi<1 (Figure 10) and that a Weibull distribution is used to model the location of the breakage point instead of a Gaussian distribution. Furthermore, Durin´s model has only two fitting parameters, namely the shape parameter m and β_e which is the average aspect ratio for cylindrical objects. For more information on the differences between the two models one should consult Durin et al., 2013 and Phelps et al., 2013 (Durin et al., 2013, Phelps et al., 2013). It is important to note that the Durin model is not implemented in any commercial injection molding simulation package.
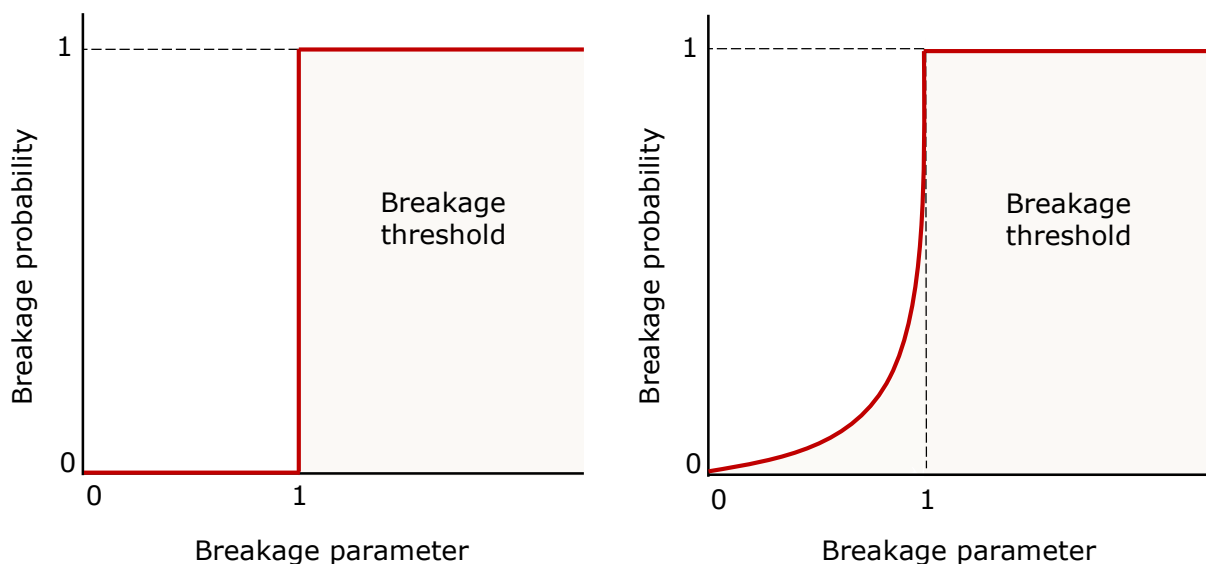
Figure 10: Probability of fiber breakage in Phelp´s model (left) and Durin´s model (right). In Phelp´s model if Bi<1 a fiber cannot break but if Bi>1 the fiber snaps. In contrast Durin et al., 2013 assign a non-zero probability of breakage to fibers with Bi<1 since real fibers present defects which are weak points and therefore may trigger possible break-ups below the critical stress value (Durin et al., 2013, Phelps et al., 2013, Bechara, 2016).

1.4.2.3   Baird model

Baird´s breakage model is a continuum model, which is based on a semi-flexible orientation model. A fiber is represented as two adjacent vectors **p** and **q**, with an internal resistivity to bending (Figure 11). If the radius of curvature between the two vectors reaches the critical radius for breaking (R_{break}) the flexible fiber snaps. At any time step, with the value of trace B (radius of curvature between the two vectors) plus with the average FL the radius of curvature can be calculated. Since

the mechanical property of the fibers are known the predicted value (R) can be compared with R$_{break}$ and the breakage rate can be obtained (Chen et al., 2015):

$$P = C_B \dot{\gamma} max \left(0, \left[1 - exp \left(1 - \frac{R_{break}}{R} \right) \right] \right)$$

Equation 17: Breakage probability of a flexible fiber, where C$_B$ is a scalar constant, $\dot{\gamma}$ the shear rate, R$_{break}$ the critical radius for breaking (=Young´s modulus/ultimate tensile strength of the fiber*radius of the fiber) and R the predicted critical radius for breaking (Chen et al., 2015).

Baird´s model has one fitting parameter (C$_B$). The model indirectly includes fiber-fiber interactions by incorporating a phenomenological parameter C$_I$, which is derived from the Folgar-Tucker model for fiber orientation predictions (Folgar and Tucker, 1984). Baird's model only tracks average values instead of the full FLD. The model is not implemented in commercial injection molding simulation packages. Additionally, the methodology of the model is not fully explained in detail at this point and, therefore, difficult to implement and use (Chen et al., 2015).
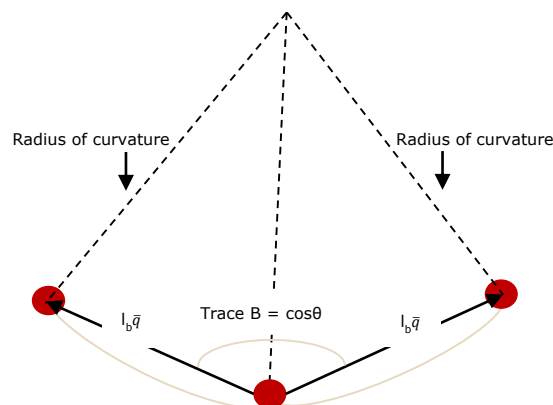
Figure 11: Two-rod model of an elastic fiber. The bending potential depends on the angle between the two unit vector p and q. cosθ (=Trace B) is the radius of curvature of a bent fiber and can be related with fiber breakage. The length l$_b$ is the order of the persistence length of the fiber (Chen et al., 2015).

1.4.3 Single Particle Model

Particle level simulations are a more fundamental approach to study the motion and mechanical response of fibers during processing. In these models, each fiber is modeled separately to simulate the motion of each individual fiber, including

interactions with the mold, the melt and fiber-fiber interactions (Perez et al., 2016b).

At the PEC, University of Wisconsin-Madison, a single particle model was developed (Lopez et al., 2013) which is based on the work presented by Schmid et al., 2000 and Lindström et al., 2007 (Schmid et al., 2000, Lindström and Uesaka, 2007).

In this model each single fiber is represented as a chain of rigid elements with circular cross sections, interconnected with spherical joints (Figure 12). For every time step within a known flow field the torque and force balance is solved for each fiber element. These balances yield a system of linear algebraic equations in which the unknown nodal velocities for each fiber are solved for and integrated over time. Since the fiber deformation is tracked the model can also predict stresses within the fibers and consequently fiber attrition. The model considers contact forces between fibers (=excluded volume forces), fiber-fiber interactions, fiber elasticity and hydrodynamic forces (=stokes forces) (Figure 12) (Baur et al., 2014, Perez et al., 2016b).

The advantage in using these kind of models is their high accuracy that is reached by modeling the actual motion of individual fibers. However, this comes at the price of high computational costs and times (Strautins, 2008).
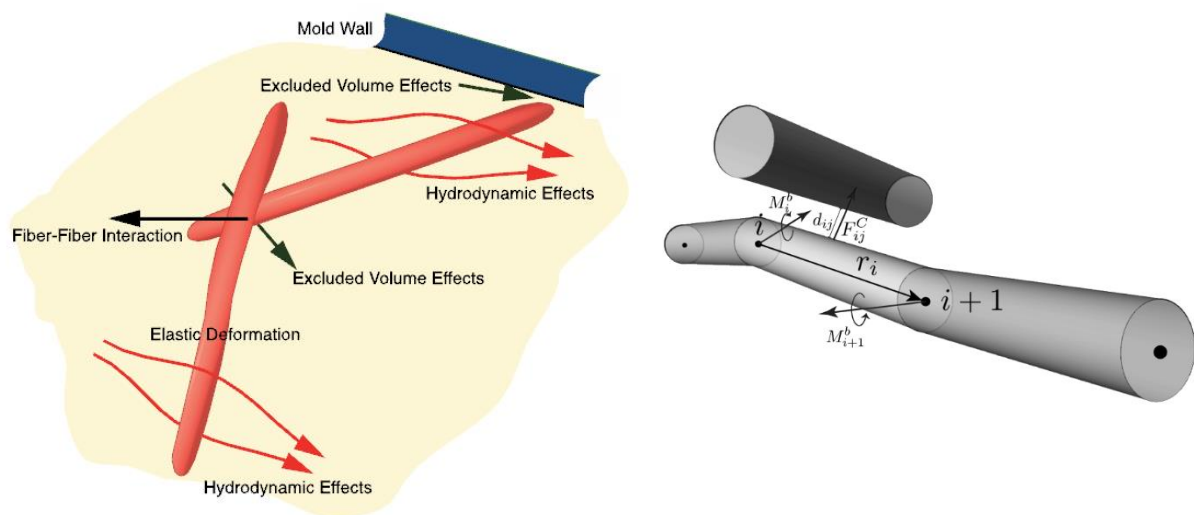
Figure 12: Left: Different effects acting on fibers in moving suspensions which are included in the mechanistic model (Baur et al., 2014), right: Fiber represented as a chain of segments (Perez et al., 2016b).

2 Materials and Methods

2.1 Overview Experimental Setup
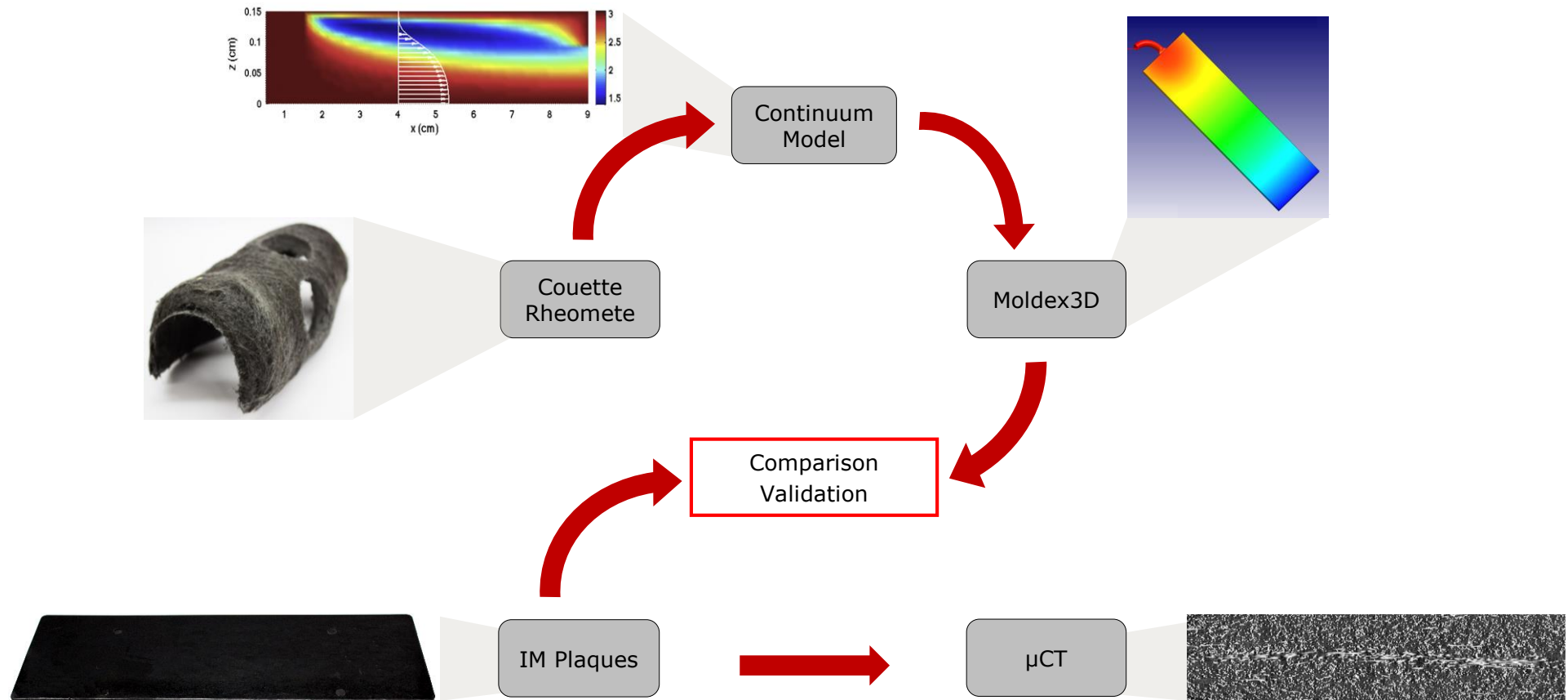
Figure 13: Experimental setup, where the acronym IM means injection molding.

Figure 13 illustrates the overall work-flow of this study. As a first step and the main part of this thesis, long glass fiber-reinforced PP (PPGF) was sheared in a Couette rheometer under different processing conditions. The induced fiber attrition was investigated by analyzing the test specimens with the PEC FL-measurement technique. The obtained results (number- and weight average FL) were then used as input parameters for the Phelps fiber breakage prediction (Phelps model). The model´s three empirical fitting parameters were obtained by fitting the simulation output to the measured values. The optimized model parameters are then used as an input for a Moldex3D simulation to determine the fiber breakage of an injection molded plaque. The predicted end FL was compared to the experimentally determined value which was again obtained by using the PEC FL-measurement technique.

The second part of this work involved the analysis of FD variations in injection molded plaques using µCT. This analysis focuses on studying the correlation of the change in FL caused by fiber breakage and the variation in FD, which occurs in injection molding as a result of the fiber-matrix separation phenomena (Goris, 2016). Each step of the experimental setup is explained in detail in the next chapters.

2.2 Material

The composite material used in this study is a commercially available long glass fiber reinforced PP with varying FCs (fiber reinforcement of 20, 30, 40 and 60 %wt.). The used E-glass fibers (density = 2.55 g/cm^3) are chemically coupled to the PP matrix (density = 0.91 g/cm^3). The material is supplied in form of coated pellets with a nominal length of 15 mm, which also represents the initial and uniform length of the glass fibers. The material was provided by SABIC Innovative Plastics, Geleen, Netherlands. Table 5 summarizes the main material properties.

Table 5: Material properties of the long glass fiber reinforced PP (SABIC® STAMAX).

Material properties	PPGF20	PPGF30	PPGF40	PPGF60
Nominal fiber content [%wt.]	20	30	40	60
Nominal fiber length [mm]	15	15	15	15
Fiber diameter [µm]	19±1	19±1	19±1	19±1
Density composite [g/cm^3]	1.04	1.12	1.22	1.48

2.3   Couette Rheometer Setup

The Couette rheometer used in this study was designed at the PEC, University of Wisconsin Madison (Domenicone-Cerquozzi, 2013). This rheometer is able to process LFT materials and to mimic the process conditions in an injection molding machine under controlled conditions.

The Couette device consists of a 150 mm long inner cylinder of 35 mm diameter which is coaxially aligned in the outer cylinder (Figure 14). The material is sheared in the annular gap (radius = 5 mm) between the rotating inner- and the stationary outer cylinder. The temperature of the system is measured by a SEFE-J-1 thermocouple (OMEGA PL 080916DJB) which slightly protrudes into the annular gap. The thermocouple is connected to a Barber Colman 580 PID-controller. This temperature controller regulates the heating of the heating bands, which are fixed on the outer cylinder. In order to maintain the desired temperature the system was insulated with a refractory Ceramic Fiber Blanket (Kaowool RT Blanket from Morgan Thermal Ceramics).
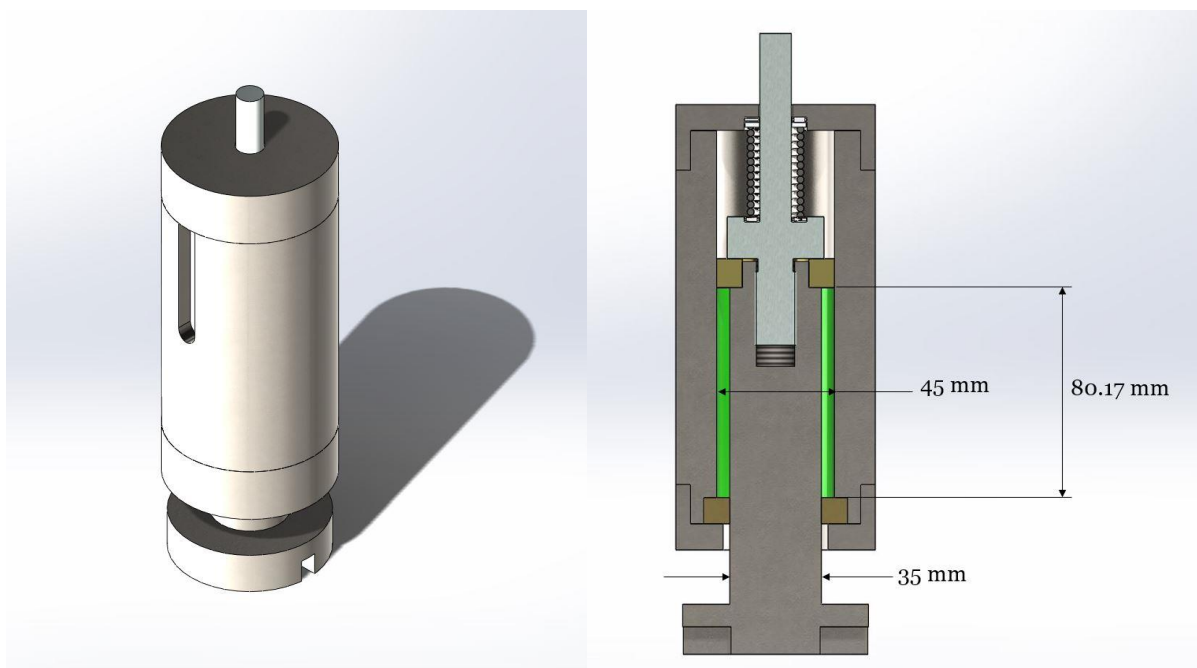
Figure 14: left: Closed Couette rheometer after the material filling process, right: Dimensions of the Couette rheometer (Pratt, 2016)

The Couette rheometer is assembled according to Figure 14, right: The outer cylinder (3) is fixed to the base (2) (Figure 15). The thermocouple is inserted in the opening of the outer cylinder. The big brass ring (8) is placed in the recess

provided in the outer cylinder (3b). Then the outer cap (7) is screwed on to fix the brass ring (8). The inner cylinder (1) is placed in the outer cylinder (3b). The small brass ring (9) is placed in the recess of the inner cylinder and the aluminum cylinder (4) is screwed in. A washer, a bearing (10), a compression spring (Music Compression Wire 720x080x250 from LEE Spring Company) (5) and another set of bearing and washer are put on the aluminum cylinder. The spring is compressed by screwing on the outer cap (6) to close the assembly (3a). The rheometer is then connected to a Brabender equipment (C.W. Brabender Instruments Inc. So. Hackensack N.J.). The individual parts of the Couette rheometer are displayed in Figure 15.
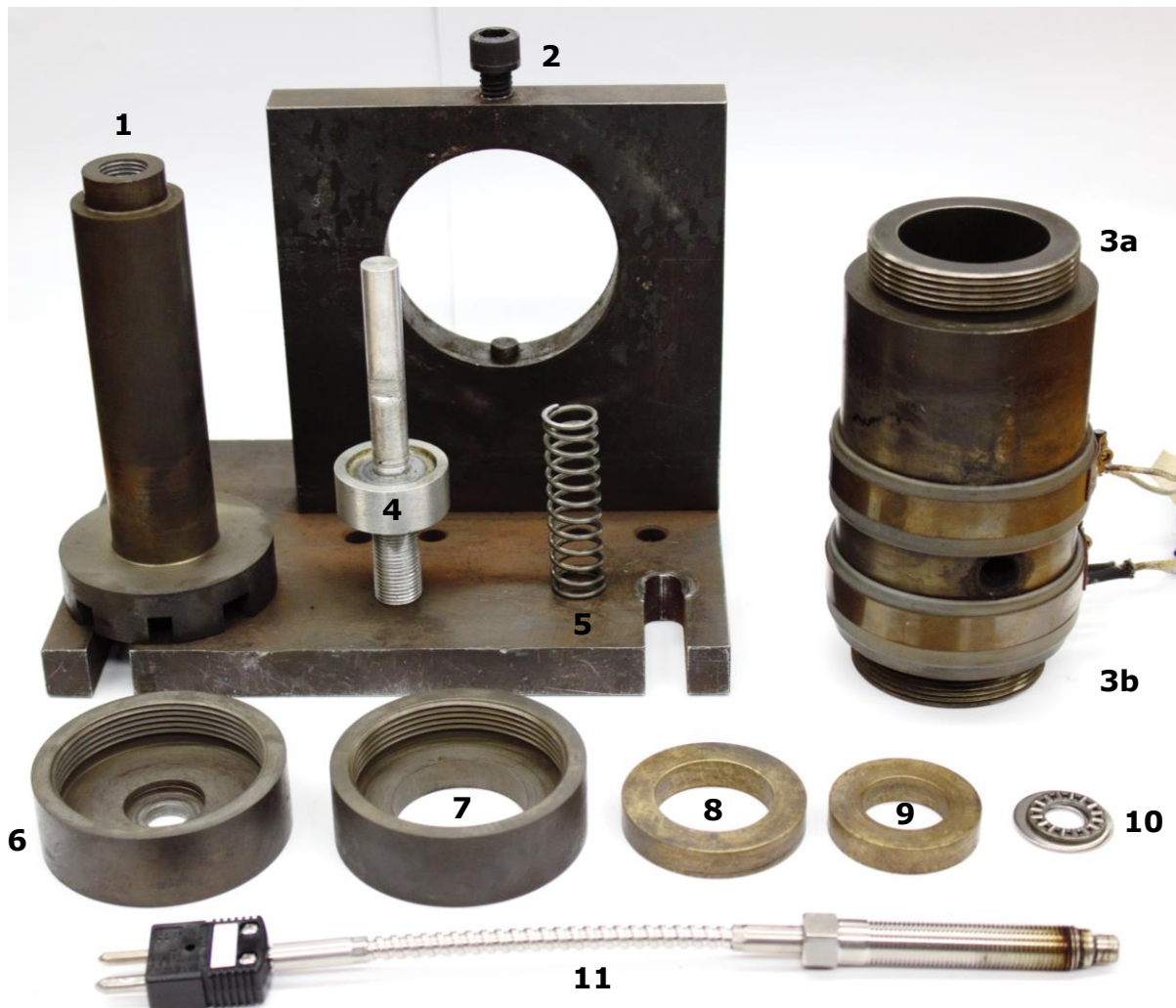
Figure 15: Individual parts of the Couette rheometer, where 1 shows the inner cylinder, 2 the base of the Rheometer, 3 the outer cylinder with two heating bands and the opening for 11, 4 the aluminum cylinder, 5 the compression spring, 6 and 7 the outer caps for 3, 8 and 9 the brass sealing, 10 two sets of bearing and washer and 11 the SEFE-J-1 thermocouple, respectively.

At the start of a Couette experiment the assembly was heated up. When the desired working temperature was reached the material (approx. 60 g) was filled in the annular gap between inner- and outer cylinder. To ensure isothermal conditions an external thermocouple (TJ36-CASS-116U-6 from OMEGA) with a digital multimeter (Extech Minitec™ 26 from Extech Instruments) was used to confirm that the melt temperature is identic to the set processing temperature. The rheometer is connected to a Brabender equipment and the material is sheared. The different processing conditions are shown in Table 6. After the shearing the rheometer is detached from the Brabender and the sample is collected for FL analysis.

Table 6: Design of Experiment approach which encompasses variation of the rotational speed of the inner cylinder, variation of the melting temperature, the residence time and the fiber content of the investigated material. SABIC® STAMAX PPGF20 describes a 20 %wt. long glass fiber-reinforced PP and SABIC® STAMAX PPGF30 is a 30 %wt. long glass fiber-reinforced PP, respectively.

Processing conditions	PPGF20	PPGF30	PPGF40	PPGF60
Rotational speed [rpm]	46, 160	46, 160	46, 160	46, 160
Residence time [sec]	120, 300	30, 45, 60, 90, 120, 300, 600	120, 300	120, 300
Melt temperature [°C]	280	220, 280	280	280

2.4 Fiber Content Measurement Technique

2.4.1 Pyrolysis

The local FD was determined by pyrolysis at a temperature of 500 °C for 2 hours (Couette rheometer samples) and at 500 °C and for 3.5 hours (injection molded plaques). The specimen was weighed before and after the pyrolysis and the fiber volume fraction was determined according to Equation 18.

$$fiber\ volume\ fraction\ [\%] = \frac{fiber\ volume\ [g/cm^3]}{fiber\ volume\ [g/cm^3] + matrix\ volume\ [g/cm^3]} * 100$$

Equation 18: Fiber volume fraction

The fiber- and matrix volume are calculated according to Equation 19 and Equation 20:

$$fiber\ volume\ [\ g/cm^3] = \frac{fiber\ mass\ [g]}{E-glass\ density\ [g/cm^3]}$$

Equation 19: Fiber volume. The density of the E-glass fibers is 2.55 g/cm³.

$$matrix\ volume\ [\ g/cm^3] = \frac{matrix\ mass\ [g]}{PP\ density\ [g/cm^3]}$$

Equation 20: Matrix volume. The density of the PP matrix is 0.91 g/cm³.

2.4.2 Micro Computed Tomography

In order to study the FD variation through the thickness of the injection molded samples, µCT scans were performed. The FD distribution through the part thickness was measured at five different sampling locations along the flow path (distance from gate to the center of the sampling location: 43 mm (=1), 89 mm (=2), 155 mm (=3), 211 mm (=4) and 267 mm (=5)), as shown in Figure 16.
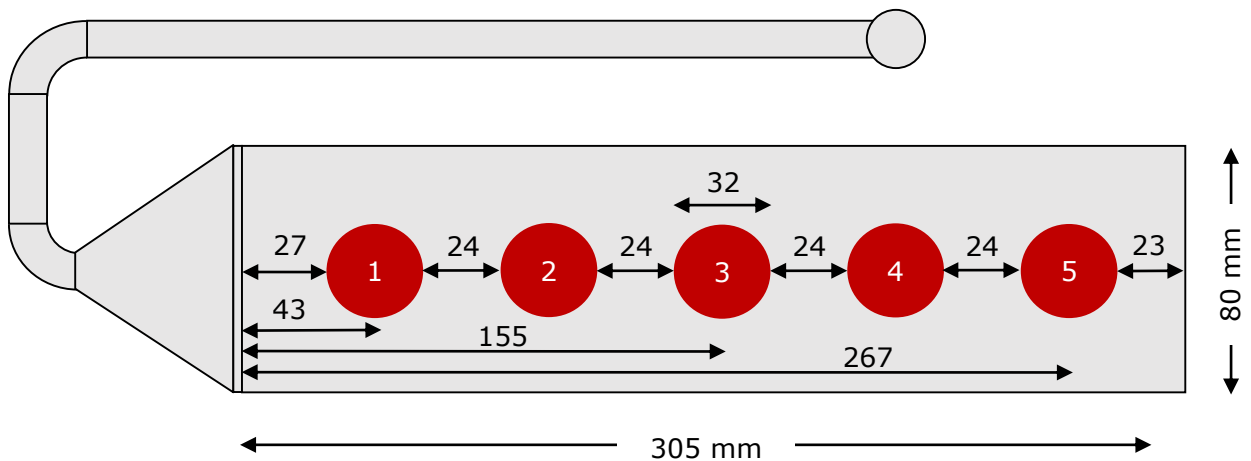
Figure 16: Injection molded plaque with sample positions for µCT scans

The measurements were repeated for two plaques to show the reproducibility of the injection molding process and to ensure the reliability of the results. The µCT data was analyzed using image processing and the approach suggested by Goris et al., 2016. In this approach, the µCT data set is converted into a stack of 2D cross-sectional images aligned normal to the thickness direction. These grayscale

images are transformed into binary images by thresholding, which separates the image into black (matrix) and white (fibers) pixels. Subsequently, the fiber volume fraction through the thickness is determined by processing the binary images and a normalization step to overcome the ambiguity caused by the thresholding step (Goris and Osswald, 2016).

The samples were scanned with a Metrotom 800 µCT system (Carl Zeiss AG, Oberkochen, Germany). The used scan parameters are summarized in Table 7.

Table 7: Metrotom 800 µCT settings.

Parameter	Unit	Value
Voltage	V	110
Current	A	70
Integration Time	ms	1000
Gain	-	8
Voxel Size	µm	8
Number of Projections	-	1800

2.5 Fiber Length Measurement Technique

2.5.1 PEC Fiber Length Measurement Concept

The FL measurement technique developed at the PEC was applied for all samples in this work (Goris and Osswald, 2016). The individual steps of this new concept are shown in Figure 17 and are explained in detail in the following chapters.

Sample extraction   Matrix removal   Downsampling   Dispersion

Scanned image   Thresholding   Fiber detection   Data analysis
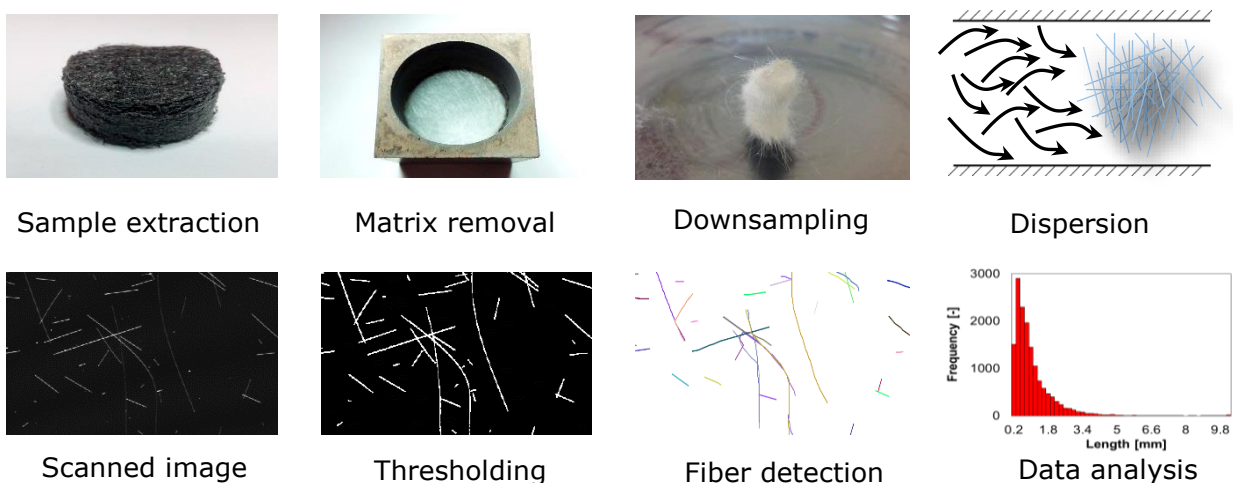
Figure 17: Illustration of the fiber length measurement technique developed at the Polymer Engineering Center (PEC) at the University of Wisconsin-Madison.

2.5.2 Downsampling

Even small samples might contain several million fibers, which makes the characterization of the FLD cumbersome and extremely time-consuming. Thus, the PEC measurement technique applies a downsampling approach based on the method proposed by Kunc et al., 2007 (Kunc et al., 2007a). Three representative coupons (radius = 15 mm) per Couette specimen are cut out with a hole saw drill bit. In order to avoid edge effects from the Couette rheometer all samples are taken 15 mm (initial FL = 15 mm) away from the sample edges. The samples are transferred into specially designed perforated brass sample holders and a weight is put on top (Figure 18). The container and the added weight act like a constraint to help to maintain the original sample size and prevent the fiber network from expanding during the pyrolysis. The polymer matrix is burned off in a Paragon Sentry XPRESS 4.0 lab furnace (Paragon Industries, L.P.) for a period of 2 hours at 500 °C to isolate the fibers from the composite. To obtain a sub-sample (contains at least 20 000 fibers) of the ashed fibers a hypodermic needle (BD Eclipse[TM] Needle from Franklin Lakes 22G x 1 ½) is centrically inserted through a needle guide into the fiber network and a column of BONDIC®Liquid-glue (B0027N07MM) is injected. The glue is cured with a 12UV LED Flashlight (Model TT-Fl001 from Tadronics®). The fiber-glue-plug is extracted from the brass container and fibers not attached to the glue column are gently removed by using brushes. A second burn-off for a period of 1.5 hours at 500 °C is performed to remove the resin (Kunc et al., 2007a, Phelps et al., 2013).
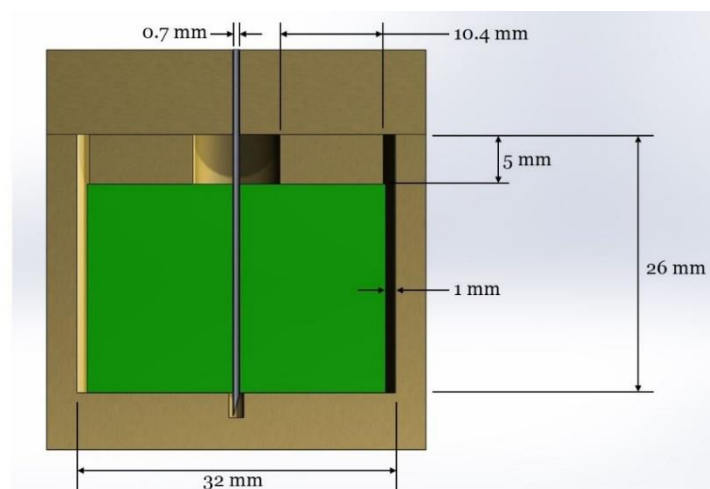
Figure 18: Brass sample holder, where the green space displays the Couette rheometer sample. A weight is put on the sample to prevent the fiber network from expanding. A needle guide is placed on the weight to only extract central fibers (Pratt, 2016).

2.5.3 Fiber Dispersion and Image Processing

The fibers are dispersed through a specially designed air dispersion chamber using bursts of compressed air at 1.5 bar (Figure 19). Due to the turbulences in the enclosed chamber system a disentanglement and a uniform dispersion of the fibers on glass plates with the dimensions of 290 mm x 215 mm x 2.3 mm can be achieved.

An Epson Perfection V750 PRO scanner (Seiko Epson Corporation, Suwa, Japan) was used to generate a 16-bit grayscale digital image of the fibers. In order to capture even the smallest fibers the resolution of the scanner was set to 1200 dpi. The optimized histogram settings for this resolution are summarized in Table 8.

Table 8: Optimum histogram settings to create scans with clearly visible fibers. The white point depends on the scan and ranges between 35-50.

Black point	Gamma	White point
0	0.23	~45

The scanned image is processed in Photoshop, Adobe Systems Inc., San Jose, USA. A binary image is created by using a thresholding technique. The thresholding value (ranges between 15-30) is chosen manually depending on the scan and the reflections on the glass plate. Dust particles, scratches on the glass plate and other noise which lower the quality of the scanned image can be removed manually.
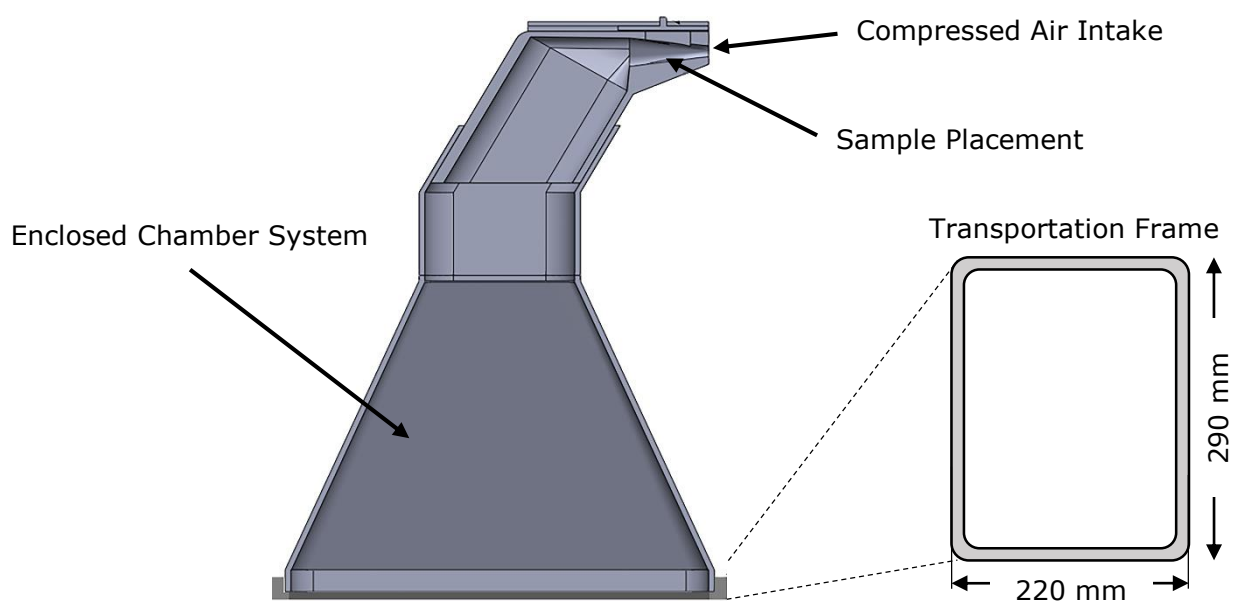
Figure 19: Enclosed chamber system for fiber dispersion with pressurized air (Goris, 2016).

2.5.4 Marching Ball Algorithm

The image processing algorithm used to analyze the scanned image is the Marching Ball Algorithm (Perez et al., 2013). This novel algorithm was developed at the PEC and detects single fibers and quantifies the FLD, as described in section 1.2.4.1.

2.5.5 Kunc Correction

Any downsampling method results in skewing the FLD, e.g. preferentially capture of long fibers since the downsampling area is small compared to the longer fibers in a sample (Figure 20). Thus a correction function is used for all FL values to be able to provide an unbiased FLD (Kunc et al., 2007a).
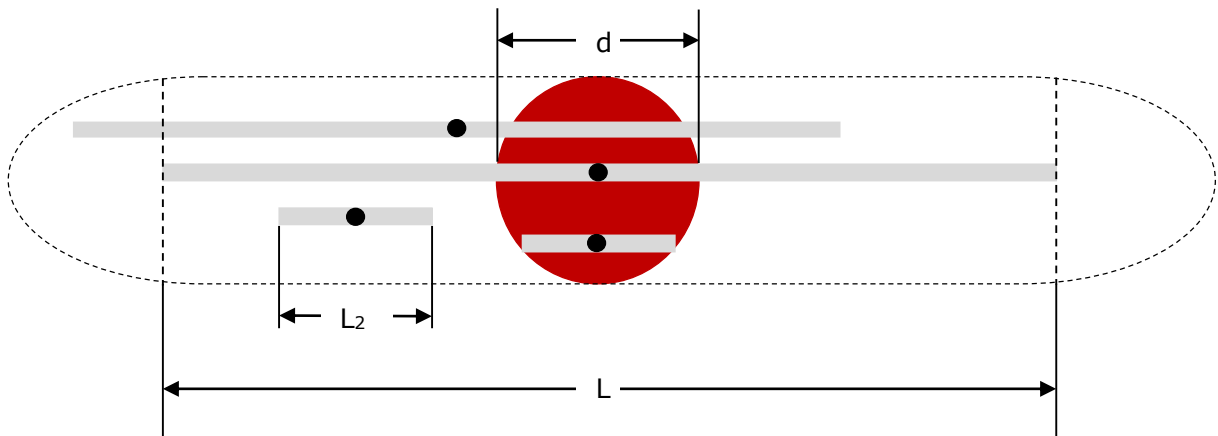
Figure 20: Sampling region of diameter d with three fibers captured for experimental measurement. A preferential capture of long fibers can be seen since the probability of long fibers passing through the region of the resin plug is higher than for a short fiber (Kunc et al., 2007a).

It is assumed that the sampling region (= glue column) is a disk of diameter d and that all fibers lie in the same plane as the disk, so that the actual number of centroids of fibers of length L within the sampling region N(L) can be obtained from the raw measurement of number of fibers of length L that pass through the sampling region Φ(L) as (Kunc et al., 2007a):

$$N(L) = \Phi(L)\left(1 + \frac{4L}{\pi d}\right)^{-1}$$

Equation 21: Corrected number of fibers of a certain length N(L), where Φ(L) is the number of fibers of length L and d the diameter of the glue column, respectively (Kunc et al., 2007a).

2.5.6 Representation of the Results

The output of the analysis is a data set consisting of the individual lengths of all fibers. This raw data set needs to be statistically processed in order to obtain comparable results to study the fiber breakage phenomena.

The most common statistical representation of the measured data is the FLD, the cumulative distribution and characteristic average values (number- and weight-average FL).

The cumulative distribution is described as follows:

$$W(L_i) = P(l \leq L_i) = \sum_{i=0}^{L_i} \frac{N_i}{n}$$

Equation 22: Cumulative FLD W, which gives the probability that fibers of length l are shorter than a certain value L_i. W is calculated by summating the relative frequency of each length interval (quotient of the number of fibers of a certain length N_i divided by the total number of fibers n).

The number-average FL ($\bar{L}_n$) and the weight-average FL ($\bar{L}_w$) are calculated according to Equation 23 and Equation 24:

$$\bar{L}_n = \frac{\sum_i N_i l_i}{\sum_i N_i}$$

Equation 23: Number average FL. The lengths l_i span the range of the data. N_i is the number of fibers with lengths between l_i-Δl/2 and l_i+Δl/2 (Δl is the experimental bin width and a set of length values l_i such that l_{i+1}=l_i+Δl) (Nguyen et al., 2008b, Yilmazer and Cansever, 2002, Ren and Dai, 2014, Wang et al., 2011).

$$\bar{L}_w = \frac{\sum N_i l_i^2}{\sum N_i l_i}$$

Equation 24: Weight average FL. The lengths l_i span the range of the data. N_i is the number of fibers with lengths between l_i-Δl/2 and l_i+Δl/2 (Δl is the experimental bin width and a set of length values l_i such that l_{i+1}=l_i+Δl) (Nguyen et al., 2008b, Yilmazer and Cansever, 2002, Ren and Dai, 2014, Wang et al., 2011).

2.5.7 Validation of the PEC Fiber Length Measurement Method

Three selected Couette rheometer samples were measured using the STAMAXTAT method (see section 1.2.4.1) and the measurements were provided by SABIC. The obtained FL-results were compared to those obtained by using the PEC FL-measurement technique.

2.6   Injection Molding Trials

SABIC® STAMAX PPGF40 was processed externally in a 200-ton Van Dorn Demag injection molding machine according to the official processing guidelines by SABIC® (SABIC, 2016). The used molding parameters are shown in Table 9. The part geometry is a plaque with dimensions of 102 mm x 305 mm x 3.2 mm and a 19.1 mm fan-gate (Figure 16).

Table 9: Injection molding parameters.

Molding parameter	Value
Melt Temperature [°C]	250
Mold Temperature [°C]	55
Injection Pressure [psi]	1100
Holding Pressure [psi]	480
Back Pressure [psi]	75
Injection Time [s]	1
Holding Time [s]	27

The FLD of the injection molded plaque was determined at three sampling locations (distance from gate to the center of the sampling location: 43 mm, 155 mm and 267 mm, Figure 16). The three test specimen show a radius of 15 mm and were cut out with a water jet cutter. The weight- and the number average FL were determined with the PEC FL measurement technique (Figure 17) and the results were compared to those obtained from an injection molding simulation (Moldex3D, Coretech Inc.).

2.7   Evaluation of a Fiber Breakage Model

2.7.1 Phelps Model

2.7.1.1   Introduction

The Phelp's model for fiber breakage prediction was implemented and evaluated for experimental studies. The continuum model uses three empirical model parameters, namely the hydrodynamic drag coefficient (ζ), the breakage coefficient (C_B) and the distribution shape factor (S). According to Phelps et al., (2013) the parameters are supposed to be fitted to experimental data.

Furthermore, it may be assumed that the parameters are material dependent in order to make the model an actual predictive tool. This means that experimentally obtained parameters for one material are supposed to be applicable for the same material under different processing conditions. However, the material dependency of the parameters has not been studied nor validated to date. This particular aspect is assessed in this work, because it is an important aspect of the Phelps model to make it a viable model for fiber breakage predictions (Phelps, 2009).

In order to verify the material dependency of these fitting parameters, Phelp's model was implemented in MATLAB and was used to emulate the PPGF20, PPGF30 and PPGF40 Couette experiments.

2.7.1.2 Input Variables

The model´s input parameters are the initial FL (15 mm), the viscosity (Pas), the shear rate (s^{-1}) and the processing time (sec). Furthermore, the histogram data (assignment of fibers to a certain length class according to their length) for Couette runs with the same processing conditions have to be combined (frequencies have to be summed up) since each experiment was repeated at least three times to ensure the reliability of the results.

The viscosity for each processing condition was modeled by using the Cross-WLF Model. This six parameter model is most common used to model the effects of shear rate and temperature on the viscosity in injection molding simulation software because it offers the best fit to viscosity data (Osswald and Rudolph, 2015).

The viscosity was calculated by using this constitutive equation:

$$\eta(\dot{\gamma}) = \frac{\eta_0}{1 + \left(\frac{\eta_0 \dot{\gamma}}{\tau^*}\right)^{1-n}}$$

Equation 25: Cross Model equation, where η is the viscosity, η_0 is the zero shear rate viscosity, n is the Power Law index which accounts for the shear thinning behavior, $\dot{\gamma}$ is the shear rate, τ^* is the critical shear stress at the transition from the Newtonian plateau (Osswald and Rudolph, 2015).

The critical shear stress and the zero shear rate viscosity are calculated according to Equation 26 and 27:

$$\tau^* = \left(\frac{4n}{3n+1}\right)^{\frac{n}{1-n}}$$

Equation 26: Critical shear stress τ^*, where n is the Power Law index (Osswald and Rudolph, 2015).

$$\eta_0(T) = D_1 * exp\left[\frac{-A_1(T-T_c)}{A_2 + T - T_c}\right]$$

Equation 27: Zero shear rate viscosity η_0, where D_1 is the viscosity at a reference temperature T_c, A_1 and A_2 describe a temperature dependency (Osswald and Rudolph, 2015).

The used model coefficients for PPGF20, PPGF30 and PPGF40 are given in Table 10 and were obtained from the Moldex3D material data bank.

Table 10: Cross WLF model coefficients for glass fiber reinforced Polypropylene at various fiber concentration levels (STAMAX PPGF20, PPGF30, PPGF40).

Description	Denoted	Unit	PPGF20	PPGF30	PPGF40
Power Law index	n	-	0,30	0,33	0,34
Critical shear stress	τ^*	Pa	27990	206700	175000
Viscosity at a reference temp. T_c	D_1	Pas	4,11e+15	1,90e+18	7,06e+18
Reference temp.	T_c	K	263,15	263,15	263,15
Temperature 1	A_1	K	36,42	40,48	41,56
Temperature 2	A_2	K	51,60	51,60	51,60

The shear rate was calculated according to Equation 28:

$$\dot{\gamma} = \frac{v}{h}$$

Equation 28: Shear rate $\dot{\gamma}$ (s^{-1}), where v is the velocity of the moving inner cylinder, measured in m/s and h the radius of the annular gap between the inner- and the outer cylinder, measured in m.

The model´s input parameter (viscosity, shear rate and processing time) for all Couette trials are demonstrated in Table 11.

Table 11: Phelp´s model input parameters. The variables depend on the material properties (STAMAX PPGF at varying fiber concentrations) and on the processing conditions.

Experimental parameters			Flow conditions	
FC	**Proc. speed**	**Temperature**	**Viscosity**	**Shear rate**
[%wt]	**[Rpm]**	**[°C]**	**[Pas]**	**[s⁻¹]**
	46	222	333,8	16,9
	46	280	129,0	
20	160	222	236,6	58,8
	160	280	105,6	
	46	222	452,1	16,9
	46	280	170,9	
30	160	222	290,3	58,8
	160	280	129,6	
	46	222	573,9	16,9
	46	280	227,3	
40	160	222	343,3	58,8
	160	280	161,0	

2.7.1.3 Algorithm and Procedure

For each processing condition at least five sets of empirical parameters are generated by using a genetic algorithm and fitted with a least squares optimization method. The set of optimum fitting parameters was selected that showed the lowest error between the experimental and predicted FLD for each trial. Subsequently, the model parameters are used to simulate the remaining experiments and compared to the measurements. This approach was repeated for all experiments and an error matrix was generated. Rows in the color matrix represent the difference between the fitting parameters, whereas columns demonstrate a change in the processing conditions. More detail on the procedure is given in the next paragraph.

The model parameters are found in the area between p_{Min} and p_{Max}. p_{Min} and p_{Max} describe the lower and the upper limit value of the model parameters and are summarized in Table 12. The values of p_{Min} and p_{Max} are based on the numerical values presented by Phelps et al., 2013 and Phelps, 2009 (Phelps et al., 2013, Phelps, 2009).

Table 12: p_{Min} and p_{Max} for the three empirical model parameters, C_B, ζ and S, respectively.

Description	p_{Min}			p_{Max}		
Material	C_B	ζ	S	C_B	ζ	S
PPGF20	0.0001	0.0006	0.1	0.025	5	2
PPGF30	0.0015	0.0006	0.1	0.025	5	2
PPGF40	0.0001	0.0006	0.1	0.025	5	2

The genetic algorithm creates an initial, random population with a population size of 50 organisms (=50 sets of empirical model parameters). The fitness of the found parameters is evaluated (match between experimental- and predicted FLD). The parameters are then ordered according to their lowest error (from the most to the least fit). Three more fit individuals are taken and each individual's genome is modified by mutating 0.02 % of their genes. A new generation which again consists of 50 organisms is formed. The parameters are ordered according to their lowest error and the three "most fit" members of this second generation are then used in the next iteration of the algorithm. This procedure is repeated till 100 iterations are reached or if the margin error willing to accept is attained (=0.001 %). If this accepted margin error is not reached after 100 iterations the best found set of model parameters is presented. Furthermore, if the match between the experimental- and predicted FLD does not decrease significantly within four generations in a row the algorithm terminates and presents the best found set of parameters. The obtained model parameters are then used to predict the FLD of the remaining experimental conditions and compared to the measurements.

2.7.2 Moldex3D

The injection molding process for end-gated plaques was simulated using Moldex3D. The software has the Phelps model implemented to predict the number and the weight average FL for each element of the mesh. The three model parameters were derived from the corresponding Couette rheometer experiments with the same material (PPGF40). The initial FL for the simulation was set to 4.75 mm, which was obtained experimentally from the purged material.

First, the solid model of the cavity was meshed with 1.5 million elements, which resulted into 12 elements through the thickness. The mold filling simulation was then performed at the given process conditions (Table 9). At three sampling

locations (distance from gate: 43 mm, 155 mm and 267 mm, Figure 16) the predicted FL values were compared to those obtained from the experimental measurements.

2.7.3 Single Particle Model

A defined set of Couette rheometer experiments was emulated with a single particle simulation model.

The length reduction over time obtained from selected Couette rheometer experiments was compared with the predicted values from the mechanistic model simulation. The parameters used for the single particle approach and processing conditions are summarized in Table 13.

Table 13: Comparison of the parameters used for the single particle model and the present conditions in the Couette rheometer run.

Description	Unit	Single Particle Model	Couette Rheometer
FC	%wt.	30	30
Initial FL	mm	12.5	15.0
Fiber diameter	µm	19	19±1
L/D	-	657	790
Fiber Young´s Modulus	GPa	73	-
Fiber strength	MPa	2600	2600
Segments per fiber	-	50	1
Time step	s	1e-5	-
Excluded volume constant	-	500	-
Shear rate	s-1	64.14	58.77
Viscosity	Pas	68.12	129.6
Time	sec	71.30	up to 600
Curvature	mm	0.267	-

3 Results

3.1 Couette Rheometer Results

3.1.1 Design of Experiments

Table 14 summarizes the experimental results of the Couette rheometer experiments. Most notable is the absence of the PPGF60 trials. The obtained test specimens at 60 %wt. did not show any dispersion of the fibers after processing. The initial fiber bundles in the pellets were still intact as can be seen in a downsampled fiber-glue plug in Figure 21 (right). Furthermore, all fibers appeared to have the same orientation which indicates the absent of a shear flow and suggest the occurrence of "slipping". Due to the high fiber loading the polymer-fiber compound was acting like a Bingham fluid in the Couette rheometer. A Bingham fluid requires a certain yield stress to overcome its 'solid structure' to be able to start flowing. Due to the slipping, no shear flow occurred and the shear stress threshold was not exceeded and the melt acted like a solid.

Furthermore, the obtained average FLs from the PPGF60 test specimens yielded to notably larger values (almost no fiber breakage was detected) than those obtained from the PPGF40 trials. These results contradict the physical institution, all published results and theories, which coherently show that a higher FC leads to more fiber-fiber interaction and, consequently to increased fiber breakage. This finding further support our hypothesis that at 60 %wt. the polymer-fiber melt act as a Bingham fluid and therefore the thick fiber bundles neither disperse nor break. While longer FLs are typically sought after, the refusal of the fibers to separate from themselves creates composites with non-uniform FLDs and therefore with non-uniform mechanical properties.
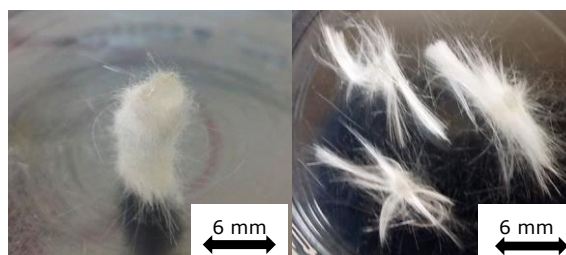
Figure 21: Left: Homogeneous dispersed fibers in a fiber-glue-plug (PPGF40). Right: Oriented, not dispersed fiber bundles in a fiber-glue plug which still show the initial FL of 15 mm for PPGF60.

Table 14: Number- and weight average FLs ($\bar{L}_N$, $\bar{L}_W$) with standard deviation (SD) from the conducted Couette rheometer trials.

Processing parameters				Final results			
Fiber concentration [%wt.]	Melt temperature [°C]	Processing Speed [rpm]	Residence Time [sec]	$\bar{L}_N$ [mm]	SD $\bar{L}_N$ [mm]	$\bar{L}_W$ [mm]	SD $\bar{L}_W$ [mm]
20	280	46	120	2.65	0.24	7.07	0.62
			300	1.79	0.15	5.26	0.45
		160	120	1.36	0.15	3.89	0.55
			300	1.41	0.18	4.00	0.61
30	220	46	120	1.36	0.09	4.22	0.44
			300	0.87	0.08	2.13	0.42
		160	30	1.25	0.11	3.78	0.31
			45	0.90	0.04	2.49	0.18
			60	0.73	0.04	1.84	0.15
			90	0.65	0.02	1.33	0.11
			120	0.64	0.08	1.23	0.28
			300	0.70	0.02	1.45	0.05
			600	0.69	0.09	1.38	0.32
	280	46	120	1.86	0.12	5.42	0.29
			300	1.06	0.11	3.03	0.45
		160	120	0.91	0.11	2.32	0.42
			300	0.89	0.11	2.15	0.53
			600	0.76	0.10	1.60	0.45
40	280	46	120	1.23	0.10	3.80	0.27
			300	0.73	0.05	1.64	0.19
		160	120	0.73	0.17	1.75	0.97
			300	0.64	0.02	1.28	0.05

3.1.2 Length Reduction over Time

In Figure 22 the FL length reduction over time for PPGF30 is shown. Previous studies have already indicated that fiber attrition is a function of time with an exponential type of length reduction (Shon et al., 2005, Moritzer and Heiderich, 2016). It can be seen that the material experiences significant fiber shortening before reaching a steady state value. This steady state value is also called equilibrium value (L_∞) and describes the average FL, which cannot be further broken (unbreakable length) (Phelps et al., 2013). L_∞ can be assumed to be a function of the present rate of deformation, the FC, the suspension viscosity and fiber properties.
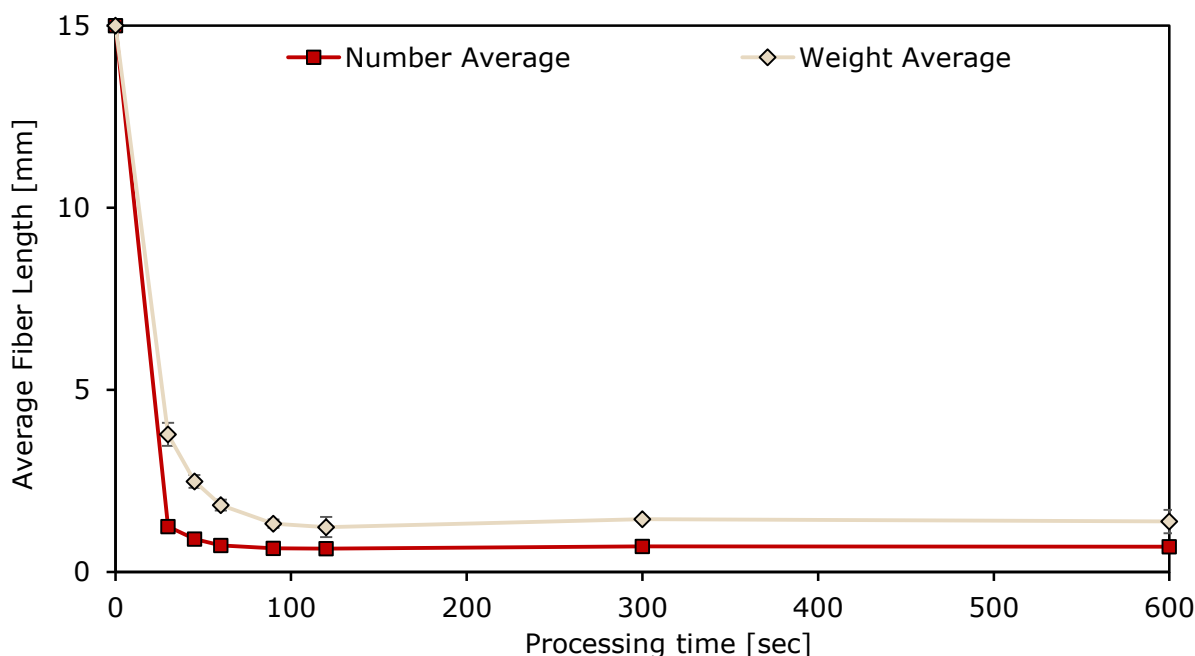
Figure 22: Fiber length degradation over time for PPGF30 at 220 °C and 160 rpm.

According to Table 14 and Figure 22, L_∞ is reached after approximately 60 sec of processing. L_∞ is found to be 0.68±0.05 mm for L_N and 1.45±0.18 mm for L_W. L_∞ is particularly important since it is an input parameter for several predictive models.

The present experimental investigations showed a total reduction from the initial FL (=15 mm) of 95 % for L_N and 90 % for L_W.

The obtained decay function shows that most of the fiber breakage happens at the beginning of the shearing process. However, it is important to keep in mind that

the material used in this study are coated LFT pellets, where the fibers are packed as not fully impregnated bundles. Consequently, there is a certain time period necessary to achieve sufficient dispersion and homogenization, which has an effect on the fiber breakage rate. This dispersion effect is not studied further in this work and measurements were only performed at sufficiently long residence times, e.g. larger than 30 sec at 220 °C and 160 rpm.

3.1.3 Impact of Fiber Concentration

Figure 23, Figure 24 and Figure 25 show the influence of FC on the fiber breakage at varying processing conditions. It can be seen that for all scenarios a higher FC leads to more fiber attrition. This phenomenon can be explained as follows: A higher nominal fiber content increases the degree of fiber-fiber interactions since the distance between the fibers is decreased and this promotes fiber breakage. Furthermore, concentrated regimes show larger suspension viscosities, which impose more stresses on the fibers. Both mechanism cause elevated fiber attrition at higher FCs.
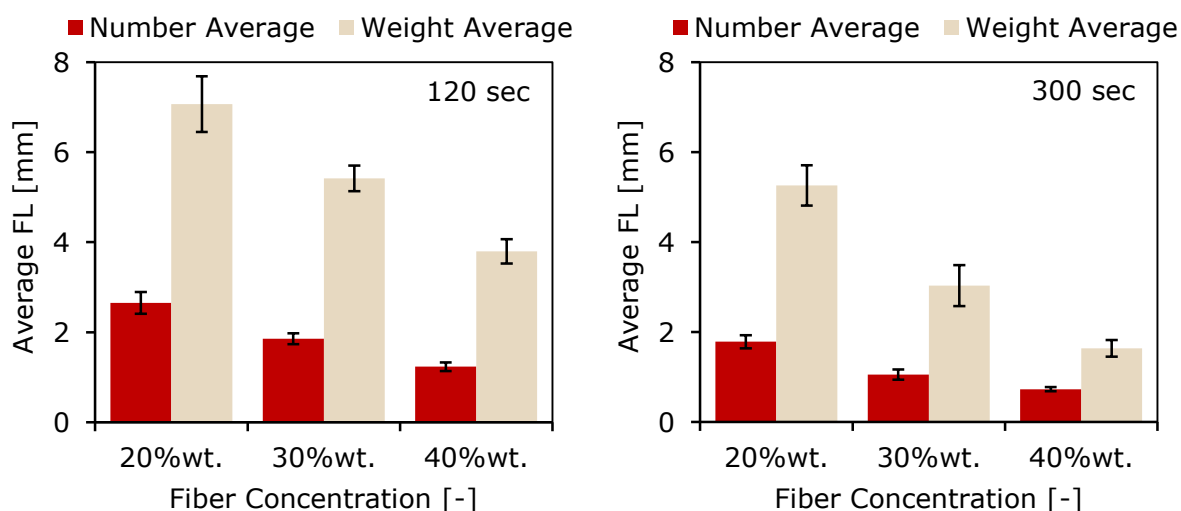
Figure 23: Results on the impact of various fiber concentrations (PPGF20, PPGF30, PPGF40) on the fiber breakage for 280 °C, 46 rpm and residence times of 120- and 300 sec.

This inverse relationship between FC and L_N/L_W agrees with the results published by Moritzer et al., 2016, Ramani et al., 1995, Hassan et al., 2004, Thomason, 2002 and Thomason, 2006 who all postulated that an increased FC leads to accelerated

fiber attrition (Moritzer and Heiderich, 2016, Ramani et al., 1995, Hassan et al., 2004, Thomason, 2002, Thomason, 2006). Moritzer et al., 2016 demonstrated that a higher fiber content causes accelerated FL degradation in a constant shear field (Couette rheometer) for short fiber-reinforced PP (Moritzer and Heiderich, 2016). Ramani et al., 1995 found that an increase in FC from 30- up to 40 %wt. leads to enhanced fiber-fiber interactions and therefore to greater fiber damage (short PSGF) (Ramani et al., 1995). Hassan et al., 2004 and Thomason, 2002 showed for short as well as for long glass reinforced thermoplastics that a higher volume fraction of fibers leads to greater fiber breakage due to increased fiber collisions and overlaps (PPGF and PAGF). They further observed that for a constant volume fraction, shorter fibers are more susceptible to damage (Hassan et al., 2004, Thomason, 2002). Thomason, 2006 added that below 10 %wt. fiber content the final average FL appears to be independent of the FC (short PA66GF). Moreover, results suggest that between 10-40 %wt. an approximate linear decrease of length averages is visible with increasing fiber content (Thomason, 2006). Von Turkovich et al., 1983 assumed that an increase in the fiber volume fraction effects the final FL in the processed material since an enhanced FC should increase fiber interactions causing abrasion or sufficient overly in bending to cause fiber fracture. However, his studies on short PSGF only revealed a slight change in the average FL with increasing volume fraction. This result would indicate that FC does not have a dominant effect on fiber breakage. This finding does not correlate with the work published by Moritzer et al., 2016, Ramani et al., 1995, Hassan et al., 2004 and Thomason, 2002 and Thomason, 2006. An explanation for this deviation would be that the sample preparation- and FL measurement technique used by Von Turkovich et al., 1983 consists of a lot of different steps (Soxhlet extraction, drying of fibers, fiber dispersion in a silicon solution, dispersion on microscopic slides, a second drying step, FL measurement), which might not be sensitive enough and may promote the loss of fibers. Furthermore, the results lack on repetitions and therefore their reliability is doubted (Turkovich and Erwin, 1983a).

In all four cases, L_N and L_W of high speed trials (160 rpm) are consistently smaller than their respective low speed counterparts (46 rpm). This is due to the reason that higher processing speeds impose increased shear stresses on the fibers (higher hydrodynamic forces) and therefore accelerate their breakage. Furthermore, Couette rheometer experiments conducted at high residence times (300 sec) show consistently lower end L_N and L_W values than their low residence

time (120sec) equivalent. A longer residence time increases the time fibers are exposed to fiber breakage mechanisms and therefore might experience greater deformation which promotes fiber attrition. Additionally, it can be seen that the end values for PPGF20, PPGF30 and PPGF40 samples (processed at 160 rpm) approach the equilibrium value for L_N and for L_W. L_∞ is approximately 1.39±0.16 mm for L_N and 3.94±0.58 mm for L_W for PPGF20, 0.85±0.10 mm for L_N and 2.02±0.47 for PPGF30 (section 3.1.2) and approximately 0.69±0.09 mm for L_N and 1.52±0.51 mm for L_W for PPGF40. Since L_∞ is a function of fiber fraction, temperature, processing speed it was expected that an increased FC leads to lower L_∞ values. Furthermore, Moritzer et al., 2016 found that an increased FC accelerates FL degradation (L_∞ is reached faster) and leads to a smaller L_∞. This phenomenon can be explained by the increased fiber-fiber interactions, which are further encouraged by the decreased distance between the fibers in more densely filled materials (Moritzer and Heiderich, 2016). With the obtained data it was able to validate this finding: the lower the FC, the higher the L_∞ values. L_∞ might have also been reached for PPGF40 processed at 46 rpm and 300 sec, but additional experiments need to be conducted at an increased residence time to fully verify this statement.
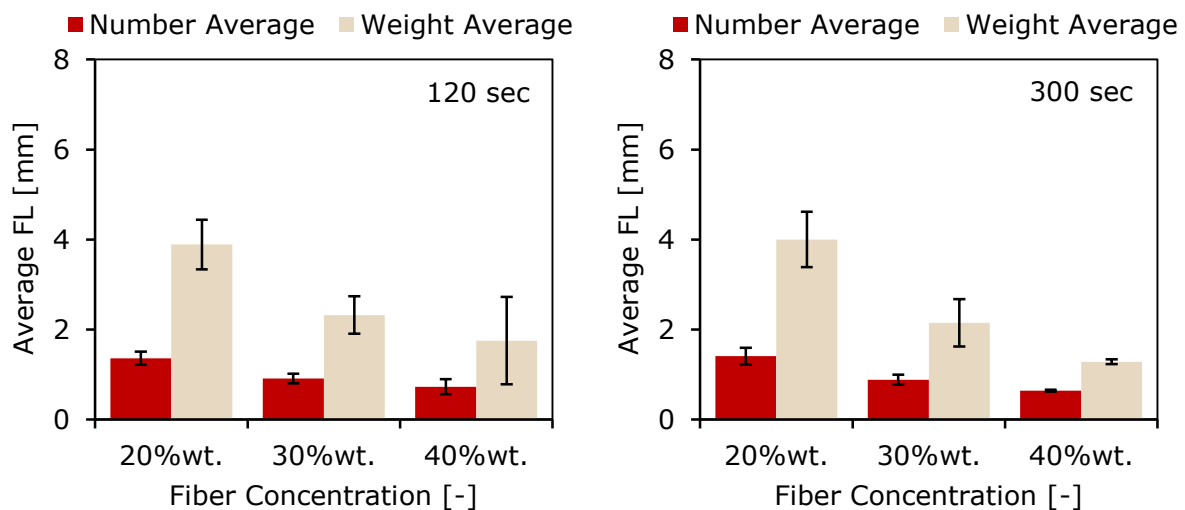
Figure 24: Results on the impact of various fiber concentrations (PPGF20, PPGF30, PPGF40) on the fiber breakage for 280 °C, 160 rpm and residence times of 120 sec and 300 sec.

The obtained data suggest that the residual FL (L_N and L_W) reduces linearly with increasing FC. A similar linear dependency was also found by Thomason, 2004, for

long glass fiber-reinforced PP and Moritzer et al., 2016, for short glass fiber-reinforced PP (Thomason, 2005, Moritzer and Heiderich, 2016).

From Table 14 it can be deduced that an increase in the FC by 10 %wt. equals an additional reduction in L_N and L_W by approximately 35 % for both residence times and low processing speed. For the Couette rheometer trials conducted at 160 rpm a 10 %wt. increase in the FC leads to a reduction in L_N of about 30 % and in L_W of approximately 35 %.

Furthermore, it can be seen that Couette rheometer experiments conducted at low residence times (120 sec) showed a slower reduction in FL if FC is increased by 10 %wt., approximately 30 % for L_N and 25 % for L_W, whereas samples which are sheared for a longer period of time (300 sec) showed an accelerated FL reduction of about 35 % for L_N and 45 % for L_W.
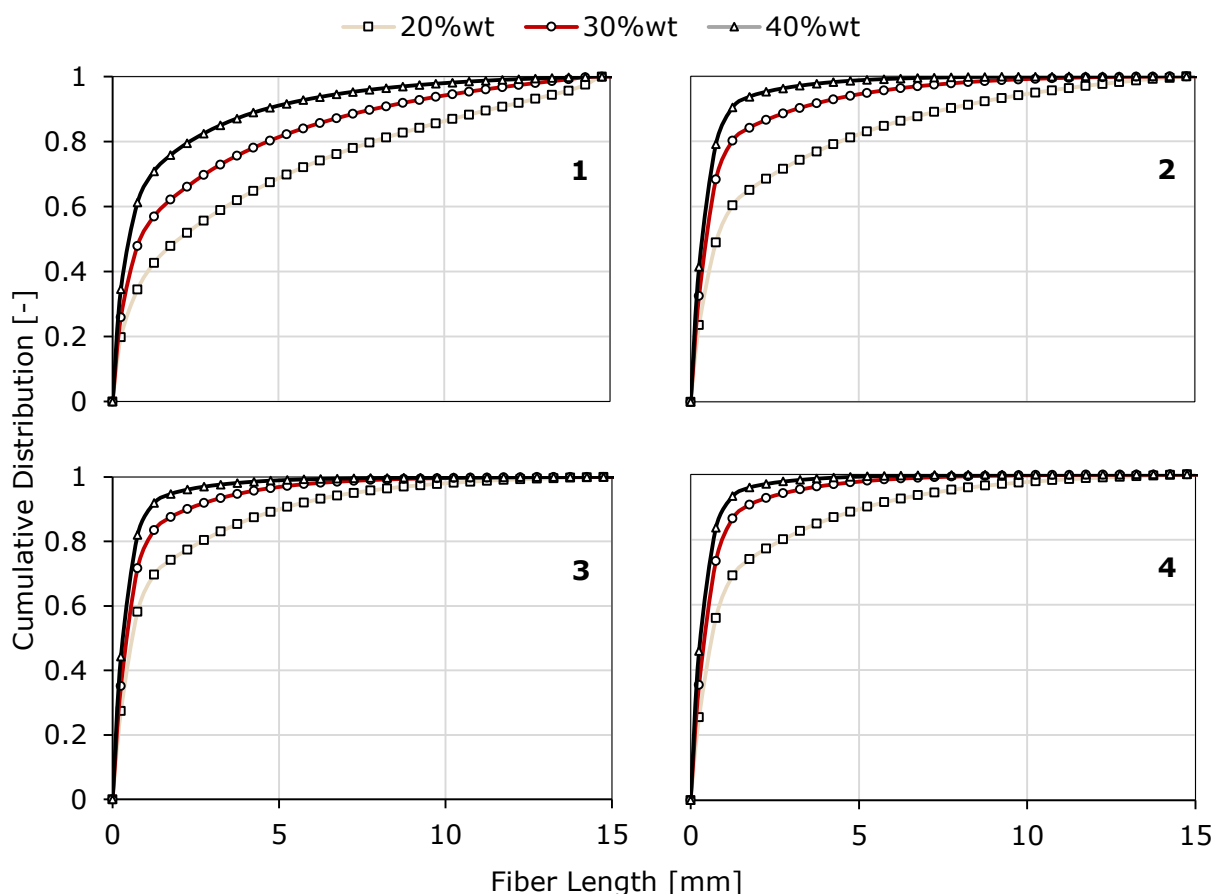
Figure 25: Cumulative FLD at varying fiber contents (PPGF20, PPGF30, PPGF40). 1 and 2 represent the results of samples processed at 46 rpm, 3 and 4 were processed at 160 rpm. The residence times for 1 and 3 was 120 sec, for 2 and 4 300 sec, respectively.

The normalized cumulative length distribution for PPGF at varying fiber content is shown in Figure 25. It can be seen that for all scenarios the higher the FC the more

the cumulative distribution is shifted to the left. The further the distribution is shifted to the left, the shorter the average FL. Low residence time and low processing speed result in a shift to the right, which means more of the initial FL can be preserved. It can be noticed that 4 shows a lower fiber breakage for PPGF20 than 3.

3.1.4 Impact of Processing Speed

Figure 26 and Figure 27 demonstrate the influence of the rate of deformation on fiber attrition by varying the rotational speed of the Couette rheometer. It can be seen that for all four scenarios an increase in processing speed accelerates fiber breakage. This relationship can be explained as follows: An increased processing speed leads to larger total stresses that fibers are exposed to and therefore promotes their breakage. Furthermore, the higher the total deformation the more fiber-fiber interactions occur which also accelerates fiber degradation.
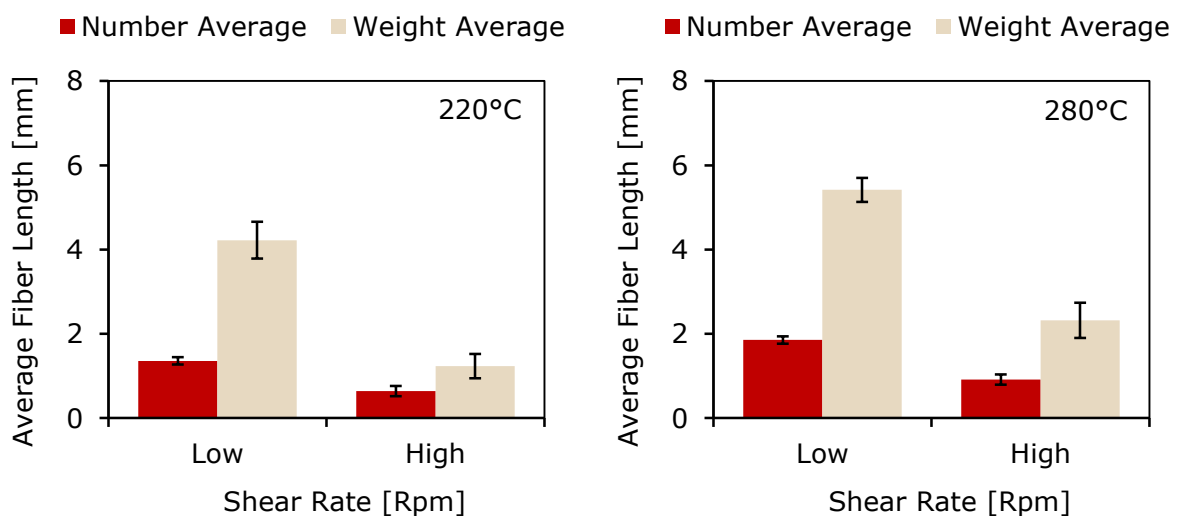
Figure 26: Results on the impact of the rotational speed on the fiber breakage of PPGF30 for left: 220 °C and 120 sec and right: 280°C and 120 sec.

Shear stress acting on the polymer-fiber suspension not only causes chain scission in the polymer molecules, but also reduces the length of the fibers (Yilmazer and Cansever, 2002). As the rotational speed increases, the shear rate increases as shown in Equation 4: 46 rpm equals 16.9 s^{-1} and 160 rpm equals 58.8 s^{-1}. An opposing mechanism is the shear thinning behavior of plastics, which is a reduction

in viscosity at high rates of deformation due to molecule disentanglement which ultimately reduces the stresses acting on fibers (Zhang and Thompson, 2005, Turkovich and Erwin, 1983b, Shimizu et al., 1997). This is due to the fact that at high shear rates the polymer molecules are stretched out and entangled which allow them to slide past each other more easily, thus lowering the melt viscosity (Osswald, 2011). However, the shear thinning impact can be neglected for the present experimental study due to the small range of shear rates (16.9 s^{-1} and 58.8 s^{-1}). Within that range, shear thinning does not have a significant impact on the viscosity. It is further important to note that fibers impede the movement of the polymer molecules. This means that the polymer cannot sufficiently lubricate the fibers, therefore the friction between them is increased, promoting their breakage (Osswald et al., 2006, Lee, 1992, Osswald, 2011, ElBarche et al., 2010).
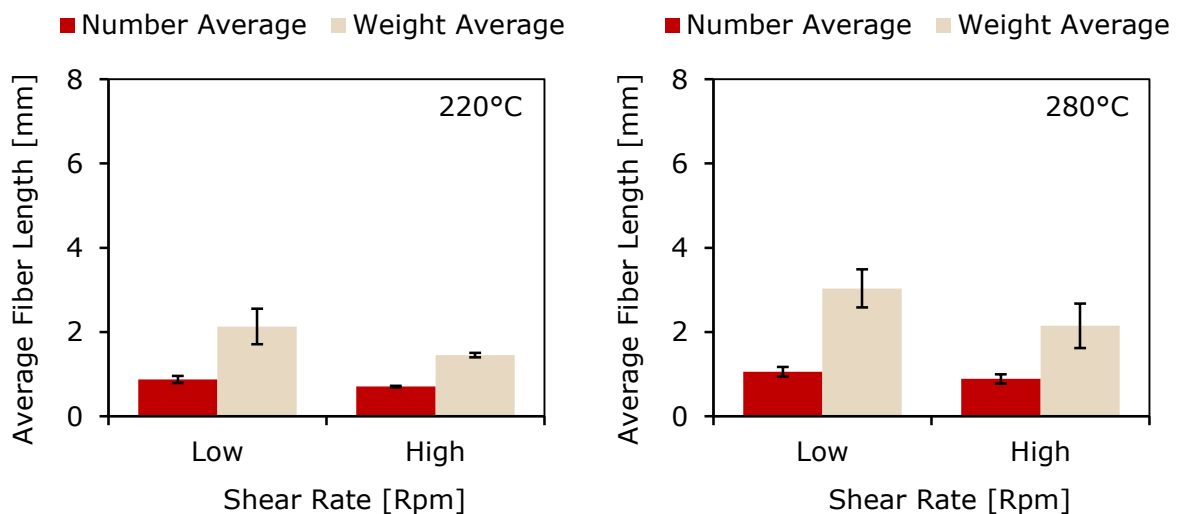
Figure 27: Results on the impact of the rotational speed on the fiber breakage of PPGF30 for left: 220 °C and 300 sec and right: 280°C and 300 sec.

The outcome of this part of the experimental study is consistent with the work published in literature, where most published results indicate that an increased rate of deformation leads to accelerated fiber degradation (Yilmazer and Cansever, 2002, Stade, 1977, Wall, 1989, Ren and Dai, 2014, Zhuang et al., 2008, Moshe et al., 2012). Wall et al., 1989 found that increased processing speeds and rate of deformations promote fiber degradation (Wall, 1989). Yilmazer´s et al., 2002, findings agree with the results presented by Wall et al., 1989. His results further suggest that increased screw velocities promote fiber degradation in short glass fiber-reinforced Nylon 6 in extrusion- as well as in injection molding processes.

Yilmazer et al., 2002 found that raising the rotational speed in extrusion by 50 rpm (from 250, to 300 and 350 rpm) leads to relative reduction in L_W of about 5 % (Feed rate of 70 kg/h). In an injection molding process a raise in processing speed of 50 rpm leads to a relative reduction in L_W of about 4 % (Feed rate of 70 kg/h) (Yilmazer and Cansever, 2002). However, it is important to note that the presented results do not show a uniform behavior, which means an increase in processing speed not always results in an accelerated fiber degradation. Therefore, the reliability of the results is limited. A similar pattern could be observed in Turkovich´s et al., 1983 and Filbert´s, 1969 findings, which not necessarily show a decrease in average FL if shear rate is increased (Turkovich and Erwin, 1983a, Filbert, 1969).

More current studies prove that an increased rate of deformation promotes fiber breakage: Zhuang et al., 2008 made extrusion experiments with short PPGF and found that doubling the processing speed (from 40.5 rpm to 81 rpm) leads to a reduction in the end FL of about 8 % in L_W (Zhuang et al., 2008). Moshe et al., 2012 showed in extrusion experiments that an increase from 34- up to 67 rpm leads to a relative reduction in L_W of about 11 % for short glass fiber-reinforced Nylon 66 (Moshe et al., 2012). Ren et al., 2014 investigated the influence of different screw speeds on the fiber breakage of long glass fiber-reinforced PP. The results suggest that doubling the processing speed (from 40 rpm to 80 rpm) leads to a relative reduction in L_W of approximately 27 % (Ren and Dai, 2014).

It can be seen in Figure 26 and Figure 27 that for all scenarios, L_N and L_W values of high rotational speed trials (160 rpm) are consistently smaller than their respective low processing speed (46 rpm) counterpart. Furthermore, experiments conducted at high residence times (300 sec) show lower L_N and L_W values than their low residence time (120 sec) equivalent, which is attributed to the increased time and, thus, total deformation that the fibers are exposed to. Moreover, it can be noticed that the end values for PPGF30 samples processed at low- and high temperature (220- and 280 °C), high processing speed (160 rpm) and varying residence times all approach L_∞. It can be therefore deduced that in this case the processing speed has a bigger impact on the fiber breakage than the residence time. The value for L_∞ for the low temperature trial is 0.68±0.06 mm for L_N and 1.35±0.22 mm for L_W and for the high temperature trial 0.85±0.10 mm for L_N and 2.02±0.47 mm for L_W. An increased equilibrium value can be noticed for the high temperature trial as L_∞ is a function of temperature.

Table 15 shows the relative decrease in L_N and L_W for PPGF30 at varying process conditions. It can be seen that raising the rotational speed from 46 rpm to 160 rpm leads to a relative decrease in L_W of 70 % at 220 °C and of 60 % at 280 °C for the low residence time trial (120 sec). The high residence time trial (300 sec) shows an identic relative decrease in L_W of 30 % for the high- as well as for the low temperature trial. A similar behavior can be observed for L_N: The same relative decrease in L_N is noticed for low- and high temperature experiments conducted at the same residence time. This identic relative decrease for low- and high temperature trials conducted at the same residence time indicates that the processing speed has a bigger impact than the melt temperature.

Table 15: Relative decrease in the number- and weight average fiber length for PPGF30 at varying processing conditions if the processing speed is raised from 46 rpm to 160 rpm.

Residence time [sec]	Melting temperature [°C]	Relative decrease in L_N [%]	Relative decrease in L_W [%]
120	220	50	70
	280	50	60
300	220	20	30
	280	20	30

3.1.5 Impact of Melt Temperature

Figure 28, Figure 29 and Figure 30 show the influence of melt temperature on the fiber breakage at varying processing conditions. It can be seen that an increased temperature reduces fiber attrition due to the reduction of the suspension viscosity and, therefore, reduces stresses acting on the fibers. The outcome of these trials are consistent with the work published by Turkovich et al., 1983, Shimizu et al., 1997, De Cicco, 2001, Zhang et al., 2005 and Moritzer et al., 2016 who all found that an increased melt temperature reduces fiber degradation (Turkovich and Erwin, 1983a, Shimizu et al., 1997, DeCicco, 2001, Zhang and Thompson, 2005, Moritzer and Heiderich, 2016). The viscosity of PPGF30 for varying process conditions is shown in Table 16.

It can be seen that for all scenarios, L_N and L_W values of high temperature trials (280 °C) are consistently higher than their respective low temperature (220 °C) counterpart. Furthermore, experiments conducted at low processing speed (46 rpm) show higher L_N and L_W values than their high processing speed (160 rpm)

equivalent, since increased processing speed impose greater stresses on the fibers and promote fiber breakage. Additionally, it can be noticed that a raise in residence time, leads to lower L_N and L_W values, which is attributed to the increased time fibers are exposed to possible breakage mechanisms. However, it is important to note that L_N and L_W do not continuously decrease with time. Fiber shortening effects only occur till a steady state value (L_∞) is reached (section 3.1.2).

Table 16: Viscosity for SABIC® STAMAX long glass fiber-reinforced PP (PPGF30) for different process conditions. The viscosity was modeled by using the CROSS-WLF Model (Modified Power Law Model, section 2.7.1.2).

Material description	Processing speed [Rpm]	Temperature [°C]	Viscosity [Pas]
PPGF30	46	222	452.1
	46	280	170.9
	160	222	290.3
	160	280	129.6
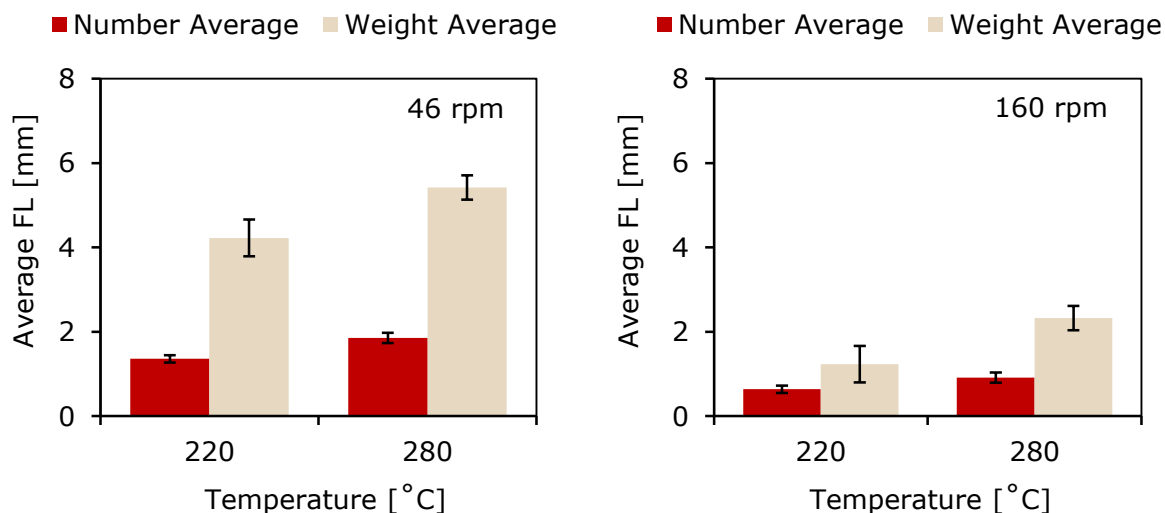
Figure 28: Results on the impact of melting temperature on the fiber breakage of PPGF30 for left: 46 rpm and 120 sec and right: 160 rpm and 120 sec.

This steady state is reached for Couette samples processed at low temperature (220 °C), high processing speed (160 rpm) and varying residence time. It can be seen in Table 14 that L_∞ is definitely reached after 120 sec of processing and displays a value of about 0.68±0.06 mm for L_N and 1.35±0.22 mm for L_W.

Table 14 further demonstrate that L_∞ is already reached after 60 sec of processing. Since L_∞ is a function of fiber fraction, temperature, processing speed and therefore rate of deformation it is expected that a higher melt temperature possibly

leads to bigger L_∞ values. Furthermore, the steady state should be reached at a later point due to gentler processing condition (elevated temperature). It can be seen that the end FL values for PPGF30 samples processed at high temperature (280 °C), high processing speed (160 rpm) and varying residence time also approach the steady state. L_∞ is definitely reached after 120 sec of processing and displays an increased value of about 0.85±0.10 mm for L_N and 2.02±0.47 mm for L_W. It was therefore possible to prove that an increased temperature affects the value of L_∞ and leads to a bigger L_∞. However, it was not possible to show if L_∞ is reached at a later point of view due to increased temperature since no experiments were conducted below a residence time of 120 sec. It is important note that there is some variation present in the work. Especially for the value obtained from the 600 sec trial (160 rpm, 280 °C) which displays a lower value. One possible explanation for this low value is that material degradation took place in course of the experiment since high processing speed (160 rpm) and high temperature (280 °C) was used. However, results suggest that in this case the processing speed exceeds the impact of residence time, because even if the residence time is lowered at high processing speed (160 rpm) all end values still approach L_∞.
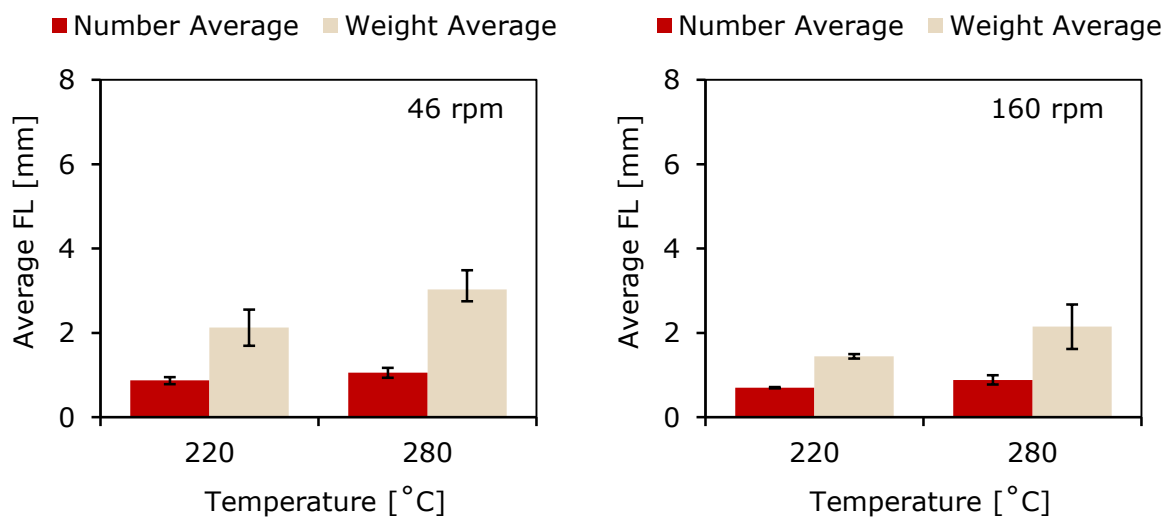
Figure 29: Results on the impact of melting temperature on the fiber breakage of PPGF30 for left: 46 rpm and 300 sec and right: 160 rpm and 300 sec.

Since the equilibrium value is also a function of the rate of deformation a reduced processing speed should lead to possibly higher L_∞ values which might be reached at a later point of view. Nevertheless, with the obtained data it was not possible to verify this hypothesis: Samples processed at high- and low temperature (220 °C

and 280 °C) and 46 rpm did not reach L_∞ after 120 sec of processing. Since no measurements were conducted at residence times higher than 300 sec it was not possible to detect if L_∞ was reached after 300 sec of shearing and therefore at a later point of view compared to the high processing speed trials.

Table 17 demonstrates the relative increase in L_N and L_W for PPGF30 as a function of melt temperature at varying process conditions. It can be seen that raising the temperature from 220 °C to 280 °C leads to a relative increase in L_W of 20 % at 46 rpm and of 50 % at 160 rpm for the low residence time trial (120 sec). The high residence time trial (300 sec) shows an identical relative increase in L_W of 30 % for the high- as well as for the low processing speed trial. A similar behavior can be observed for L_N: The same relative increase for L_N is noticed for low- and high processing speed experiments conducted at the same residence time.

Table 17: Relative increase in the number- and weight average FL for PPGF30 at varying processing conditions if the melt temperature is raised from 220 °C to 280 °C.

Residence time [sec]	Processing speed [rpm]	Relative increase in L_N [%]	Relative increase in L_W [%]
120	46	30	20
	160	30	50
300	46	20	30
	160	20	30
600	160	10	10
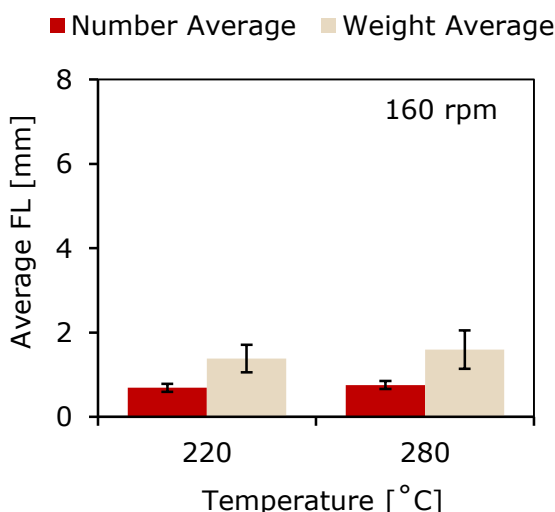
Figure 30: Results on the impact of melting temperature on the fiber breakage of PPGF30 for 160 rpm and 600 sec.

3.1.6 Validation of the PEC Fiber Length Measurement Technique

In order to ensure the validity of the obtained measurements, the applied FL measurement technique was compared to a third-party measurement system for selected samples.

Three different samples were defined and the outcome of both measurement concepts were compared. Figure 31, Figure 32, Figure 33 show the cumulative FLD of the PEC FL-measurement concept and the SABIC STAMAXTAT measurement technique (section 1.2.4.1) for PPGF30 at varying process conditions.

A strong agreement between the two measurement systems can be seen in the results. It should be noted that the SABIC technique is only able to measure FLs up to 12 mm (=dimensions of the sample) whereas the PEC measurement technique is not limited on the FL. Also, this comparative study was limited to one sample at each condition for the STAMAXTAT method. This method is assumed to be accurate and robust due to the fact that all fibers within a sample are measured, but the repeatability of the measurements cannot be quantified. In Figure 32 and Figure 33 a slightly higher fiber attrition can be noticed for the SABIC results, which should lead to higher average values in the PEC technique. A more detailed comparison of the two measurement techniques by providing the obtained numerical data (L_N and L_W) is shown in Table 18 and is graphically depicted in Figure 34.
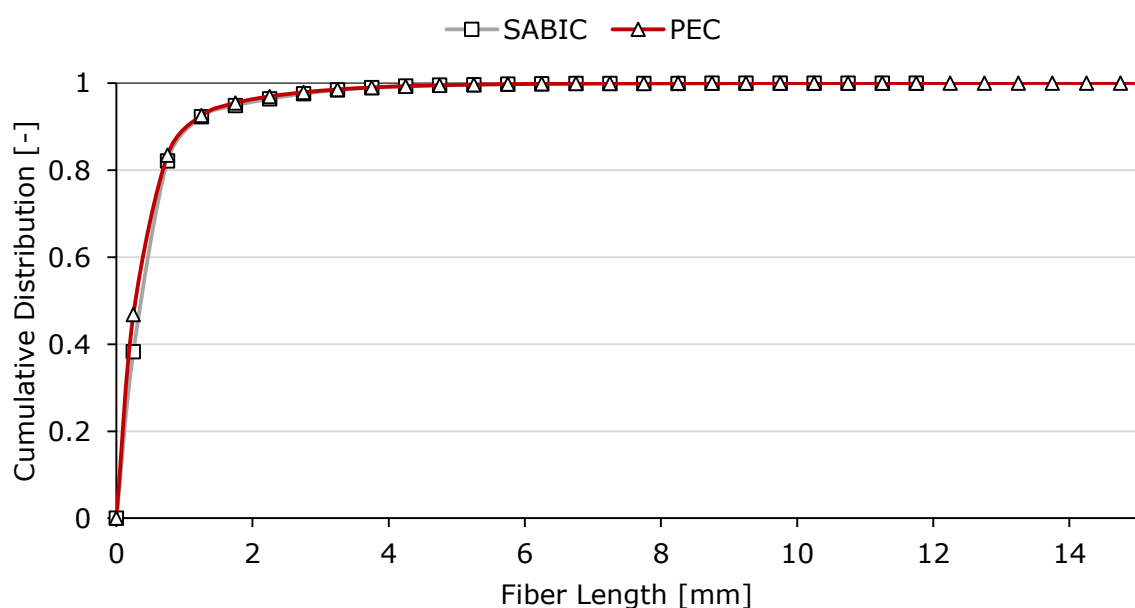
Figure 31: Cumulative FLD for PPGF30 processed at 220 °C, 160 rpm and 120 sec, respectively.
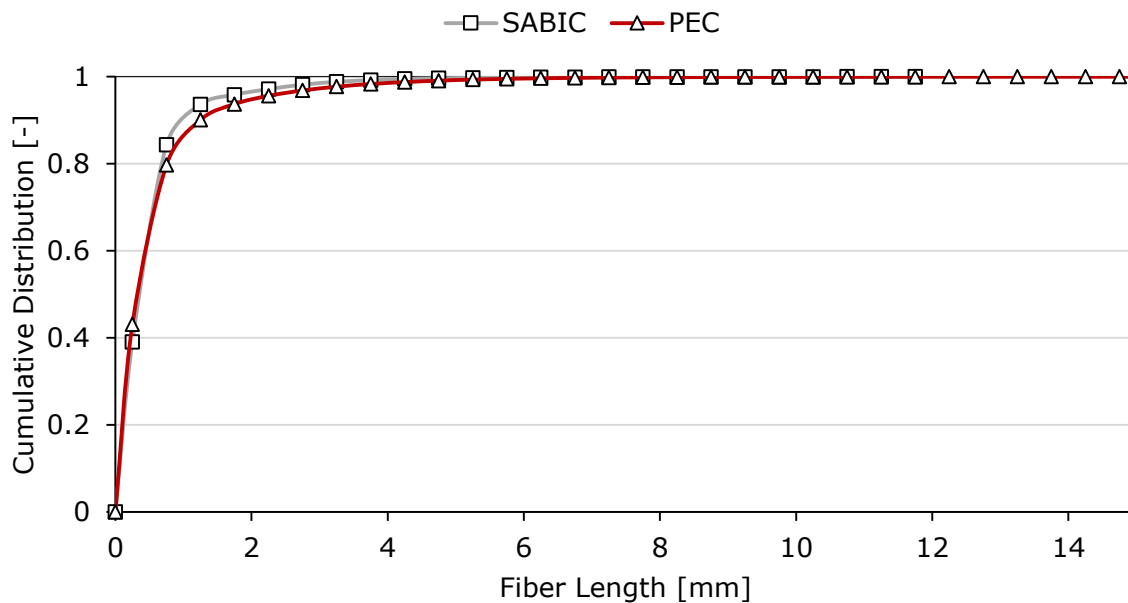
Figure 32: Cumulative FLD for PPGF30 processed at 220 °C, 160 rpm and 300 sec, respectively.
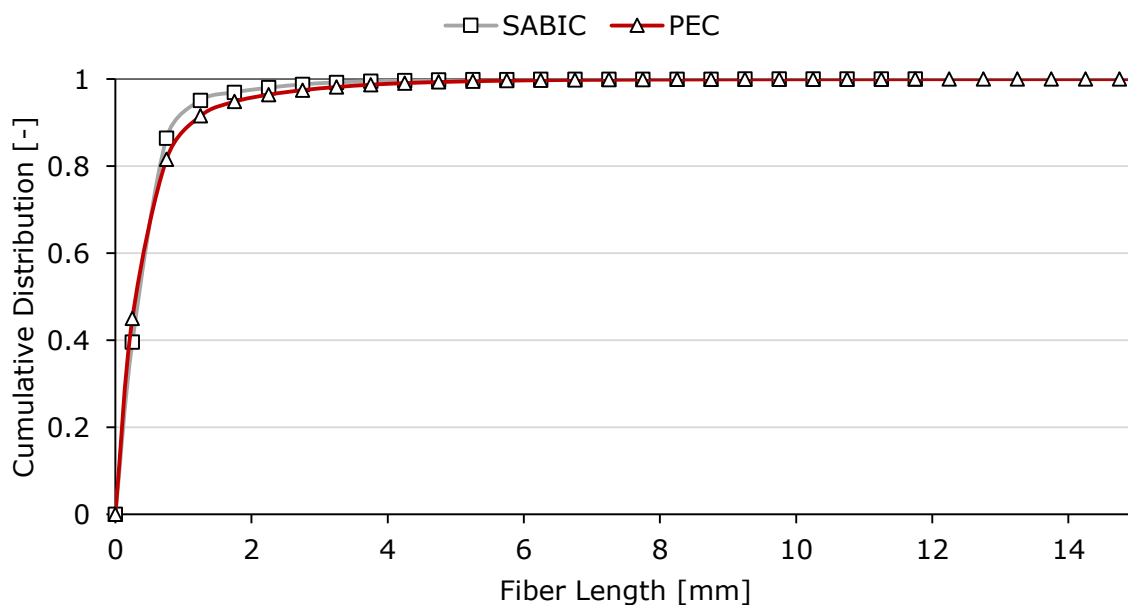
Figure 33: Cumulative FLD for PPGF30 processed at 220 °C, 160 rpm and 600 sec, respectively.

It can be seen in Table 18 and Figure 34 that for the two high residence time Couette trials (300- and 600 sec) the value for L_W measured by SABIC is lower than those obtained from the PEC FL-measurement technique. A possible explanation for this lower value is due to the inherent sample size limitation of the STAMAXTAT method. The maximum sample size is 12 mm x 12 mm x thickness. Consequently, longer fibers are likely to be cut during the extraction of the sample

from the molded part. Since all fibers in the test specimen are measured, also the cut fibers at the edges are included in the measurement. Thus, an error in the analysis and a skewing in the results can be expected. This especially effects L_W, since this value is strongly influenced by the occurrence of long fibers (Yilmazer and Cansever, 2002). This interpretation also enables to explain the higher SABIC values for L_N for most of the samples compared to those obtained from the PEC technique, since for L_N cut and therefore shorter fibers are weighted more (Yilmazer and Cansever, 2002).

Table 18: Average FL for PPGF30 at varying process conditions by using two different FL measurement concepts, the PEC FL-measurement technique and the STAMAXTAT method from SABIC, respectively.

Description	SABIC		PEC	
	L_N [mm]	L_W [mm]	L_N [mm]	L_W [mm]
220 °C, 46rpm, 120 sec	0.84	1.48	0.64±0.08	1.23±0.28
220 °C, 46rpm, 300 sec	0.80	1.34	0.70±0.02	1.45±0.05
220 °C, 46rpm, 600 sec	0.75	1.17	0.69±0.09	1.38±0.32
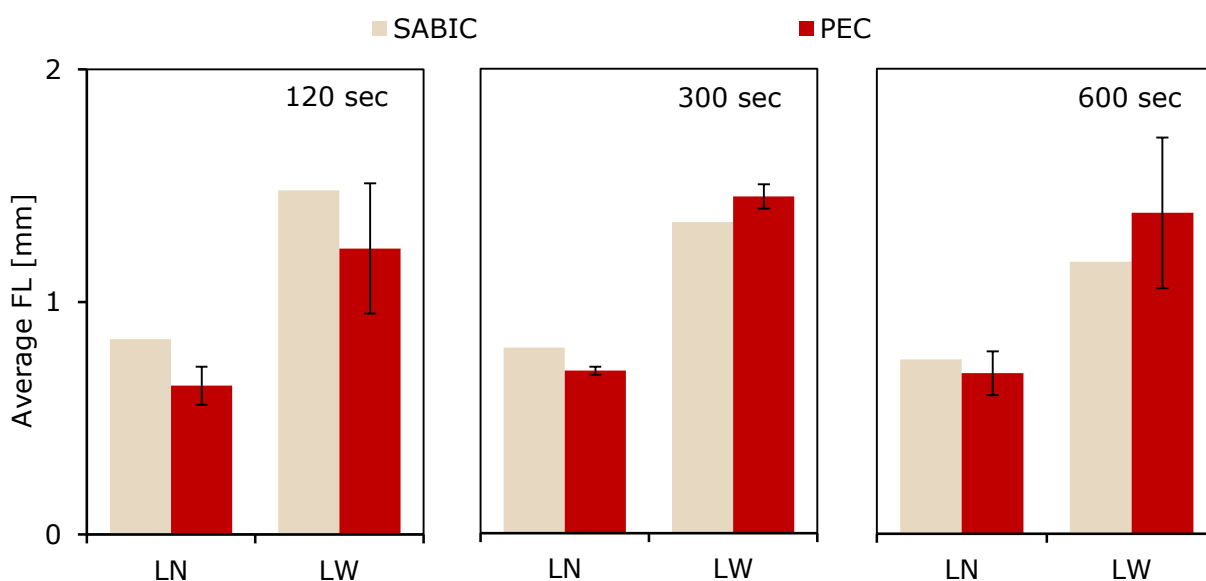
Figure 34: Average FL for PPGF30 processed at 220 °C, 160 rpm and varying residence times, by using two different FL measurement concepts, the PEC FL-measurement technique and the STAMAXTAT method from SABIC, respectively. Since the STAMAXTAT measurement technique allows a full analysis of all fibers in a sample no error bars are shown.

To conclude, the results indicate a strong agreement in the outcome of the two measurement techniques and backup the measurement technique used in this work.

3.2   Fiber-Matrix Separation

The FD over the part thickness was measured at five different positions along the flow path of the injection molded plaque (Position 1–5, Figure 16). In order to ensure the repeatability of the injection molding process two sets of samples were analyzed.

Figure 35 summarizes the FD distribution across the part thickness for all five sampling locations obtained from the µCT scans. The results for all locations suggest, a characteristic core-shell structure through the thickness of the plaque. A substantial fiber agglomeration in the core of the injection molded plaque is visible, reflected in an increased normalized FD of about 40 %.

Although this phenomena has not been fully understood yet, there are two hypothesis that explain this phenomena: First, shear induced particle migration might be responsible for the increased FD in the core since fibers migrate from high shear regions (near the mold wall) to lower shear regions (center of the part) (Morris and Boulay, 1999, Goris et al., 2016). Another explanation for this phenomenon is the Fiber-Pull-Out mechanism discussed in section 1.3 (Goris, 2016). This means that the fibers are pulled out of the frozen layers at the mold walls and swept along the molten core during mold filling. This leads to an agglomeration of fibers in the core as well as at the end of the part. Quantitatively, the peak in the FD in the core region is on average 40 % higher than the nominal FD value. Comparing the obtained results with literature reveals that within this study a slightly higher increase of FD was found in the core layer (Back, 2016, Lafranche et al., 2005, Akay and Barkley, 1991). Back, 2016 found that the FD peak in the core layer is about 30 % above the nominal value for PPGF40 (Back, 2016). Similar results were presented by Lafranche et al., 2005 who postulated a relative increase of about 25 % for a 40 %wt. glass fiber-reinforced PA66 and Akay et al., 1991 who found a relative increase of 30 % for a 50 %wt. fiber-reinforced PA (Lafranche et al., 2005, Akay and Barkley, 1991).

The results further show that the width and the height of the core peak slightly varies across the part length. Close to the gate (sampling location 1) the FD distribution shows a wide peak in the core of the plaque. In the center region and the end of the plaque the peak becomes slightly smaller and thinner. The results suggest that close to the gate the FD in the core peak is lower compared to other sampling locations, noticeable in an approximately 28 % increase in the FD near

the gate region, whereas the other core peaks showed an increase in the nominal FD of about 40 %. This finding does not correspond with the results presented by Back, 2016, who postulated a higher core peak near the gate region (Back, 2016).
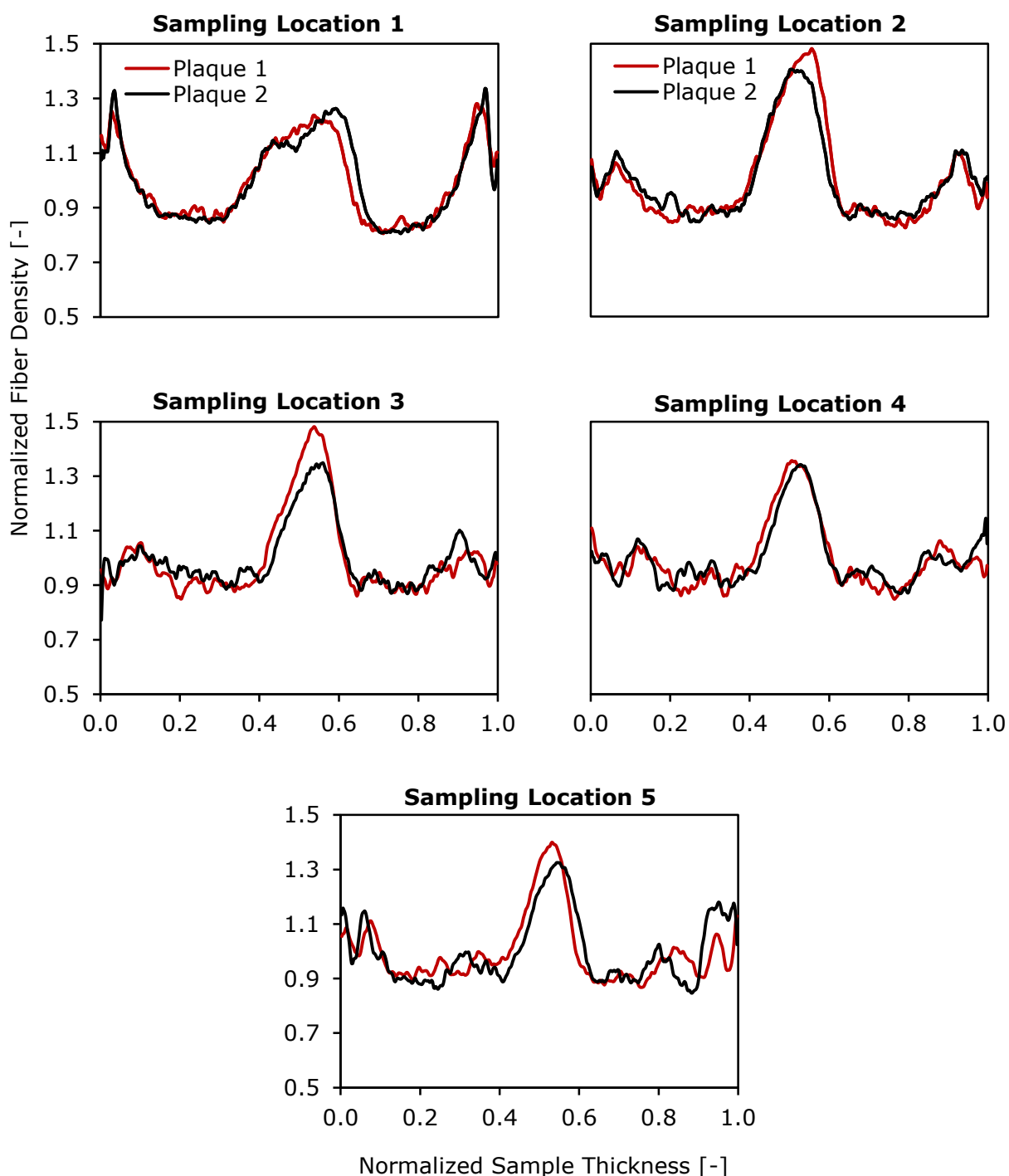
Figure 35: FD distribution over the part thickness for sampling region 1 till 5 for both injection molded plaques.

In the shell layers the FD is below the nominal FC. A density minimum on either side of the core is visible, where the density is up to -15 % lower than the nominal value. Furthermore, secondary peaks close to the surfaces can be found, which are approximately 0-15 % higher than the nominal FD. This secondary peak at sampling location 1 is higher than the main peak in the core layer. Since the plaque was molded with a 19.5 mm fan gate, a radial flow is present close to the gate (Figure 16), which might explain the difference in the shell-core structure of the FD distribution compared to the other locations.
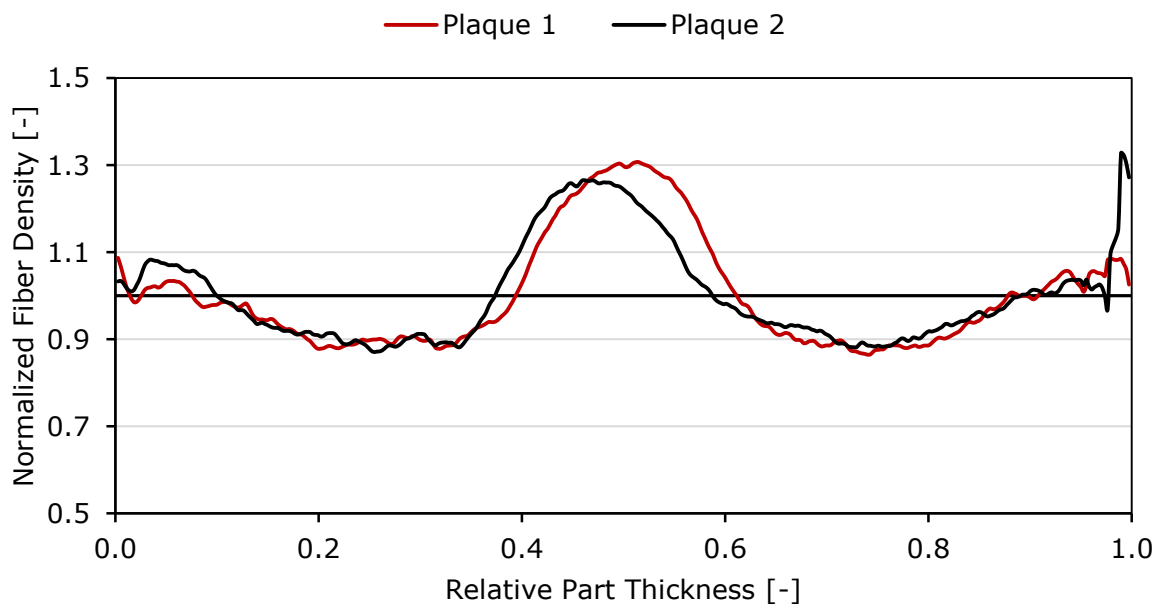
Figure 36: FD over the part thickness for two injection molded plaques processed at the same processing conditions (average of all measurement points along the flow path from Position 1 to Position 5).

In order to compare the FD distribution of the two plaques and therefore evaluate the repeatability of the injection molding process, the average over all sample locations (Position 1-5) was calculated. Figure 36 shows the average FD distribution of the two plaques. A good agreement between the two curves can be seen which confirms the repeatability of the injection molding process. The height and width of the core peak are similar. A slightly higher relative FD can be noticed for the core peak of plaque 1 with 1.30, whereas plaque 2 shows an average normalized FD of 1.27. Furthermore, a slight shift of the core peak is visible. No substantial difference within the shell layer can be noticed: The secondary peaks and the density minimum in the shell layers for both plaques are at the same level

and show the same height and width. It can be seen that plaque 2 shows an increase in the FD of 1.33 at a relative thickness of 1, which might indicate an increased heterogeneity throughout the part thickness.

Additional ashing tests were performed for samples along the flow path of the injection molded plaque to determine the local FD distribution. The results for the relative change of the FD along the plaque are shown in Figure 37 (left). The relative change was calculated according to Equation 29:

$$d_{relative} = \left(\frac{d}{d_{nominal}} - 1 \right) * 100$$

Equation 29: Relative change d$_{relative}$ of the local FD from the nominal value d$_{nominal}$.

It can be noticed that the measurements show a high degree of reproducibility with an overall standard deviation of less than 0.20 %. The results further demonstrate a local variation of the FD. The initial fiber weight fraction (=nominal FD) in the LFT pellets is 40 %wt. according to manufacturer SABIC. The measurements therefore reveal a low FD close to the gate (approx. 38. %wt.) and a maximum FD at the end of the flow path (approx. 41 %wt.). This fiber agglomeration at the end of the plaque can be again explained with the Fiber-Pull-Out mechanism which leads to an increase in FD in the core as well as at the end of the part (Goris, 2016).
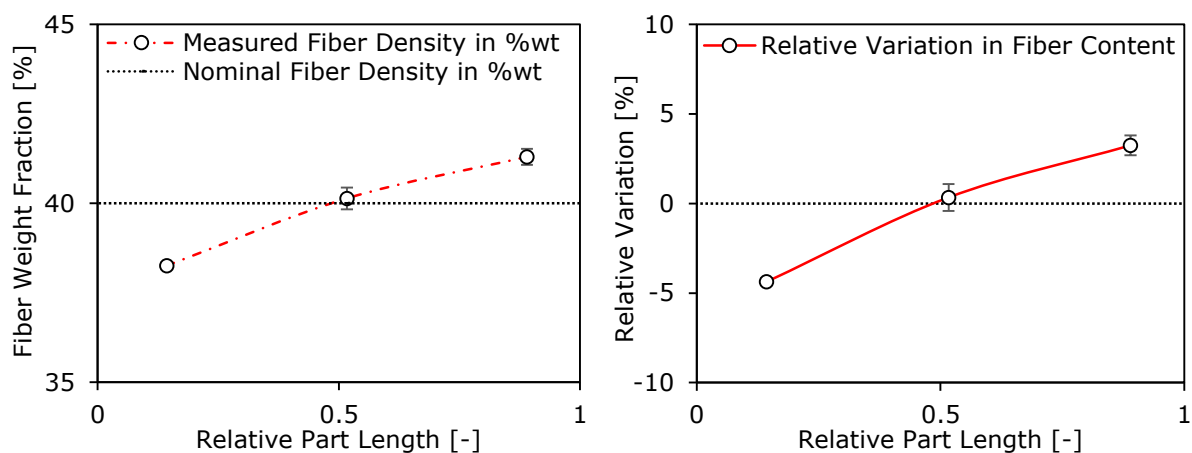
Figure 37: Left: FD variation along the flow path (average of plaque 1 and plaque 2). Right: Variation in the FD along the flow path relatively to the nominal FD (average of plaque 1 and plaque 2).

If the obtained FD results are plotted relative to the nominal fiber content, the deviations range from -4.4 % to +3.2 %, as shown in Figure 37 (right). This finding correspond with studies published in literature: According to Lafranche, 2007 and Toll et al., 1993 the difference in FD between the beginning and end of the part lies between 5 % and 10 % (Lafranche, 2007, Toll and Andersson, 1993, Back, 2016).

The FLD was measured at three sampling locations along the injection molded part (distance from the gate to the center of the sampling location: 43 mm (Pos. 1), 155 mm (Pos. 2) and 267 mm (Pos. 3), Figure 16). At least 28000 fibers per sample were measured to obtain reliable results. Figure 38 (left) shows the normalized cumulative length distribution and Figure 38 (right) shows the average values for all three sampling locations. It can be seen that the FL is not constant along the part length. The number average FL increases from 0.58 mm at sampling position 1 to 0.76 mm for location 5. The weight average FL rise from 1.52 mm at location 1 to 2.09 mm for sampling position 5. The results demonstrate an increase in the average FL towards the end of the flow path. In order to fully verify the obtained results additional measurements per sampling location are recommended since one repetition per location may not be representative.
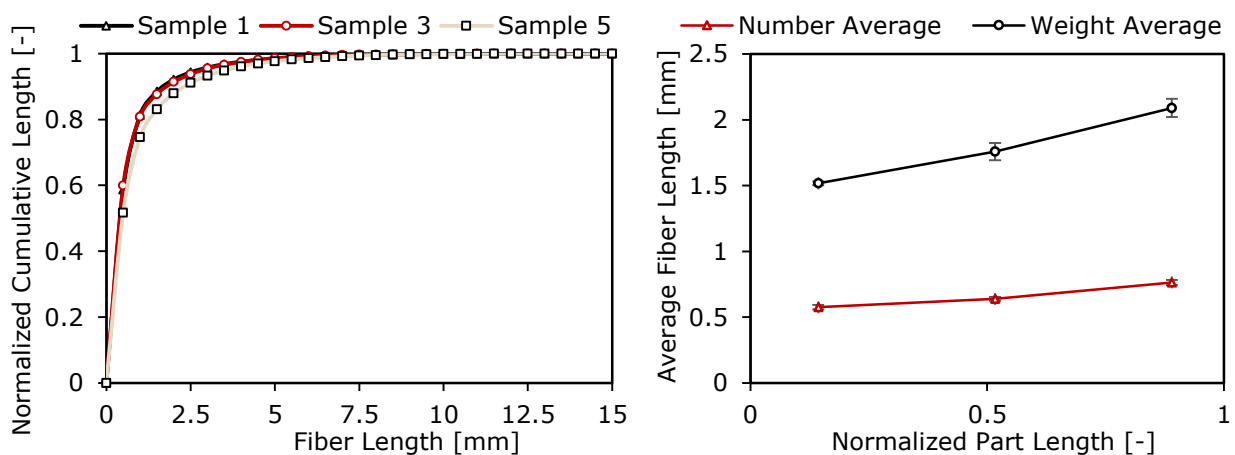
Figure 38: Left: Normalized cumulative FLD for sampling positions 1,3 and 5 (average of plaque 1 and plaque 2). Right: Number- and weight average FL along the flow path (average of plaque 1 and plaque 2).

All these results prove that the assumption of a uniform FL and FD in injection molded plaques is not valid. This heterogeneity of the fiber architecture needs to be taken into account for material modeling and structural analysis to increase the confidence level of LFTs. It is important to note that current approaches for LFT

modeling and structural analysis still assume that FL and FD are uniform throughout the part and this may cause errors in the simulation results. Furthermore, it may be concluded from these substantial deviations that the area close to the gate has decreased mechanical properties due to reduced FL and lower FD, while the end-of-flow area would have increased material properties since a larger FL and an increased FD was found (Goris and Osswald, 2016).

3.3   Modeling and Simulation Results

3.3.1 Evaluation of the Single Particle Model

The experimentally determined FL reduction over time is compared to the single particle model predictions (Perez et al., 2016a). The outcome of the comparison is shown in Figure 39.
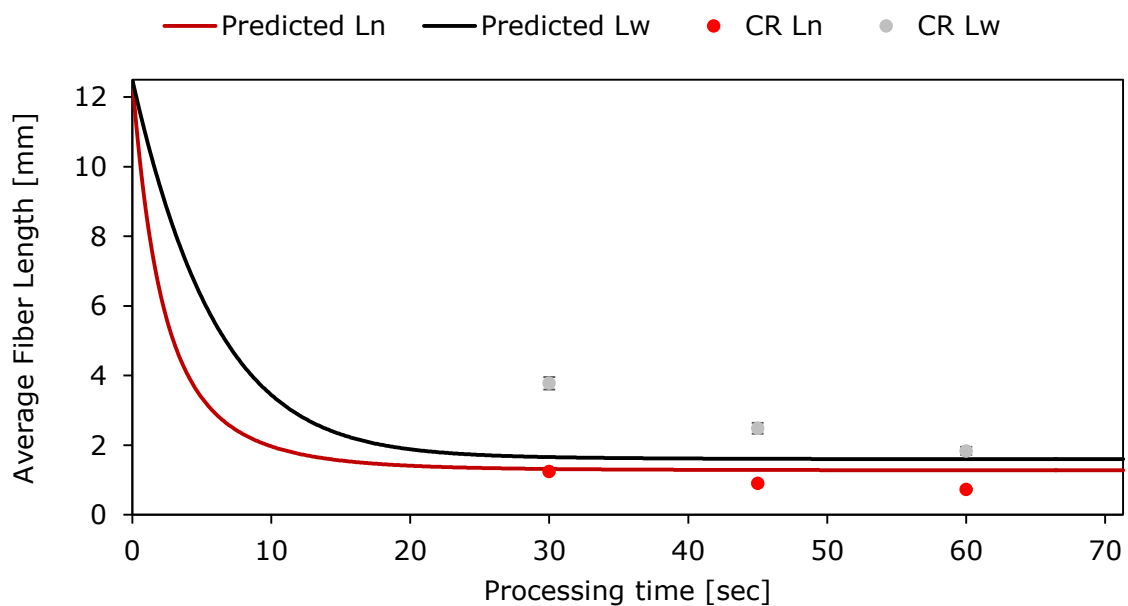
Figure 39: Predicted and experimentally determined FL reduction over time for PPGF30.

It can be seen that the fiber attrition displays an exponential decay function. Shon et al., 2005 proposed a model (differential equation) in which an average FL decreases towards an equilibrium value (L_∞). This model can be used to describe the found decay function. After solving the differential equation stated by Shon et al., 1983 the following decay function is obtained (Shon et al., 2005):

$$L_t = (L_0 - L_\infty)e^{-k_f t} + L_\infty$$

Equation 30: Exponential decay function, where L_t is the FL at a time t, L_0 the initial FL, L_∞ the unbreakable length and k_f a fitting parameter (exponential decay constant), respectively (Shon et al., 2005).

It is noticeably that significant fiber breakage occurs till a shearing time of 30 sec. Subsequently, L_∞ is reached at approximately 49.5 sec and is 1.28 mm for L_N and 1.60 mm for L_W (Table 19). This means a total reduction from the initial FL (=12.5 mm) of 90 % for L_N and 87 % for L_W.

Table 19 summarizes the most important parameters to describe the observed FL over time modeled as a decay function. It can be seen that the value of L_∞ is higher for the particle level simulation compared to the Couette rheometer trial. It is further noticeable that L_∞ of the L_W value from the simulation and the experimental work are very similar compared to L_∞ of the L_N values. L_∞ of the L_N value for the simulation approach has twice the size of the value obtained from the experiments. Additionally, a significant longer residence time is observed for the Couette trial to reach the steady state. Moreover, it seems that the rate of decay for L_N and L_W is higher for the single particle simulation approach.

Table 19: Comparison between the experimentally determined- and the predicted FL decay function by presenting the most important parameters, where L_N is the number average FL, L_W the weight average FL, L_∞ the unbreakable FL and t the time required to reach L_∞.

		Couette rheometer		Single particle model	
Description	**Units**	**L_N**	**L_W**	**L_N**	**L_W**
L_∞	mm	0.68±0.05	1.45±0.18	1.28	1.60
t	sec	60.00	60.00	49.50	49.50

It is important to note that the available data only allows a qualitative comparison between the experimental- and the predicted values. This is due to two simplifications of the single particle approach: First, the single particle model assumes fully dispersed fibers as the initial state of the shear cell, whereas the fibers are initially bundled up in the Couette rheometer. Consequently, there is a certain time period until the fibers are fully dispersed and impregnated in the experimental study. Second, the initial FLs in the simulation and in the experimental work are different, displayed in an initial FL of 12.5 mm in the simulation and 15 mm in the pellets used for the Couette trials. This is due to

current computational limitation in the single particle model that does not allow larger FLs. Nevertheless, the comparison showed a good agreement between the experimentally- determined and predicted FL values with both results suggest an exponential-decay-type behavior and approach similar L_∞ values.

3.3.2 Evaluation of the Phelps Model

All experimentally results obtained from the Couette rheometer experiments were successfully used to fit the three parameters. The optimum set of fitting parameters for each material and each processing condition is shown in the appendix.
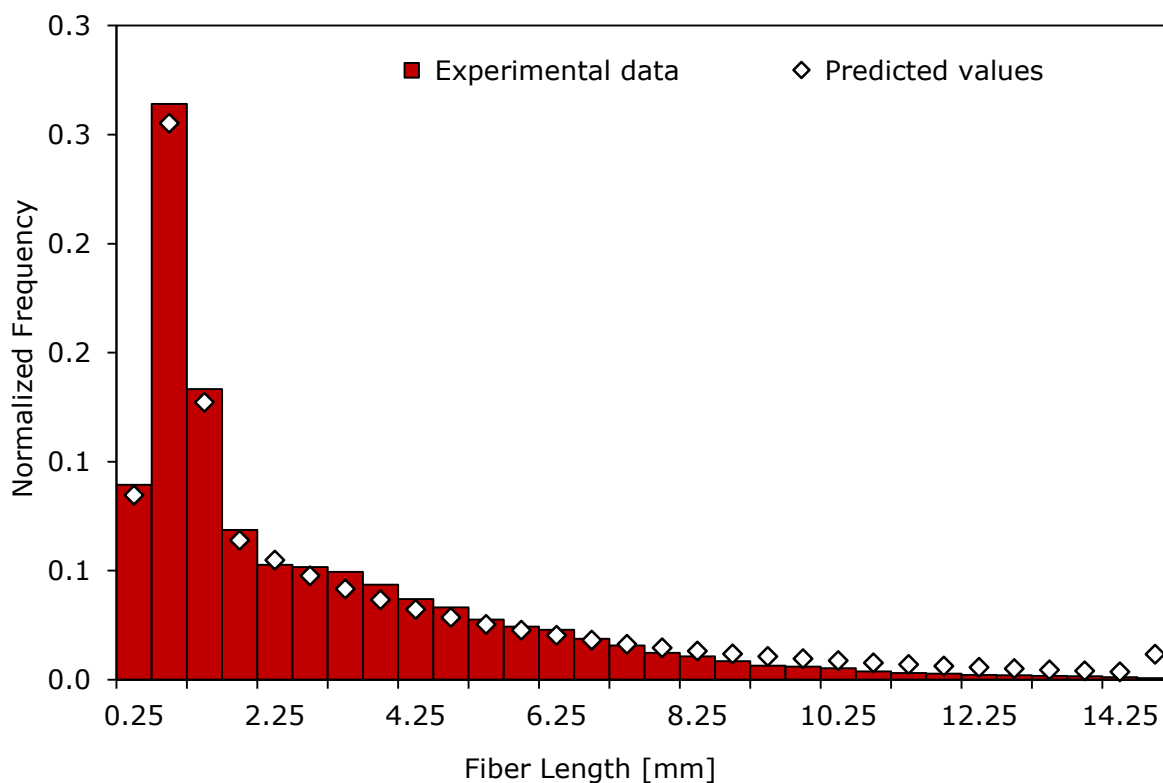
Figure 40: Experimental (bars) and predicted (dots) normalized weight-based fiber length distribution for 300 sec, 46 rpm, 220 °C and 30%wt.

The examination of the fiber breakage model started by plotting the obtained experimental data from the Couette rheometer experiments with the predicted values. Figure 40 exemplary demonstrates a fit between the experimental data and the predicted values. It can be seen that the Phelps's model for fiber breakage

prediction was applied successfully and that a good fit (low error) between experimental- and predicted values could be achieved.

Table 21 shows the relative error between the experimentally determined values and the predicted values for PPGF30 at varying processing conditions. It can be seen that it was not possible to fully verify the material dependency of the model parameters.

Experiment 2, 9 and 14 support the material dependency hypothesis since a change in processing conditions do not increase the relative error. To name an example: If the model parameters from experiment 2 are used to simulate the remaining 30 %wt. experiments (varying processing conditions) the relative standard deviation within the experimental measurements is approximately 30 % for L_W. This finding supports the claim that the model parameters are material dependent.

However, the fit between experimental data and predicted values for experiment 10, 11 and 12 reveal that variations in processing conditions increase the relative error. A good fit could only be achieved if an experiment was fitted to itself. Model parameters for the same material did not accurately predict the fiber breakage from another experiment. Therefore, the relative error is far higher than the standard deviation and the material dependency of the model parameters could not be supported.

Similar results are obtained for PPGF20 and PPGF40 (Table 20, Table 22). For some cases the fitting parameters from one experiment were perfectly able to accurately predict the FLD from another run leading to a low relative error in the color matrix. But for a greater part the parameters were not suitable to predict the FLD for another experiment, noticeable in large relative errors up to 250 %. Those results show again that the model parameters cannot be treated as material dependent.

Table 20: Relative error between experimental data and predicted values for various processing conditions and a fiber concentration of 20%wt.

	Description	Exp 1	Exp 2	Exp 3	Exp 4
	Processing conditions	280°C 46rpm 120sec	280°C 46rpm 300sec	280°C 160rpm 120sec	280°C 160rpm 300sec
Fitted Model Parameters	Exp 1	0.02	0.22	0.28	0.47
	Exp 2	0.25	0.03	0.01	0.73
	Exp 3	0.25	0.03	0.01	0.73
	Exp 4	0.51	0.64	0.93	0.05

Table 21: Relative error between experimental data and predicted values for various processing conditions and a fiber concentration of 30 %wt.

Description	Exp 1	Exp 2	Exp 3	Exp 4	Exp 5	Exp 6	Exp 7	Exp 8	Exp 9	Exp 10	Exp 11	Exp 12	Exp 13	Exp 14
Processing conditions	220°C 46rpm 120sec	220°C 46rpm 300sec	220°C 160rpm 30sec	220°C 160rpm 45sec	220°C 160rpm 60sec	220°C 160rpm 90sec	220°C 160rpm 120sec	220°C 160rpm 300sec	220°C 160rpm 600sec	280°C 46rpm 120sec	280°C 46rpm 300sec	280°C 160rpm 120sec	280°C 160rpm 300sec	280°C 160rpm 600sec
Exp 1	0.01	0.26	0.18	0.18	0.13	0.05	0.06	0.33	0.29	0.22	0.39	0.47	0.44	0.27
Exp 2	0.03	0.05	0.20	0.25	0.26	0.31	0.26	0.00	0.10	0.17	0.22	0.26	0.18	0.06
Exp 3	0.12	0.34	0.06	0.02	0.04	0.09	0.16	0.36	0.30	0.30	0.44	0.50	0.44	0.27
Exp 4	0.12	0.36	0.06	0.01	0.07	0.15	0.20	0.36	0.29	0.30	0.50	0.51	0.44	0.27
Exp 5	0.04	0.46	0.16	0.12	0.01	0.22	0.38	0.55	0.50	0.25	0.59	0.67	0.69	0.59
Exp 6	0.01	0.29	0.18	0.17	0.11	0.01	0.13	0.36	0.30	0.22	0.42	0.49	0.44	0.27
Exp 7	0.68	0.41	0.71	0.56	0.39	0.10	0.02	0.18	0.10	0.69	0.47	0.44	0.36	0.20
Exp 8	0.44	0.13	0.41	0.35	0.20	0.11	0.20	0.00	0.10	0.49	0.27	0.24	0.14	0.08
Exp 9	0.04	0.13	0.13	0.14	0.14	0.20	0.17	0.11	0.07	0.23	0.31	0.30	0.19	0.06
Exp 10	0.19	0.58	0.30	0.50	0.72	1.16	1.24	0.78	0.92	0.01	0.32	0.34	0.56	1.03
Exp 11	0.36	0.26	0.45	0.16	0.15	0.69	0.84	0.55	0.70	0.38	0.03	0.11	0.31	0.70
Exp 12	0.36	0.26	0.45	0.16	0.15	0.69	0.84	0.55	0.70	0.38	0.03	0.11	0.31	0.70
Exp 13	0.03	0.08	0.18	0.25	0.31	0.46	0.46	0.18	0.30	0.16	0.10	0.12	0.02	0.24
Exp 14	0.04	0.13	0.13	0.14	0.14	0.20	0.17	0.11	0.07	0.23	0.31	0.30	0.19	0.06

(Row label for left axis: **Fitted Model Parameters**)

Table 22: Relative error between experimental data and predicted values for various processing conditions and a FC of 40%wt.

Description		Exp 1	Exp 2	Exp 3	Exp 4
Processing conditions		280°C 46rpm 120sec	280°C 46rpm 300sec	280°C 160rpm 120sec	280°C 160rpm 300sec
Fitted Model Parameters	**Exp 1**	0.00	0.19	0.42	0.37
	Exp 2	0.31	0.13	0.36	0.50
	Exp 3	0.61	0.78	0.09	0.47
	Exp 4	1.14	2.51	1.68	0.02

If the three fitted model parameters are material dependent a change in material (varying FC) would result in high relative errors since the obtained parameters from one system cannot be used in other systems. In order to investigate this assumption, the model parameter from one material are used to predict the FLD from another material. The results are shown in Table 23 and Table 24.

Table 23: Relative error between experimental data and predicted values for constant processing conditions (left: 280 °C, 46 rpm, 120 sec, right: 280 °C, 46 rpm, 300 sec) and varying FCs (PPGF20, PPGF30, PPGF40).

Description		Exp 1	Exp 2	Exp 3
Material		20%wt	30%wt	40%wt
Fitted Model Param.	**Exp 1**	0.02	0.28	0.70
	Exp 2	0.17	0.01	0.30
	Exp 3	0.40	0.24	0.00

Description		Exp 1	Exp 2	Exp 3
Material		20%wt	30%wt	40%wt
Fitted Model Param.	**Exp 1**	0.03	0.73	2.36
	Exp 2	0.35	0.03	0.97
	Exp 3	0.64	0.40	0.13

Table 24: Relative error between experimental data and predicted values for constant processing conditions (left: 280 °C, 160 rpm, 120 sec, right: 280 °C, 160 rpm, 300 sec) and varying FCs (PPGF20, PPGF30, PPGF40).

Description		Exp 1	Exp 2	Exp 3
Material		20%wt	30%wt	40%wt
Fitted Model Param.	**Exp 1**	0.01	0.68	1.52
	Exp 2	0.33	0.11	0.51
	Exp 3	0.54	0.26	0.09

Description		Exp 1	Exp 2	Exp 3
Material		20%wt	30%wt	40%wt
Fitted Model Param.	**Exp 1**	0.05	1.12	2.42
	Exp 2	0.48	0.02	0.51
	Exp 3	0.67	0.33	0.02

It can be seen that low relative errors could only be achieved if the experiment was fitted to itself which means a good fit between the experimental and predicted values from the same experiment. Model parameters from one experiment (=from one material) were not able to accurately predict the FLD from another experiment (=different material). Apart from one case we get high relative errors up to 240 %. This indicates that one or more of the parameters are a function of the FC, which

has not been incorporated or stated before (Phelps et al., 2013). This reaffirms some of the findings from Table 21, Table 20 and Table 22. Nevertheless, the overall results show that the model parameters cannot be treated as material dependent yet since some of the findings are not supporting this hypothesis.

The necessary characteristic for a predictive tool is the fact that the model parameters are known or can be determined beforehand, which can be achieved by material depended parameters. The findings of this work indicate that the model parameters can be fitted to all experimental results individually. However, the parameters cannot be transferred for the same material within the trials at different processing conditions. Also, the results suggest that there is a dependency on the FC, which is currently not incorporated in the Phelps model. As a result of this it was not possible to validate Phelps's fiber breakage model nor to find a process to find the model parameters beforehand. Therefore, the usefulness of the model as a predictive tool is not given at this point. It is necessary to develop a methodology that allows to find the parameters for the Phelps model.

3.3.3 Fiber Breakage Prediction in Injection Molding Simulation

The optimum set of fitting parameters (Phelps's model, Appendix Table 1) for each PPGF40 Couette rheometer trial was used as an input parameter for Moldex3D simulations (Figure 41).
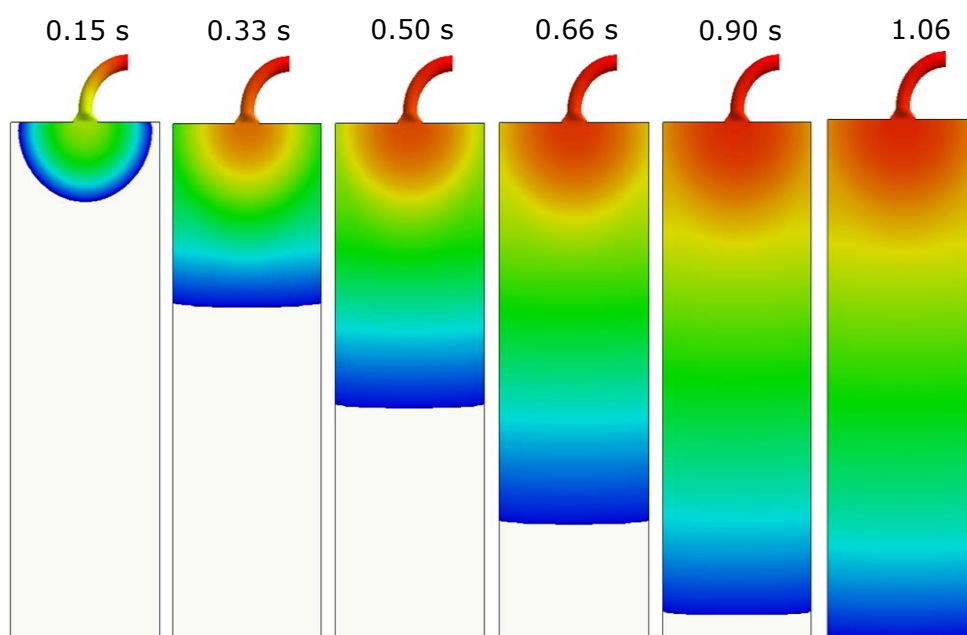

Figure 41: Mold filling (Melt front line) of the injection molded plaque (Moldex3D).

The simulations are based on the assumption that the model parameters are material dependent. The predicted weight average FLs are presented in Table 25. Furthermore, the predicted weight averages by using the Moldex3D default model parameters and the experimentally determined weight averages (PEC FL measurement technique) are demonstrated in Table 25.

Table 25: Comparison between predicted and experimentally determined L_W at three different sampling locations (distance from gate: 43 mm (=1), 155 mm (=2) and 267 mm (=3), Figure 16). Phelps model parameter 1-4 describe the use of the fitting parameters obtained from the Phelps model calculation for PPGF40 as an input for the Moldex3D simulation. Moldex3D default describes the use of the Moldex3D default fitting parameters to predict the average Fls in the injection molded plaque.

Description	Weight average FL [mm]		
Sample position	1	2	3
Phelps model parameter 1	4.46	4.44	4.43
Phelps model parameter 2	4.53	4.52	4.51
Phelps model parameter 3	4.58	4.58	4.57
Phelps model parameter 4	4.66	4.66	4.66
Moldex3D default	2.03	1.83	1.75
Experimental values	1.53	1.81	2.14

The experimental data demonstrate that the initial fibers of 15 mm length are reduced in course of the injection molding process by 86 up to 90 %. It can be seen in Table 25 that the end FL is lower near the gate and higher at the end of the plaque. These increasing FLs along the flow path can be explained with the Fiber-Pull-Out mechanism described in section 1.3, which assumes that partially embedded fibers are pulled out of the solidified layers and are swept along with the molten core leading to an accumulation of longer fibers at the end of the plaque (Toll and Andersson, 1993). Additional measurements are recommended in order to verify and ensure the reliability of this finding.

By using the fitting parameters obtained from the Phelps's model calculation to predict the weight average FLs of an injection molded plaque it can be seen that the fibers experience almost no breakage. The weight average FL at the end of the gate/beginning of the plaque was set to 4.75 mm (experimentally determined value). Therefore, a total reduction in FL of about 0.1-0.3 mm occurred.

If using the Moldex3D default fitting parameters to predict the weight averages an increased fiber attrition is visible, displayed by a FL reduction from 4.75 mm (end of the gate/beginning of the plaque) to approximately 3 mm (=63.16 %). These predicted values are more similar to the experimental data. The weight average

FL for sampling location 2 perfectly matches the experimental value. If using the Moldex3D default values a continuous decrease in the end FL along the flow path is visible. This phenomenon can be explained with the Fiber-Breakage mechanism described in section 1.3, which assumes that the flow of the molten core shears off the embedded fibers which are then swept along and agglomerated at the end of the part (Lafranche et al., 2005, Akay and Barkley, 1991).

It is important to note that the Moldex3D default fitting parameters do not have any justification at this point since there is no information available of how these parameters have been created and therefore an accurate fiber breakage prediction cannot be ensured.

Since the obtained results are contradictory and did not meet our expectations the used fitting parameters are examined more closely (Table 26).

Table 26: Fitting parameters for the Moldex3D simulation approach to predict the weight average FL in an injection molded plaque, where C_B is the breakage coefficient, ζ the hydrodynamic drag coefficient and S the distribution shape factor, respectively.

Description	Material	C_B	ζ	S
Phelps et al., 2013	Injection molding process, 40%wt., fiber diameter 17µm, fiber modulus 73GPa	0.0250	0.5500	1.0000
Moldex3D default values	-	1.0200	3.0000	0.2500
Parameters obtained from Phelps model calculation	Couette Rhoemeter, 40%wt., Initial FL 15 mm, fiber diameter 19µm, fiber modulus 73GPa	0.0015	1.6815	1.9994
		0.0011	4.9999	1.9994
		0.0008	2.2291	1.4959
		0.0004	1.9116	1.9931

It can be seen from Table 26 that our obtained C_B values are smaller (up to three magnitudes) than the Moldex3D default value and the one presented by Phelps et al., 2013. The ζ coefficient is bigger than the value presented in the Phelps's paper. The obtained low C_B values can be explained by the basic conservation equation for FL (Equation 13). It can be seen that the rate of change of FL (dN/dt) is proportional to the breakage probability (P_i). Since the Couette rheometer trials present large residence times (120 sec up to 600 sec) the time factor in Equation 13 is large resulting in a small breakage probability. This approach explains the low fiber breakage in the Moldex3D simulations. It can be deduced then that the parameters obtained by fitting the model to Couette experiments

("mild" conditions) cannot be used to predict the end FL in injection molding simulations ("harsh" conditions) since the time scales are so different the fibers experience almost no breakage (L_N and L_W are being overestimated).

The drag coefficient ζ appears in the numerator of the dimensionless variable for buckling (B_i) (Equation 16). This means B_i is proportional to ζ. But it is important to note that Bi is a function of ζ, the matrix viscosity, the scalar magnitude of D (shear rate), the FL, the elastic modulus of the fiber and the fiber diameter. Since B_i is present inside the negative exponent of the breakage probability P_i (Equation 15) with values close to the unit it can be deduced that C_B has a bigger impact in the overall breakage rate.

When comparing Couette rheometer experiments with injection molding trials it is important to note the differences between those two processes: Couette trials introduce low shear rates (since processing speed is limited due to the maximum capacity of the machine, maximum=59 s^{-1}) and long residence times (since a minimum time is required to achieve sufficient dispersion of the material, minimum time required=30 sec), whereas injection molding introduces high shear rates of 300-500 s^{-1} and short residence times of about 0.5-1 sec. Phelps et al., 2013 obtained their model parameters by fitting their model to experimental data of an injection molding process and then predicted the fiber breakage in an injection molding part, whereas the present work obtained the parameters by fitting the model to the experimental data of a Couette rheometer experiment and then tried to predict the fiber breakage in an injection molding part. As already stated, the outcome of this work suggest that the model parameters obtained by fitting the model to Couette experiments cannot be used to predict in injection molding simulations.

However, one approach to account for changes in residence time and rate of deformation might be through the dimensionless time defined by Phelps et al., 2013, which accounts for the total deformation, by using Equation 31 (Phelps et al., 2013):

$$t^* = C_B \dot{\gamma} t$$

Equation 31: The breakage parameter C$_B$ is reported in terms of a dimensionless time t* to enable reliable fiber breakage predictions for injection molding processes. $\dot{\gamma}$ is the shear rate and t the time, respectively (Phelps et al., 2013).

The dimensionless time (t*) for each of the PPGF40 Couette rheometer trials was calculated by multiplying the fitted C_B value from the Phelps model calculation with the corresponding shear rate and residence time of the respective Couette trial. Subsequently, the parameter C_B^{IM}* for the injection molding simulation is obtained from t* of the Couette rheometer experiment by adjusting the shear rate and residence time to the injection molding process.

The injection molding process has an injection time of 1 sec. Since the geometry of the injection molded plaque is known (dimensions of 102 mm x 305 mm x 3.2 mm) the shear rate of the injection process can be calculated according to Equation 32:

$$\dot{\gamma} = \frac{6 * Q}{W * H^2}$$

Equation 32: Apparent shear rate in injection molding for rectangular channels, where Q is the volumetric flow rate of the polymer in m^3/s, W the gate width in m and H the gate thickness in m, respectively.

The volumetric flow rate is determined according to Equation 33:

$$Q = \frac{V}{t}$$

Equation 33: Polymer flow rate in m^3/s, where V is the volume of the plaque in m^3 and t the injection time of the injection molding process in sec.

The calculated shear rate for the injection molded plaque as well as for the gate are shown in Table 27.

Table 27: Polymer flow rate and shear rate of the injection molded plaque and the gate. Dimensions of the gate: gate length 75 mm, gate width 19.1 mm. It is assumed that the gate thickness is the part thickness which is 3.2 mm.

Description	Unit	Plaque	Gate
Volumetric flow	m/s^3	995520e-10	995520e-10
Shear rate	s^{-1}	572	3054

The C_B values from the Phelps model calculation and the t* for the PPGF40 Couette trials as well as the C_B parameters reported in terms of a dimensionless time (C_B^{IM}*) are shown in Table 28.

It can be seen that the C_B^{IM}* values which are now accounted for in terms of a dimensionless time are bigger compared to the C_B values. This agrees with the

hypothesis stated in this work: Smaller residence times should lead to smaller time factors in Equation 13 and therefore an increased breakage probability should be observed leading to more realistic L_N and L_W values. To validate this statement future work should include using the new calculated $C_B^{IM}*$ values as input parameters for the Moldex3D simulation to predict fiber breakage in an injection molded plaque. Also, the dependency of the hydrodynamic parameter needs to be evaluated in terms of its dependency of the shear rate and residence time.

Table 28: Comparison of C_B and $C_B^{IM}*$.

Description Couette trial	280 °C 16.9 s^{-1} 120 sec	280 °C 16.9 s^{-1} 300 sec	280 °C 58.8 s^{-1} 300 sec	280 °C 58.8 s^{-1} 300 sec
C_B	1500e-6	1096e-6	803e-6	400e-6
t*	3.042	5.55672	5.6630772	358.7704
$C_B^{IM}*$	5318e-6	9715e-6	9901e-6	627221e-6

Furthermore, the Phelps model should be fitted to injection molding experiments to establish a consistent comparison between the experiment, literature and commercial software. But it is important to keep in mind that the process injection molding introduces many variables to the study.

4 Discussion and Conclusion

The experimental investigation of processing long glass fiber-reinforced thermoplastics focused on the fiber breakage and fiber-matrix separation. The FL degradation was investigated under controlled conditions in a Couette flow. The impact of processing conditions (FC, temperature, processing speed and residence time) on fiber attrition was quantified. The results of this work clearly show that the Couette rheometer is a feasible device to isolate and quantify the impact of processing conditions on the residual FL.

The results indicate that all factors (FC, melt temperature, processing speed, residence time) do have a significant effect on the fiber attrition. It was shown that a higher FC causes more fiber attrition due to increased fiber-fiber interactions as well as larger suspension viscosity. The obtained data further suggest that L_N and L_W reduces linearly with increasing FC within the range of 20 %wt. to 40 %wt., which represents industrial relevant FC. Additionally, the results suggest that L_∞ is a function of FC. It was able to demonstrate that an increase in FC leads to lower FL end values. Consequently, a higher FC of the same fibers might not yield to the expected increase in mechanical performance due to the additional fiber attrition caused by the evaluated fiber-fiber interactions. An increase in temperature reduces fiber breakage as melt viscosity is lowered, which results into lower stresses acting on the fibers. Results further indicate that L_∞ is also a function of temperature, noticeable that an increase in melt temperature results in bigger L_∞ values compared to the low temperature counterpart. Increased processing speed leads to a larger total deformation that fibers are exposed and to more fiber interactions and therefore accelerated fiber breakage. Results were able to prove that samples processed at high and low temperature, as well as varying residence time all approach L_∞ if processed at a high processing speed. It can be therefore assumed that the factor processing speed has a bigger impact on fiber breakage than the residence time.

A longer residence time promotes fiber degradation as fibers are more likely to be exposed to various fiber breakage mechanisms. It could be shown that fiber breakage is a function of time with an exponential type of length reduction. A total reduction from the initial FL to a steady state value of 90 % was found for L_W. This degree of fiber breakage is aligned with reports in the literature from injection

molding studies that commonly suggest 85 to 95 % FL reduction. Additionally, the results suggest that the factor processing speed has the biggest impact of all processing variables on the residual FL and therefore exceeds the impact of residence time, melt temperature and FC.

Results from the FD measurements of injection molded plaques show substantial variation through the thickness as well as along the flow path and the analysis confirms a highly heterogeneous fiber state. A distinct agglomeration of fibers in the core layers was found using µCT scans. The FD in the core is approximately 40 % higher than the nominal FD. This increased FD in the core may be explained with the shear induced particle migration or with the Fiber-Pull Out mechanism. The implication of this agglomeration for the mechanical performance are expected to be significant, but has not been studied yet. Measurements of the local FD reveal variations along the injection molded part, noticeable in a minimum FD close to the gate and a maximum at the end of the flow path. Results demonstrate a relative decrease in the local FD by approximately -4 % at the beginning of the plaque and relative increase in the local FD of about 3.2 % at the end of the part. FL measurements showed an increase in FL towards the end of the flow path, resulting in a relative increase of 27 % for L_W. All these findings suggest that the area close to the gate would show decreased mechanical properties due to smaller FL and lower FD, while the end of the injection molded plaque would show increased material properties since an increased FL and a higher FD was found.

The experimentally obtained data was used to evaluate a set of models for fiber breakage prediction. Therefore, the measured FL data sets from the Couette rheometer trials were used to validate a continuum model (Phelps model) and a single particle model. Phelps model is based on three fitting parameters, which were verified for their material dependency. The Phelps model was successfully implemented with Matlab and an optimization scheme was developed to fit the model parameters to the experimental data. Individually for each trial, model parameters estimated the residual FLD correctly with less than 30 % error (=experimental error). However, the model parameters cannot be applied in-between the varying processing conditions. Thus, it was not possible to prove the material dependency of these model parameters. Furthermore, the results suggest a dependency on the FC, which is not incorporated in the Phelps model and the FC does only play an indirect role for the input of the Phelps model through the suspension viscosity.

As an additional part of this comprehensive model evaluation, the Phelps model was also applied for the injection molding experiments by comparing three model parameter sets. The default and recommended model parameters from Moldex3D as well as the values reported by Phelps et al., 2013 were used as a reference point and compared to the parameters obtained from the Couette rheometer trials with the same material. Subsequently, the simulation results were compared to the experimentally obtained values. The outcome of this evaluation show a significant discrepancy between the simulation results and measured values for all three sets of model parameters. Especially, the parameters derived from the Couette rheometer experiments lead to inconsistent results. The cause of this is to be found in the fact that these model parameters were obtained by fitting the model to Couette rheometer experiments, where the material experiences smaller rates of deformation and longer processing times compared to an injection molding process, where the material experience larger rates of deformation, but shorter processing times. The different time scales between those two processes ultimately leads to an overestimation of L_N and L_W in the injection molded part.

The experimentally determined FL reduction over time (obtained from the Couette rheometer experiments) was emulated with a single particle model. A representative volume element with periodic BCs was successfully implemented, where fibers are exposed to a simple shear flow and the fiber attrition over time was observed. The comparison showed a good agreement between the experimentally determined and predicted FL values with both results suggest an exponential-decay-type behavior and approach similar L_∞ values. It was shown that the value of L_∞ is higher for the particle level simulation compared to the Couette rheometer trial. Furthermore, the rate of decay for L_N and L_W seems to be higher for the simulation approach than the Couette experiment. In order to obtain a comprehensive validation for the single particle model additional simulations are required to be done as well as further length reduction over time experiments need to be conducted with the Couette rheometer for varying processing conditions. However, single particle level simulations are computationally very expensive, even for small systems and periodic BCs, which limits the range of applications for these type of models.

5 Outlook

The outcome of this work built the basis for additional experimental studies on fiber breakage and fiber matrix separation during processing of LFT materials. Based on the discussed results, the following research aspects and investigations should be carried forward:

- Extend the design of experiment approach for Couette rheometer trials to further study the influence of FC on fiber degradation with focus on a greater variety of FCs, such as 5 %, 10 %, 15 %wt. in the semi-dilute region. Furthermore, the Couette rheometer setup should be tested with PPGF50 and PPGF55 to verify, when the polymer-fiber melt starts acting like a Bingham fluid. Moreover, additional shear rates and melt temperatures should be investigated to validate the found relationships and hypotheses.

- The study of FL reduction over time using the Couette rheometer setup is an important tool to validate and verify models to predict fiber breakage over time. Additional experiments at various processing conditions need to be conducted to be able to support model development and validation.

- Conduct a more detailed study on FD distribution variations in injection molded plaques. Furthermore, the experimentally determined values can be compared to common modeling approaches that assume a uniform FL and FD. Additionally, mechanical testing of coupons of varying microstructures (FL or FD variations near the gate and at end of the part) should be conducted to determine their influence on the final part properties.

- Continue validating the Phelps continuum model for fiber breakage prediction as it is the current benchmark for fiber breakage models in process simulation. The outcome of this work indicate that FC is an important factor of fiber attrition. However, the Phelps model does not incorporate this material property as an input variable, only indirectly though the suspension viscosity. Potentially, the Phelps model can be expanded by an additional term and model parameter that is directly related to the FC. For example, such a term can describe the impact of single fiber buckling at different fiber packing. Furthermore, a methodology that allows

to determine the model parameters for the Phelps model has to be developed and validated.

- Improve the Moldex3D simulation approach. Since it was shown that the model parameters obtained by fitting the model to Couette experiments cannot be used to predict in injection molding simulations a first step should include to account the model parameter c_B in terms of a dimensionless time. The new calculated c_B value should then be used as an input parameter for a Moldex3D simulation to predict fiber breakage in an injection molded plaque. Additionally, it is important to note that the hydrodynamic parameter needs to be evaluated in terms of its dependency on the shear rate and residence time. Furthermore, the Phelps model should be fitted to injection molding experiments to establish a consistent comparison between the experiment, literature and commercial software.

- Run additional single particle model simulations and investigate the breakage behavior on microscale using numerical simulation. Furthermore, the single particle model approach should be validated with a wide range of data sets. Ultimately, these numerical simulations can then replace the experimental studies, such as the Couette rheometer experiments. In a first step, the model´s validity can be tested for the set of data from this work as well as additional experiments.

All these approaches help to gain a higher level of understanding the process induced microstructure as well as to determine and improve the accuracy of existing/latest simulation approaches, so it will eventually be possible to mass produce high performance composites with increased properties and controlled quality making light weight LFTs available to a wider range of applications.

6 References and Bibliography

AKAY, M. & BARKLEY, D. 1991. Fibre orientation and mechanical behaviour in reinforced thermoplastic injection mouldings. *Journal of Materials Science,* 26**,** 2731–2742.

AYOTTE, J. M. & BUND, D. R. 2008. *Method of measuring fiber length for long fiber reinforced thermoplastic composites*. PCT/US2007/078090.

BACK, T. 2016. Microstructure Analysis of Injection Molded Long Fiber-Reinforced Thermoplastics. *Master thesis at the Polymer Engineering Center - University of Wisconsin-Madison*.

BALASUBRAMANIAN, R. 2011. Polymer matrix composites

BAUR, E., GORIS, S., RAMIREZ, D., SCHMIDTKE, P. & OSSWALD, T. A. 2014. Mechanistic model to determine fiber orientation simulation material parameters. *Proceedings of the Annual Technical Conference of the Society of Plastics Engineers, Las Vegas, NV (2014)*.

BRAST, K. 2001. Verarbeitung von langfaserverstärkten Thermoplasten im direkten Plastifizier-/Pressverfahren. *RWTH Dissertation. Aachen*.

CHEN, H., CIESLINSKI, M., WAPPEROM, P. & BAIRD, D. G. 2015. Long Fiber (glass) Breakage in Capillary and Contraction Flow. *SPE ANTEC Paper,* Orlando**,** 546-550.

CLARK, R. 2016. *Understanding Rheology* [Online]. Available: http://www.uow.edu.au/content/groups/public/@web/@sci/@chem/documents/doc/uow107427.pdf [Accessed 17/10/2016.

COX, H. L. 1952. The elasticity and strength of paper and other fibrous materials *British Journal of Applied Physics* 3**,** 72-79.

DEALY, J. M. & WANG, J. 2013. *Melt Rheology and its Application in the Plastics industry*.

DECICCO, M. 2001. An Investigation of Fiber Damage Mechanisms in a Shear Flow Using Glass Fiber Reinforced Polyamide 6. *Master thesis at the Polymer Engineering Center - University of Wisconsin-Madison*.

DOMENICONE-CERQUOZZI, R. 2013. Medición de la Degradación Térmica y por Cizalla de Polímeros usando el Ensayo de MFI.

DURIN, A., MICHELI, P., VIELLE, J., INCEOGLU, F., VALETTE, R. & VERGNES, B. 2013. A matricial approach of fibre breakage in twin-screw extrusion of glass fbres reinforced thermoplastics *Composites,* Part A 48 47-56.

ELBARCHE, N., CANDAL, M. V., YANEV, A. & OSSWALD, T. A. 2010. Experimental Study of Fiber Attrition Within a Long Fiber Glass-Reinforced PP under Controlled Conditions. *Journal of Composite Materials,* not published yet.

FILBERT, W. 1969. *SPE Journal,* 25.

FOLGAR, F. & TUCKER, C. L. 1984. Orientation Behavior of Fibers in Concentrated Suspensions. *Journal of Reinforced Plastics and Composites,* 3**,** 98-119.

FREEDONIA 2013. Fiber-Reinforced Plastic Composites. *US Industry Study with Forecasts for 2017 & 2022,* Study #3092**,** 317 pages.

GARESCI, F. & FLIEGENER, S. 2013. Young´s modulus prediction of long fiber reinforced thermoplastics *Composites Science and Technology,* 85**,** 142-147.

GORIS, S. 2016. Characterization of the process-induced fiber configuration of long glass fiber-reinforced thermoplastics. *Preliminary PhD Report at the Polymer Engineering Center, University of Wisconsin-Madison*.

GORIS, S., GANDHI, U., SONG, Y. Y. & OSSWALD, T. A. 2016. Analysis of the process-induced microstructure in injection molding of long glass fiber-reinforced thermoplastics *SPE ANTEC™ Indianapolis 2016***,** 318-326.

GORIS, S. & OSSWALD, T. A. 2016. Progress on the characterization of the process-induced fiber microstructure of long glass fiber-reinforced thermoplastics. *Proceedings of the 16th SPE Automotive Composites Conference & Exhibition (ACCE), Novi, MI (2016)*.

GUPTA, V., MITTAL, R., SHARMA, P., MENNING, G. & WOLTERS, J. 1989. Some studies on glass fiber-reinforced polypropylene.Part 1: reduction in fiber length during processing. *Polymer Composites* 10**,** 8-15.

HA, P. T. T. 2015. The introduction of composites material

HAMEDI, N. 2015. Data Correction in Couette Rheomete. *Lund University*.

HASSAN, A., YAHYA, R., YAHAYA, A. H., TAHIR, A. R. M. & HORNSBY, P. R. 2004. Tensile, impact and fiber length properties of injection-molded short and long glass fiber-reinforced polyamide 6,6 composites. *Reinforced Plastic Composites,* 23**,** 969-986.

HÖHN, D.-I. T. N. 2016. *FASEP* [Online]. xyz high precision: Dipl.-Ing. (TH) Norbert Höhn Available: http://www.fasep.biz/index.html [Accessed 7/31 2016].

INCEOGLU, F., VILLE, J., GHAMRI, N., PRADEL, J. L., DURIN, A., VALETTE, R. & VERGNES, B. 2011. Correlation between processing conditions and fiber breakage during compounding of glass fiber-reinforced polyamide. *Polymer Composites*.

INOUE, A., MORITA, K., TANAKA, T., ARAO, Y. & SAWADA, Y. 2015. Effect of screw design on fiber-breakage and dispersion in injection-molded long glass-fiber-reinforced polypropylene. *Journal of Composite Materials,* Vol. 49(I) 75-84.

JEYANTHI, S. & RANI, J. J. 2012. Influence of natural long fiber in mechanical, thermal and recycling properties of thermoplastic composites in automotive components. *International Journal of Physical Sciences,* 7**,** 5765-5771.

KELLY, A. 1966. Strong solids-fibre reinforcement. *Oxford University Press*.

KELLY, A. & TYSON, W. R. 1965. Tensile properties of fibre-reinforced metals: copper/tungsten and copper/molybdenum. *Journal of Mechanics and Physics of Solids,* 13**,** 329-350.

KUNC, V., FRAME, B., NGUYEN, B., III, C. T. & VELEZ-GARCIA, G. 2007a. Fiber length distribution measurement for long glass and carbon fiber reinforced injection molded thermoplastics *Proceedings of the 7th annual society of plastic engineers automotive composites conference and exposition,* MI: Troy.

KUNC, V., FRAME, B., NGUYEN, B. N., III, C. L. T. & VELEZ-GARCIA, G. 2007b. Fiber length distribution measurements for long glass and carbon fiber reinforced injection molded thermoplastics.

LAFRANCHE, E. 2007. Injection moulding of long glass fibre reinforced polyamide 6-6. Guidelines to improve flexural properties. *eXPRESS Polymer Letters 1,* 7**,** 456–466.

LAFRANCHE, E., KRAWCZAK, P., CIOLCZYK, J.-P. & MAUGEY, J. 2005. Injection moulding of long glass fiber reinforced polyamide 66. Processing conditions/microstructure/flexural properties relationship. *Advances in Polymer Technology,* 24**,** 114-131.

LAI, M., KREMPL, E. & RUBEN, D. 2010. *Introduction to Continuum Mechanics*, Elsevier Inc.

LARBIG, H., SCHERZER, H., DAHLKE, B. & POLTROCK, R. 1998. Natural fibre reinforced foams based on renewable resources for automotive interior applications. *ournal of Cellular Plastics,* 34**,** 361-379.

LATIMER, T., SUDRLA, J., HENSHAW, J., DAHL, J. & BLANCHARD, P. 2008. A method for characterizing fiber length distribution in random fiber composites.

LEE, S. M. 1992. *Handbook of Composite Reinforcements*, Wiley-VCH.

LINDSTRÖM, S. B. & UESAKA, T. 2007. Simulation of the motion of flexible fibers in viscous fluid flow *Physics of Fluids,* 19.

LOPEZ, L., RAMIREZ, D. & OSSWALD, T. A. 2013. Fiber attrition and orientation productions of a fiber filled polymer through a gate - a mechanistic approach. *ANTEC 2013*.

MALLICK, P. K. 2007. *Fiber-Reinforced Composites: Materials, Manufacturing, and Design*, CRC Press - Taylor & Francis Group.

MALNATI, P. 2007. *Reinforced Thermoplastics: LFRT/GMT Roundup* [Online]. Composites World. Available: http://www.compositesworld.com/articles/reinforced-thermoplastics-lfrtgmt-roundup [Accessed 25/10 2016].

MANIAS, E. 2016. *Rheology - Rotational and sliding surface Rheometers (Couette Devices) Gap Loading vs. Surface Loading* [Online]. Materials Science & Eng. Department - Pennsylvania State University. Available: http://zeus.plmsc.psu.edu/~manias/MatSE447/13_Rheometry.pdf 17/10/2016].

MICROPHOTONICSINC. 2015. *How does a micro-CT scanner work?* [Online]. Micro Photonics Inc. . Available: https://www.microphotonics.com/how-does-a-microct-scanner-work/ [Accessed 20/10 2016].

MORITZER, E. & HEIDERICH, G. 2016. Fiber length degradation of glass fiber reinforced polypropylene during shearing. *SPE ANTEC Paper,* Indianapolis**,** 647-651.

MÖRL, D.-I. S. 2016. *Fibre Length Analysis FASEP* [Online]. University of Bayreuth: Dipl.-Ing. Stefan Mörl. Available: http://polymer-engineering.de/en/equipment/additional-appliancies/fibre-length-analysis-fasep.html [Accessed 7/31 2016].

MORRIS, J. F. & BOULAY, F. 1999. Curvilinear flows of noncolloidal suspensions: The role of normal stresses. *Journal of Rheology,* 43.

MOSHE, A. V., SIEGMANN, N., SIEGMANNS, A. & KENIG, S. 2012. Short-fiber thermoplastics composites fiber fracture during melt processing. *Wiley Encyclopedia of Composites,* 2.

NGUYEN, B. N. 2010. An Elastic-plastic Damage Model for Long-fiber Thermoplastics. *International Journal of damage mechanics,* 19**,** 691-725.

NGUYEN, B. N., BAPANAPALLI, S. K., HOLBERY, J. D., SMITH, M. T., KUNC, V., FRAME, B. J., PHELPS, J. H. & III, C. L. T. 2008a. Fiber Length and Orientation in Long-Fiber Injection-Molded Thermoplastics – Part I: Modeling of Microstructure and Elastic Properties. *Journal of Composite Materials,* 42**,** 1003-1029.

NGUYEN, B. N., BAPANAPALLI, S. K., HOLBERY, J. D., SMITH, M. T., KUNC, V., FRAME, B. J., PHELPS, J. H. & TUCKER, C. L. 2008b. Fiber length and orientation in long-fiber injection-molded thermoplastics -- Part 1: Modeling of microstructure and elastic properties. *Journal of Composite Materials,* 42**,** 10: 1003.

NGUYEN, N., HOLBERY, J. D., JOHNSON, K. I. & SMITH, M. T. 2015a. *Long-Fiber Thermoplastic Injection Molded Composites: From Process Modeling to*

Property   Pediction   [Online].   ResearchGate.   Available:
https://www.researchgate.net/publication/241970147_Long-
Fiber_Thermoplastic_Injection_Molded_Composites_from_Process_Modelin
g_to_Property_Prediction [Accessed 20/10 2016].

NGUYEN, T. B. T., MORIOKA, M., YOKOYAMA, A., HAMANAKA, S., YAMASHITA, K.
& NONOMURA, C. 2015b. Measurement of fiber orientation distribution in
injection-molded short-glass-fiber composites using X-ray computed
tomography. *Journal of Materials Processing Technology,* 219**,** 1-9.

OSSWALD, T. A. 2011. *Understanding polymer processing - Processes and
governing equations,* Munich, Carl Hanser Verlag.

OSSWALD, T. A., BAUR, E., BRINKMANN, S., OBERBACH, K. & SCHMACHTENBERG,
E. 2006. *International Plastics Handbook*, Carl Hanser Verlag GmbH & Co.
KG

OSSWALD, T. A. & MENGES, G. 2012. *Material Science of Polymers for Engineers*,
Carl Hanser Verlag.

OSSWALD, T. A. & RUDOLPH, N. 2015. *Polymer Rheology - Fundamentals and
Applications,* Munich, Carl Hanser Verlag.

PATCHARAPHUN, S. & OPASKORNKUL, G. 2008. Characterization of fiber length
distribution in short and long-glass fiber reinforced polypropylene during
injection molding process. *Kasetsart Journal***,** 392-397.

PEREZ, C., GORIS, S. & OSSWALD, T. A. 2013. Study on the fiber properties of a
LFT strand. *Proceedings of the 13th SPE Automotive Composites Conference
& Exhibition (ACCE), Novi, MI (2013)*.

PEREZ, C., TAPIA, A. & OSSWALD, T. A. 2016a. Particel level simulation of fiber
motion to determine continuum based models parameters for fiber
orientation prediction. *ECCM17* 17th European Conference on Composite
Materials.

PEREZ, J. C., RAMIREZ, D. & OSSWALD, T. A. 2016b. Particle Level Simulation for
Fiber Orientation Prediction in SMC. *Composites,* not published yet.

PHELPS, J. H. 2009. Processing-microstructure models for short- and long- fiber
thermoplastic composites. *Dissertation - Mechanical Engineering at the
Graduate College of the University of Illinois at Urbana-Champaign*.

PHELPS, J. H., EL-RAHMAN, A. I. A., KUNC, V. & III, C. L. T. 2013. A model for
fiber length attrition in injection-molded long-fiber composites. *Composites,*
Part A**,** 11-21.

RAMANI, K., BANK, D. & KRAEMER, N. 1995. Effect of screw design on fiber
damage in extrusion compounding and composite properties. *Polymer
Composites,* 16**,** 285-266.

REN, P. & DAI, G. 2014. Fiber dispersion and breakage in deep screw channel
during processing of long-fiber reinforced polypropylene. *Fibers and
Polymers,* 15**,** 1507-1506.

RHODE, M., EBEL, A., WOLFF-FABRIS, F. & ALTSTÄDT, V. 2011. Influence of
processing parameters on the fiber length and impact properties of injection
molded long glass fiber reinforced polypropylene. *International Polymer
Processing,* 16.

ROHDE, M., EBEL, A., WOLFF-FABRIS, F. & ALTSTÄDT, V. 2011. Influence of
processing parameters on the fiber length and impact properties of injection
molded long glass fiber reinforced polypropylene. *International Polymer
Processing,* 26.

SABIC. 2016. *Processing guides: SABIC® STAMAX* [Online]. Available:
https://www.sabic.com/europe/en/products-

services/plastics/technical/Processing-guides--SABIC-STAMAX [Accessed 10/12/2016.

SCHATT, W. 1983. Einführung in die Werkstoffwissenschaft. *VEB Deutscher Verlag für Grundstoffindustrie,* 5. Auflage.

SCHMID, C. F., SWITZER, L. H. & KLINGENBERG, D. J. 2000. Simulations of fiber flocculation: Effects of fiber properties and interfiber friction *Journal of Rheology* 44.

SERVAIS, C., LUCIANI, A. & MANSON, J.-A. E. 1999. Fiber-fiber interaction in concentrated suspensions: Dispersed fiber bundles *The Society of Rheology* 43(3).

SHI, D., XIAO, X., LEE, W. & JASIUK, I. M. 2013. Fiber orientation measurement of injection molded long-glass-fiber reinforced thermoplastics.

SHIMIZU, Y., ARAI, S., ITOYAMA, T. & KAWAMOTO, H. 1997. Experimental analysis of the kneading compounding. *Advances in Polymer Technology,* 16**,** 25-32.

SHON, K., LIU, D. & WHITE, J. L. 2005. Experimental studies and modeling of development of dispersion and fiber damage in continuous compounding. *International Polymer Processing,* 20**,** 322-331.

SHON, K. & WHITE, J. 1999. A comparative study of fiber breakage in compounding glass fiber-reinforced thermoplastics in a buss kneader, modulus co-rotating and counter-rotating twin screw extruders. *Polymer Engineering and Science,* 39**,** 1757-1768.

SIEMENS. 2016. *CAE / Computer-Aided Engineering* [Online]. Available: https://www.plm.automation.siemens.com/en_us/plm/cae.shtml [Accessed 27/9 2016].

SIMON, S. A. 2016. Fiber breakage in processing of discontinous fiber-reinforced thermoplastics. *Literature Research Project at the University of Applied Sciences Wiener Neustadt, Campus Tulln*.

STADE, K. 1977. Techniques for Compounding Glass Fiber-Reinforced Thermoplastics. *Polymer Engineering and Science,* 17**,** 50-56.

STELZER, G. 2003. Zum Faser- und Eigenschaftsabbau bei Verarbeitung und Recycling diskontinuierlich faserverstärkter Kunststoffe. *Dissertation*

STEWART, R. 2003. Composites on the road to the big time. *Reinforced Plast***,** 33-47.

STRAUTINS, U. 2008. Flow-driven orientation dynamics in two classes of fibre suspensions. *Dissertation - Fachbereich Mathematik der Technischen Universit¨at Kaiserslautern*.

STRONG, A. B. 2000. *Plastics materials and processing,* New Jersey: Prentice Hall.

TAN, Y., WANG, X. & WU, D. 2015. Preparation, microstructures, and properties of long-glass-fiber-reinforced thermoplastic composites based on polycarbonate/polybutylene terephthalate alloys. *Journal of Reinforced Plastics and Composites,* 34**,** 1804–1820.

THOMASON, J. L. 2002. The influence of fiber length and concentration on the properties of glass fibre reinforced polypropylene: 5 Injection moulded long and short fibre PP. *Polymer Composites,* A**,** 1641-1652.

THOMASON, J. L. 2005. The influence of fibre length and concentration on the properties of glass fibre reinforced polypropylene. 6. The properties of injection moulded long fibre PP at high fibre content. *Composites,* Part A 995–1003.

THOMASON, J. L. 2006. Structure-property relationships in glass reinforced polyamide: 1) The effects of fibre content. *Polymer Composites,* 27**,** 552-562.

TOLL, S. & ANDERSSON, P. O. 1993. Microstructure of long- and short-fiber reinforced injection molded polyamide. *Polymer Composites,* 14.

TURKOVICH, R. & ERWIN, L. 1983a. Fiber fracture in reinforced thermoplastic processing. *Polymer Engineering and Science,* 23**,** 723-749.

TURKOVICH, R. V. & ERWIN, L. 1983b. Fiber fracture in reinforced thermoplastic processing *Polymer Engineering and Science* 23**,** 743-9.

VELEZ-GARCIA, G. M. 2012. Experimental Evaluation and Simulation of Fiber Orientation in Injection Molding of Polymers Containing Short Glass Fibers. *Virginia Polytechnic Institute and State University Dissertation. Blacksburg, VA*.

WALL, D. 1989. The Processingof Fiber-Reinforced Themeroplastics Using Co-Rotating Twin Screw Extruder. *Polymer Composites,* 10.

WAMBUA, P., IVENS, J. & VERPOEST, I. 2003. Natural fibers: can they replace glass in fiber reinforced plastics? *Composites Science and Technology,* 63**,** 1259-1264.

WANG, J., GENG, C., LUO, F., LIU, Y., WANG, K., FU, Q. & HE, B. 2011. Shear induced fiber orientation, fiber breakage and matrix molecular orientation in long glass fiber reinforced polypropylene composites. *Materials Science and Engineering* A**,** 3169-3176.

YILMAZER, U. & CANSEVER, M. 2002. Effects of processing conditions on the fiber length distribution and mechanical properties of glass fibre reinforced nylon-6. *Polymer Composites,* 23, No. 1.

ZENG, D., LU, L., ZHOU, J., LI, Y., XIA, Z., HOKE, P., DANIELSON, K. & SOUZA, D. 2015. Modeling of Long Fiber Reinforced Plastics. *SAE Technical Paper,* 2015-01-0698.

ZHANG, G. & THOMPSON, M. R. 2005. Reduced fibre breakage in a glass-fibre reinforced thermoplastic though foaming. *Composites Science and Technology,* 65**,** 2240-2249.

ZHUANG, H., REN, P., ZONG, Y. & DAI, G. C. 2008. Relationship between fiber degradation and residence time distribution in the procesing of long fiber reinforced thermoplastics. *eXPRESS Polymer Letterd,* 2**,** 560-568.

Appendix

All experimentally results obtained from the Couette rheometer experiments were successfully used to fit the three model parameters. The optimum set of fitting parameters for each material and each processing condition is shown Table 1.

Table 1: Optimum found set of model parameters for PPGF20, PPGF30 and PPGF40 for varying process conditions.

Material	Processing conditions			Model parameters		
Fiber content [%wt]	Temperature [°C]	Processing speed [Rpm]	Residence Time [s]	Breakage coefficient C_B	Drag coefficient ζ	Shape factor S
20	280	46	120	0.000762	0.039658	1.998087
	280	46	300	0.000422	4.441290	1.993216
	280	160	120	0.000422	4.441290	1.993216
	280	160	300	0.000157	2.904304	0.974042
30	220	46	120	0.001500	0.312681	1.744757
	220	46	300	0.001500	0.079021	1.983968
	220	160	30	0.001686	0.347086	1.939320
	220	160	45	0.001621	0.626135	0.620720
	220	160	60	0.001500	2.500300	1.761514
	220	160	90	0.001500	0.365318	1.999333
	220	160	120	0.042429	0.264851	1.669495
	220	160	300	0.003115	0.070248	1.999913
	220	160	600	0.001602	0.122808	1.998116
	280	46	120	0.001500	0.007771	1.985098
	280	46	300	0.013167	0.015628	1.999478
	280	160	120	0.013167	0.015628	1.999478
	280	160	300	0.001561	0.042023	1.998753
	280	160	600	0.001602	0.122808	1.998116
40	280	46	120	0.001500	1.681535	1.999362
	280	46	300	0.001096	4.999924	1.999420
	280	160	120	0.000803	2.229108	1.495863
	280	160	300	0.000400	1.911610	1.993129